Università degli Studi di Genova
Facoltà di Scienze Matematiche Fisiche e Naturali
Dottorato di Ricerca in Fisica, XIII Ciclo
Anno Accademico 1999-2000

Tesi di Dottorato

MEASUREMENT OF THE DOUBLE SPIN ASYMMETRY IN π^+ ELECTROPRODUCTION WITH CLAS

candidato:
Raffaella De Vita

Relatore:
Chiar.^{mo} Prof. G. Ricco
Università di Genova

Relatore esterno:
R. Minehart
Professor of Physics
University of Virginia

Contents

Figures

Tables

Introduction

Single-pion electroproduction is a powerful tool to investigate the structure of the nucleon and of its excited states. Most of the known baryonic resonances have in fact large branching ratios in the πN channel and the study of the different decay modes ($\pi^+ n$, $\pi^0 p$, $\pi^- p$, $\pi^0 n$) allows the isospin decomposition of the process. Furthermore the measure of the Q^2 dependence of the electro-excitation mechanism allows to probe the spatial structure of the nucleon and of the resonance wave functions. However the simple cross-section measurement is not sufficient to obtain the full spin decomposition of the process. The cross section is in fact determined by a linear combination of the hadronic response functions. These quantities depends both on the helicity of the virtual photon and of the nucleon, so that their determination can be achieved only by exploiting the spin degrees of freedom and by measuring the corresponding observables. These quantities provide a physics information that has been demonstrated to be extremely sensitive to the details of the hadronic structure and consequently are a unique mean to approach the study of baryonic resonances.
For these reasons, a significant part of the experimental program in Hall B at Jefferson Lab is dedicated to the measurement of spin observables both in inclusive and exclusive reactions. An experiment with polarized electrons impinging on a polarized proton and deuteron target is in progress in Hall B using CLAS (CEBAF Large Acceptance Spectrometer). The CEBAF accelerator provides highly polarized electron beam using the GaAs-cathode technique while the CLAS polarized target consists of solid NH_3 and ND_3 material polarized via Dynamic Nuclear Polarization. This experiment provides data in the nucleon-resonance region at moderate and low Q^2 (0.2 GeV^2/c^2 $< Q^2 <$1.75 GeV^2/c^2) and for the first time allows the extraction of single and double spin asymmetries in single-pion electroproduction. A first experimental run was completed in December '98 providing a significant amount of data, while a second run to extend the available data is presently in progress.
The present thesis describes the measurement of the double spin asymmetry in the $ep \to e\pi^+ n$ reaction. This represents the only existing measurement for this observable. The reaction is identified detecting the scattered electron and the emitted pion and using the missing mass technique to identify the neutron. The asymmetry is evaluated as a function of the four-momentum transfer Q^2, the invariant mass W and the

pion center of mass angle θ^*. These are in fact the variables that determine the transition amplitudes for the process. The W range of this measurement varies from the pion threshold to a maximum value of 1.8 GeV, exploring the full resonance region. The results obtained with this analysis in the evaluation of the spin asymmetry are presented. The outline of the thesis can be summarized as follows. In the first chapter I will describe the physics motivation that are at the basis of this experiment. In the second and third chapters I will illustrate the design of the CLAS detector and of the polarized target. The fourth chapter is dedicated at the description of the event reconstruction and to the event selection while the analysis procedure is described in chapter five. In chapter sixth I will finally discussed the results of this measurement, including the evaluation of the systematic uncertainty and the comparison with a physics model.

Chapter 1

Single Pion Electroproduction

1.1 Introduction

The main motivation of the research in strong interaction physics is the understanding of the hadrons structure and of the basic principle of their interaction mechanism. A consistent theoretical picture of strong interactions is provided by Quantum Chromo Dynamics (QCD) that describes this physics in term of quark and gluons, i.e. elementary objects. In the high energy regime perturbative methods can be applied and the QCD predictions have given remarkable results in the understanding of the basic mechanisms. However at lower energy, where the perturbative approach fails, the present knowledge is not sufficient to understand the strong force and how for example it manifests in the structure of complex hadronic system as baryons. In this regime lattice QCD is now providing useful information about the static properties of hadrons, but for light quark baryons as the nucleon crude approximation are still necessary.
An alternative approach is given by chiral theories that apply QCD at very low energy. In their validity range, close to pion threshold, it is possible to perform accurate calculation. However correction due to resonance contributions cannot be calculated model independently.
In this scenario, models of the hadron structure have still an important role to provide theoretical support, and, as a consequence, it is fundamental to perform the experiments that may provide the necessary information to test and improve these models.
One of the most efficient tools to probe the hadronic structure is the electron scattering. The main advantage is given by the possibility of separating the leptonic vertex, completely predicted in QED, from the hadronic vertex that contains the new information. In addition it provides a mean to study the nucleon wave function as well as the excitation spectrum and the wave functions of the excited states with final information that can be complementary to pion scattering. Finally electroproduction allows the study of the spatial and spin structure of the resonance transition by varying the four momentum transfer.
Large and successful efforts have been dedicated to obtain accurate measurements of the inclusive electro-production cross section in a large Q^2 and W range (see ref. [1]). Nevertheless inclusive measurements do not allow the separation of the different excited states (see figure 1.1). It has in fact been proven that the inclusive cross section below an invariant mass of 2 GeV is actually determined by the overlap of several excited states

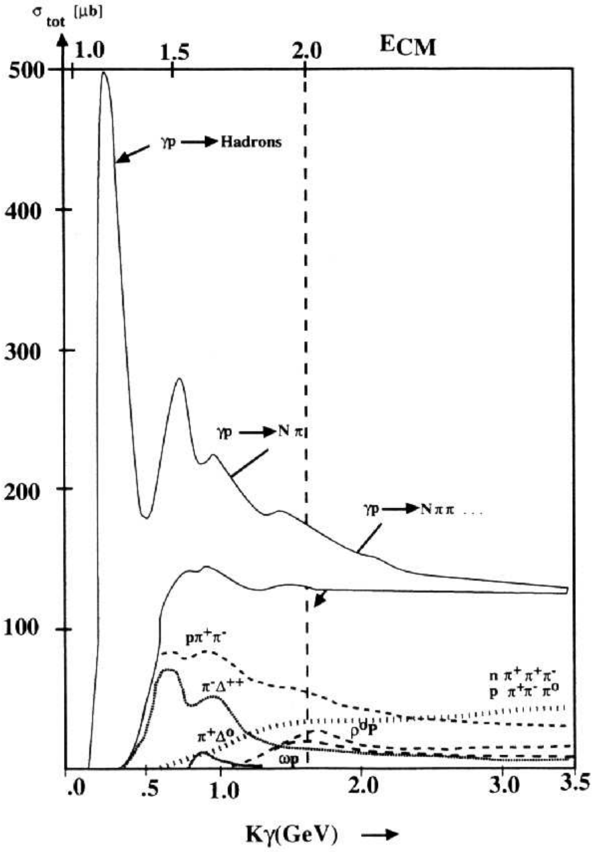

Figure 1.1: *Photoabsorption and total photoproduction cross section for various exclusive channels.*

superimposed on a smooth background. An unambiguous separation of these contributions can be achieved only by measuring exclusive reaction as $\gamma N \to \pi N$, $\gamma N \to \eta N$, $\gamma N \to \rho N$ or $\gamma N \to \Delta N$.
The πN final states is in general preferable since most of the baryonic resonances have significant branching ration in this channel. The pion threshold lies in fact below the first resonance region and the $\Delta(1232)$ decays only in this final states. Furthermore the measures of the different isospin channels, π^+, π^0 and π^-, allows the separation of the cross-section into its isospin components, while the measure of the pion angular distribution leads to the spin decomposition. Experiments in single pion electroproduction were for the first time performed in the seventies in several different facilities. These studies were mainly devoted to the measurements of the cross-section and the angular distribution. In spite of the large number of information that were provided, they had to face the intrinsic problem of extracting a large number of amplitudes and electromagnetic multipoles from a limited number of observables with the obvious result of very complicated and sometime ambiguous analysis. At that time no attempt of measuring polarization observables was done because of technical limitations.
In the following years, the first double polarization measurements in inclusive electron scattering were performed at SLAC with the extraction of the polarized structure functions [2, 3]. From that time several other measurement of polarization observables have

been performed both in inclusive and semi-inclusive or exclusive scattering. At present, measurements of single pion photo and electroproduction with polarized beam and targets are in progress leading to significant improvements in respects to the original experiments. They give finally access to several unmeasured observables related to the spin degrees of freedom of the process. These quantities introduce additional constraints on the physics analysis that aims at the extraction of the resonance parameters and give a sensitive tools to understand the details of the strong interaction mechanisms.
This chapter is dedicated to an overview of single pion electroproduction as a tool to study the baryonic resonances. In the first sections, the typical formalism will be introduced including the definition of the spin observables relative to this process. In section 1.3 a review of selected topics in pion production will be presented. Finally the CLAS program in the study of the spin structure of baryonic resonances will be described, including the present experiment.

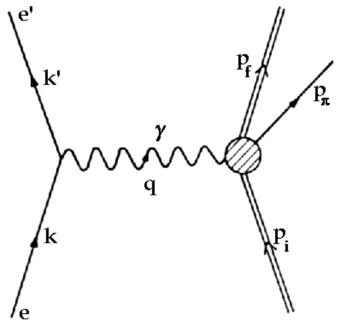

Figure 1.2: *Diagram for the exclusive electroproduction of one pion in the OPE (one photon exchange) approximation.*

1.2 Formalism

Since the electromagnetic interaction is governed by the fine structure constant $\alpha = e^2/4\pi$, the interaction between electron and nucleon can be described with the exchange of a photon with well defined energy $\omega = \epsilon_i - \epsilon_f$ and three-momentum $\mathbf{q} = \mathbf{k_i} - \mathbf{k_f}$, being ϵ and k the energy and three momentum of the initial and final electrons (see figure 1.2). The independent variation of $\mathbf{q}$ and ω allows to explore the spatial distribution of the phenomenon under investigation.
In the following I will use as independent variables two invariants: the momentum transfer $Q^2 = -q^2 = \mathbf{q}^2 - \omega^2$ and $W = (m_N^2 + 2m_N\omega - Q^2)^{1/2}$ that represent the mass of the excited hadronic system. Obviously Q^2 vanishes for real photons. The kinematics of the hadronic system is described in terms of the four momenta of the initial nucleon $p_i = (E_i, \mathbf{p_i})$, of the recoiling nucleon $p_f = (E_f, \mathbf{p_f})$ and of the emitted pion $p_\pi = (E_\pi, \mathbf{p}_\pi)$. Because of energy and momentum conservation, in addition to the virtual photon variables there are only two independent variables describing the hadronic system. These are usually chosen to be the angles θ^* and ϕ^* of the emitted pion in the center of mass system (see figure 1.3).
Using the notation in ref. [4], the differential cross section for the electroproduction

process can be written as

$$
\begin{aligned}
d\sigma &= \frac{\epsilon_i}{k_i}\frac{m_e}{\epsilon_i}\frac{m_N}{E_i}\frac{m_e}{\epsilon_f}\frac{d^3\mathbf{k_f}}{(2\pi)^3}\frac{1}{2E_\pi}\frac{d^3\mathbf{p}_\pi}{(2\pi)^3}\frac{d^3\mathbf{p_f}}{(2\pi)^3} \\
&\cdot \quad (2\pi)^4\delta^{(4)}(p_i+q-p_\pi-p_f) \\
&\cdot \quad |<p_f,p_\pi|J^\mu|p_i>q^{-2}<k_f|j_\mu|k_i>|^2,
\end{aligned}
\tag{1.1}
$$

where the phase space is evaluated in the laboratory frame and j^μ and J^μ represent the electromagnetic current of the electron and hadronic system respectively. The square of the transition matrix elements of the currents in the previous equation can be cast into the product of two rank-2 Lorentz tensors $\eta_{\mu\nu}$ and $W_{\mu\nu}$, respectively the leptonic and hadronic tensors. The leptonic tensor is well known and can be written as

$$
\begin{aligned}
\eta_{\mu\nu} &= \sum_{s_f}(\bar{u}(k_f,s_f)e\gamma_\mu u(k_i,s_i))(\bar{u}(k_f,s_f)e\gamma_\nu u(k_i,s_i))^* = \qquad (1.2) \\
&= \frac{e^2}{4m_e^2}\Big((k_{f_\mu}+k_{i\mu})(k_{f_\nu}+k_{i\nu})+q^2g_{\mu\nu}+2ih\epsilon_{\mu\nu\alpha\beta}q^\alpha(k_f^\beta+k_i^\beta)\Big)
\end{aligned}
$$

where h represents the helicity of the electron, $g_{\mu\nu}$ is the (symmetric) metric tensor and $\epsilon_{\mu\nu\alpha\beta}$ is a completely antisymmetrical tensor. The previous formula is valid in the assumption of undetected spin state of the final electron.
Gauge invariance is fulfilled since

$$q^\mu\eta_{\mu\nu} = \eta_{\nu\mu}q^\mu = 0.$$

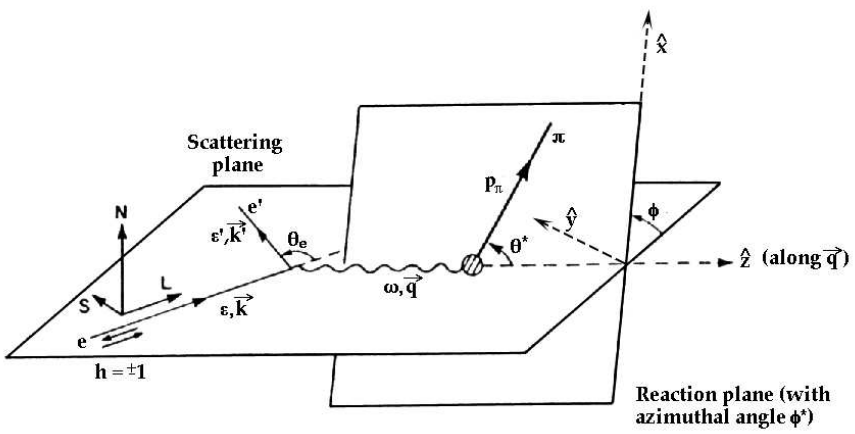

Figure 1.3: *Kinematics for single pion electroproduction. The leptonic plane id defined by the direction of the incident and scattered electrons, while the hadronic plane is defined by the direction of the virtual photon and of the emitted pion. The reaction is usually described in term of the virtual-photon variables (Q^2 and W) and of the angles of the emitted pion in the center of mass system. These are the angle ϕ^* between the leptonic and hadronic plane and the angle θ^* between the virtual photon and pion direction. The spin of the electron is assumed to be longitudinal and is represented by the helicity h while the spin of the target is usually decomposed in the frame identified by the vectors $\hat{x}$, $\hat{y}$, $\hat{z}$.*

The hadronic tensor $W^{\mu\nu} =< p_f, p_\pi | J^\mu | p_i >< p_f, p_\pi | J^\nu | p_i >^*$ depends instead on the structure of the particles involved in the process as well as on the excitation mechanism and therefore can only be parameterized. A typical choice for this parameterization is given by the helicity basis in which the transition amplitudes between states with well-defined helicity are considered. Since the process involves the absorption of a spin 1 object, the virtual photon, from a spin 1/2 nucleon to produce a spin 1/2 and a spin zero particle in the final state, there are 12 different complex amplitudes. Due to parity symmetry only six of them are independent so that, in the end, the hadronic tensor can be written in terms of 12 unknown real functions.
Using the typical notation [5]

$$H = \langle \lambda_\pi, \lambda_f | T | \lambda_\gamma, \lambda_i \rangle,$$

where λ_i and λ_f represents the helicity of the nucleon in the initial and final states, λ_γ is the virtual photon helicity and λ_π is the pion helicity obviously equal to zero, the six complex quantities are reported below:

$$\begin{aligned} H_1 &= \langle 0, +1/2 | T | +1, +1/2 \rangle \\ H_2 &= \langle 0, +1/2 | T | +1, -1/2 \rangle \\ H_3 &= \langle 0, -1/2 | T | +1, +1/2 \rangle \\ H_4 &= \langle 0, -1/2 | T | +1, -1/2 \rangle \\ H_5 &= \langle 0, +1/2 | T | 0, +1/2 \rangle \\ H_6 &= \langle 0, -1/2 | T | 0, -1/2 \rangle . \end{aligned} \tag{1.3}$$

The first four amplitudes are relative to the absorption of transverse virtual photons and determines the photoproduction cross section, while H_5 and H_6 describe the contribution of longitudinal photon and therefore appears only in electron scattering. An intuitive picture of this matrix elements is shown in figure 1.4. H_1 and H_3 contributes to the helicity 1/2 amplitude, while H_2 and H_4 determines the 3/2 amplitude.

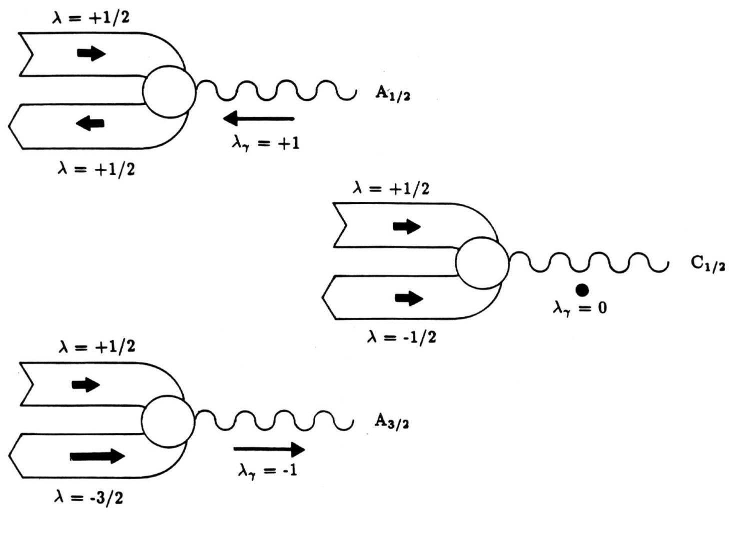

Figure 1.4: *Decomposition of the hadronic vertex in term of helicity amplitudes.*

Using this basis, it's possible to express the hadronic current $\mathbf{J}$ in terms of its spherical components $J_{\pm,0}$, with $J_{\mp} = \mp(J_x \pm J_y))/\sqrt{2}$ and $J_0 = J_z$. Since the components of the current operator are defined in two-dimensional Pauli spin space, they can be written as 2×2 matrices in terms of the helicity amplitudes H_i

$$J_+ = \begin{pmatrix} H_1 & H_2 \\ H_3 & H_4 \end{pmatrix} \quad J_- = \begin{pmatrix} H_4 & -H_3 \\ -H_2 & H_1 \end{pmatrix} \quad J_0 = \begin{pmatrix} H_5 & H_6 \\ H_6 & -H_5 \end{pmatrix}$$

Based on this parameterization, the transition matrix elements of the currents in eq. 1.1 can be substituted [6]. Assuming to deal with the unpolarized case in which the electron and proton in the initial state are unpolarized and the recoil polarization of the nucleon in the final state is undetected, the final expression of the cross section can be written as

$$\frac{d\sigma}{dE' d\Omega_e d\Omega^*_\pi} = \Gamma_\gamma \frac{d\sigma_v}{\Omega^*_\pi}, \tag{1.4}$$

where Γ_γ is the virtual photon flux given by

$$\Gamma_\gamma = \frac{\alpha}{2\pi^2} \frac{E'}{E_0} \frac{q_\gamma^{lab}}{Q^2} \frac{1}{1-\epsilon} \tag{1.5}$$

and the virtual photon cross-section is

$$\frac{d\sigma_v}{d\Omega^*_\pi} = \frac{|\mathbf{q}|}{q_\gamma^{CM}} \{R_T^0 + \epsilon_L R_L^0 + \sqrt{2\epsilon_L(1+\epsilon)} R_{LT}^0 \cos\phi^* + \epsilon R_{TT}^0 \cos 2\phi^*\} \tag{1.6}$$

where the functions $R_i = R_i(Q^2, W)$, called response functions, are bilinear combination of the helicity amplitudes H_i (see Appendix A). In this expression I have used the quantity ϵ which represents the degree of transverse polarization of the virtual photon and is defined as

$$\epsilon = (1 + \frac{2\mathbf{q}^2}{Q^2} \tan^2 \frac{\Theta_e}{2})^{-1}.$$

This parameter is invariant under collinear transformation while the longitudinal polarization

$$\epsilon_L = \frac{Q^2}{\omega}\epsilon$$

is frame dependent. The quantity $q_\gamma^{lab} = (W^2 - M^2)/2M$ denotes the "photon equivalent energy", i.e. the laboratory energy necessary for a real photon to excite a hadronic system with C.M. energy W.

By measuring the cross section for the electroproduction process and in particular it's angular dependence, it's possible to separate the 4 response functions that determines the unpolarized cross section and extract from them information on the helicity amplitudes. It's clear anyhow that the measurement of 4 real observables is not sufficient to extract the six independent helicity amplitudes, unless further assumptions on the mechanism governing the process are made. For this reason, it has been often pointed out the need for a 'complete' experiment, an experiment that by using polarization degrees of freedom would measure simultaneously enough observables to extract in a model independent way

the 6 helicity amplitudes.
Limiting the discussion to case of beam and target polarization, the case of interest for this thesis, 14 additional terms need to be included in the cross section reported in eq. 1.6 that becomes [6, 7, 8]:

$$\begin{aligned} \frac{d\sigma_v}{d\Omega^*_\pi} &= \frac{|\mathbf{q}|}{q_\gamma^{CM}}\{R_T^0 + P_y R_T^y + \epsilon_L(R_L^0 + P_y R_L^y) + \\ &+ \sqrt{2\epsilon_L(1+\epsilon)}[(R_{LT}^0 + P_y R_{LT}^y)\cos\phi^* + (P_x R_{LT}^x + P_z R_{LT}^z)\sin\phi^*] + \\ &+ \epsilon[(R_{TT}^0 + P_y R_{TT}^y)\cos 2\phi^* + (P_x R_{TT}^x + P_z R_{TT}^z)\sin 2\phi^*] + \\ &+ h\sqrt{2\epsilon_L(1-\epsilon)}[(R_{LT'}^0 + P_y R_{LT'}^y)\sin\phi^* + (P_x R_{LT'}^x + P_z R_{LT'}^z)\cos\phi^*] + \\ &+ h\sqrt{1-\epsilon^2}[P_x R_{TT'}^x + P_z R_{TT'}^z]\}. \end{aligned} \tag{1.7}$$

In this expression the electron spin is assumed to be longitudinal [1] and is represented by the helicity h, while the target polarization is described in the frame $\{\hat{x}, \hat{y}, \hat{z}\}$ where the z axis is in the direction of the virtual photon, the y axis is perpendicular to the hadronic plane and the x axis is given by $\hat{x} = \hat{y} \times \hat{z}$ (see figure 1.3).
As the formula indicates, the new response functions can be measured both by detecting the angular distribution of the outgoing pion or by measuring spin asymmetries obtained reversing the electron and/or target spin. It is in fact natural to define three independent asymmetries given by

$$\begin{aligned} A_e &= \frac{\sigma(+h_e,) - \sigma(-h_e)}{\sigma(+h_e) + \sigma(-h_e)} \\ A_t &= \frac{\sigma(+h_N) - \sigma(-h_N)}{\sigma(+h_N) + \sigma(-h_N)} \\ A_{et} &= \frac{\sigma(+h_e,+h_N) + \sigma(-h_e,-h_N) - \sigma(+h_e,-h_N) - \sigma(-h_e,+h_N)}{\sigma(+h_e,+h_N) + \sigma(-h_e,-h_N) + \sigma(+h_e,-h_N) + \sigma(-h_e,+h_N)} \end{aligned} \tag{1.8}$$

These quantities, and the response functions that determine them, give an additional mean to extract information on the helicity amplitudes. The advantage of the spin observables is that many of these terms result from interference between different amplitudes. Therefore when searching for small components, these observables become more effective than a simple unpolarized cross-section. In this situation the interference with a larger components of the process makes the spin observable to behave linearly in the small amplitude. Consequently, its determination becomes considerably easier than from an unpolarized measurement where it would occur quadratically.
It is worth to notice that some of these functions, as for example $R_{TL'}$, are accessible only in out of plane measurements since their contribution would vanish for $\phi^* = 0$. This feature, together with the intrinsic complexity of polarized scattering experiments, is one of the reasons why very little is known about the polarized response functions in spite of their importance.

---

[1] The contribution of transverse electron polarization are suppressed due to kinematics by a factor $1/\gamma$

1.3 Electro-excitation of the Baryonic Resonances

In the last three decades, several experiments in photo and electroproduction have been completed in Mainz, Bonn, Desy, NINA. The results of these experiments, mainly cross-section and angular distribution measurements, together with the results from πN scattering, represent the main source of knowledge on the baryonic resonances presently available [9].
In spite of the large amount of new information that was accumulated, these measurements have left several open questions, from the Q^2 dependence of the E_{1+}/M_{1+} ratio of the $P_{33}(1232)$ resonance, to the puzzle of the structure of the Roper resonance, to the search for the missing resonances. Following this line of research, a new generation of experiments is now in progress at Jefferson Lab, Mainz, Elsa, LEGS, GRAAL. These new experiments are using high duty cycle machines and large acceptance detectors not available at the time of the first attempts, improving both the quality of the information that can be extracted and the kinematical coverage of the measurement. Furthermore for the first time the proposed measurements include an extensive study of polarization observable that, as stressed before, may become a fundamental tool in this research field. At present in fact only few measurement of polarization observables are available in single pion photoproduction from Mainz[10], GRAAL[11] and LEGS[12], while in electroproduction only few points of the electron asymmetry in the $\Delta(1232)$ region are available from Bates [13] and no measurement with polarized beam and target have been performed in the resonance region.
In the following I will discuss a few examples that illustrate what the present status of the research on the baryonic resonances is and how the new experiments and, in particular the measurement of spin observables, may help in completing our knowledge.

1.3.1 The Electro-excitation of the $P_{33}(1232)$ Resonance

The $P_{33}(1232)$ or Delta resonance has been the most studied of all the baryonic resonances since is the most accessible. It is in fact the only resonance that does not strongly overlap with other excited states and its only strong decay is by single pion emission. The resonance has been studied mainly in $ep \to ep\pi^0$ and $ep \to en\pi^+$, but also data on $en \to ep\pi^-$ are available.
In the pure SU(6) model, the $P_{33}(1232)$ is in the lowest $[56, 0^+]$ multiplet. At low Q^2 in the non-relativistic quark model the $N \to P_{33}$ excitation is characterized by a single quark spin-flip transition with $\Delta L = 0$. This transition is therefore completely determined by the M_{1+} multipole [14]. Since, anyhow, the SU(6) symmetry is broken by the color hyperfine interaction, the Delta wave function is characterized by a mixture a $L = 0$ and $L = 2$ configuration. This implies that an E_{1+} multipole contribution to the transition is possible. This contribution is predicted to be of the order of few percents since the $SU(6)$ breaking is of the same level. The measurement of the relative strength of the two multipoles and in particular of the ratio E_{1+}/M_{1+} is therefore fundamental as a test of the quark model prediction.
The measures at low Q^2, including the photoproduction data, are consistent with the dominance of the M_{1+} over the E_{1+} multipole as shown in figure 1.6. The electroproduction data indicates in fact that the E_{1+}/M_{1+} ratio is small and, for most of the data

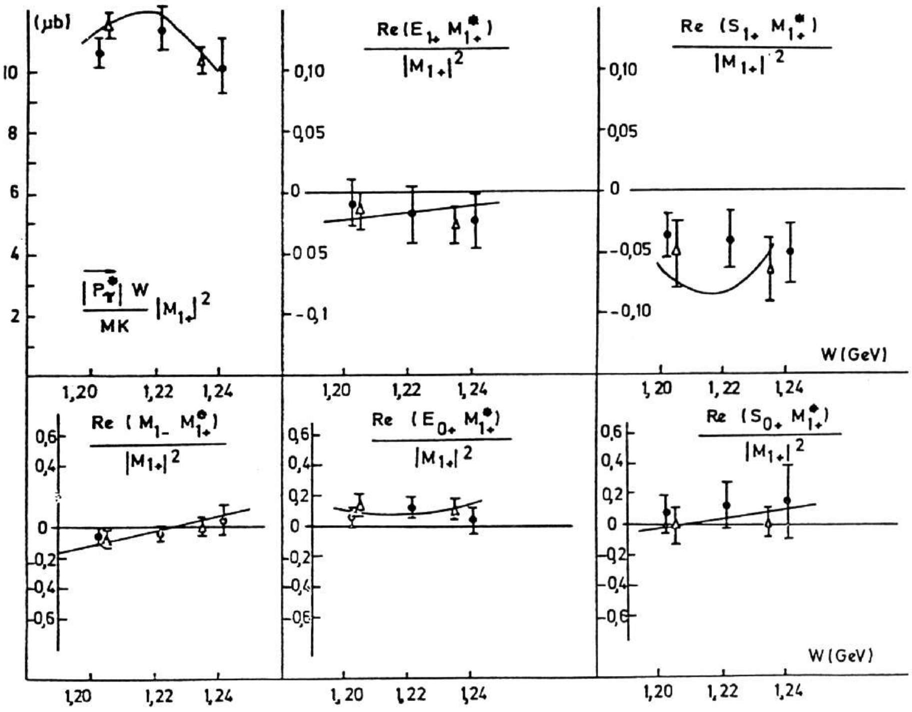

Figure 1.5: *Multipole analysis of $\gamma_v p \to \pi^0 p$ in the $P_{33}(1232)$ region. The data shown are from Bonn [16].*

points, consistent with zero. The more recent photoproduction point from Mainz [15] indicates that at $Q^2 = 0$ the ratio is negative with a value of $(-2.5 \pm 0.2 \pm 0.2)\%$. On the other side, for the high Q^2 limit, pQCD predictions indicates that the E_{1+}/M_{1+} ratio should approach one. This is a direct consequence of the helicity conservation and implies that the multipole ratio and therefore the structure of the nucleon-delta transition should have a dramatic change going form the photon point to the high Q^2 limit. The occurrence of the predicted transition can provide a fundamental insight in hadronic physics since it may indicate the regime where the idea of constituent quark need to be substitute by other degrees of freedom as current quarks.
The data used for the plot in figure 1.6 were obtained using a multipole analysis of the angular distribution of the Delta decay. In the assumption of the M_{1+} dominance, the single pion cross-section in the P_{33} region can be written as

$$
\begin{aligned}
\frac{d\sigma}{d\Omega} &\approx \frac{\mathbf{p}_\pi W}{KM}\Big[\frac{5}{2}|\, M_{1+}|^2 - 3\mathcal{R}e(M_{1+}E^*_{1+}) + \mathcal{R}e(M_{1+}M^*_{1-}) \\
&+ \; 2\cos\theta^*\mathcal{R}e(E_{0+}M^*_{1+}) \\
&+ \; \cos^2\theta^*\left(-\frac{3}{2}|M_{1+}|^2 + 9\mathcal{R}e(M_{1+}E^*_{1+}) - 3\mathcal{R}e(M_{1-}M^*_{1+})\right) \\
&+ \; \epsilon\sin^2\theta^*\cos 2\phi^*\left(-\frac{3}{2}|M_{1+}|^2 - 3\mathcal{R}e(M_{1+}E^*_{1+})\right) \\
&- \; \sqrt{2\epsilon_L(1-\epsilon)}\sin\theta^*\cos\phi^*\left(\mathcal{R}e(S_{0+}M^*_{1+}) + 6\cos\theta^*\mathcal{R}e(S_{1+}M^*_{1+})\right)\Big]
\end{aligned}
\tag{1.9}
$$

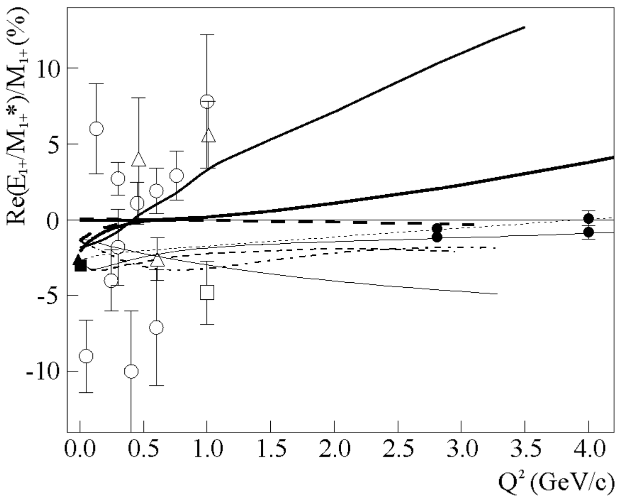

Figure 1.6: *Ratio $\mathcal{R}e(E_{1+}M_{1+})/|M_{1+}|^2$ at the $P_{33}(1232)$ mass from electroproduction experiments. The open points correspond to the old measurement from ref. [16, 17, 18, 19, 20, 22, 23]. The full points are the most recent measurement from ref. [10, 12, 25] (plot courtesy of L.C.Smith and K.Joo).*

where the structure function of formula 1.6 has been substituted by their multipole expansion up to p-waves [2].
Measuring the θ^* and ϕ^* distribution of the cross section is therefore possible to extract the resonant terms

$$|M_{1+}|^2,\ \mathcal{R}e(M_{1+}E^*_{1+}),\ \mathcal{R}e(M_{1+}S^*_{1+})$$

and the non resonant terms

$$\mathcal{R}e(E_{0+}M^*_{1+}),\ \mathcal{R}e(S_{0+}M^*_{1+}),\ \mathcal{R}e(M_{1-}M^*_{1+}).$$

As shown in figure 1.5 that gives an example of this technique, these analyses are intrinsically complicated since the size of the magnetic multipole is much larger than the non-dominant contribution and an high degree of precision is necessary to obtain accurate results. In addition, the multipoles that are extracted with this technique can contain a significant non-resonant contribution that makes hard a direct comparison with theoretical models. Finally as shown in figure 1.6, the data points presently available are not sufficient to discriminate between different models. The same is valid for the ratio of the coulombian multipole S_{1+} over M_{1+} (see figure 1.7).
The experiments that are now in progress have planned measurements both of the single and double spin observables in addition to the cross-section measurement. The double spin observable, namely the structure function $R^z_{TT'}$, is in fact rather sensitive to the size of the E_{1+}/M_{1+} ratio. In fact, a ratio of the order of few percents is already expected for particular kinematics to change the sign of the double spin asymmetry. Furthermore while the cross-section measurement give access to the real part of interference terms as $\mathcal{R}e(E_{1+}M^*_{1+})$ or $\mathcal{R}e(S_{1+}M^*_{1+})$, the single spin asymmetry allows the study of their

[2]Since the Δ decay is in $L = 1$ wave, in the resonance region is reasonable to use the expansion up to p-waves

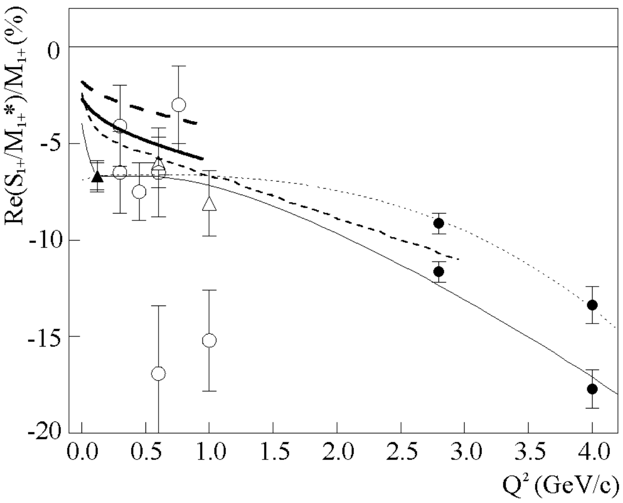

Figure 1.7: *Ratio $\mathcal{R}e(S_{1+}M_{1+})/|M_{1+}|^2$ at the $P_{33}(1232)$ mass from electroproduction experiments, The open points correspond to the old measurement from ref. [16, 17, 18, 19, 20, 22, 23]. The full points are the most recent measurement from ref. [10, 12, 25] (plot courtesy of L.C.Smith and K.Joo).*

imaginary parts $\mathcal{I}m(E_{1+}M^*_{1+})$ or $\mathcal{I}m(S_{1+}M^*_{1+})$ that would not be otherwise accessible. These quantities are obviously very sensitive to the phase relation between the different multipoles since they would vanish identically if the multipoles were strictly in phase. The electron beam asymmetry, in particular, in the assumption of M_{1+} dominance is proportional to

$$-\left[\mathcal{I}m(S_{0+}M^*_{1+}) + 6\cos\theta^*\mathcal{I}m(S_{1+}M^*_{1+})\right].$$

As mentioned above, the second interference term would vanish if the multipoles contain resonant contribution from the P_{33} only. Any deviation from zero would indicate the existence of additional non-resonant contribution to the S_{1+} multipole in isospin 1/2 channel.

1.3.2 The Roper Resonance

The $P_{11}(1440)$ or Roper resonance is a well established 4-star nucleon resonance found in πN scattering [26]. In pion photoproduction, its contribution appears as a definite shoulder on the $D_{13}(1520)$-$S_{11}(1535)$ resonances but in electroproduction its existence remains uncertain. In the non relativistic quark model (NRCQM), the $P_{11}(1440)$ is interpreted as a radial excitation of the nucleon within the SU(6)×O(3) multiple $[56, 0^+]$ (L=0, N=2). However this hypothesis is characterized by several contradictions. The mass of this state lies in fact considerably below the excitation energy typically expected for a N=2 state. Even when SU(6) mixing induced by the hyperfine interaction is invoked, the state is still 150-200MeV below the expected mass. In addition, the photocoupling amplitude $A_{1/2}$ predicted within the framework of the NRCQM has the wrong sign and magnitude [27]. The measured Q^2 dependence of $A_{1/2}$ is in fact quite different from the result of quark model calculation (see figure 1.3.2). The data indicates a rapid fall off of

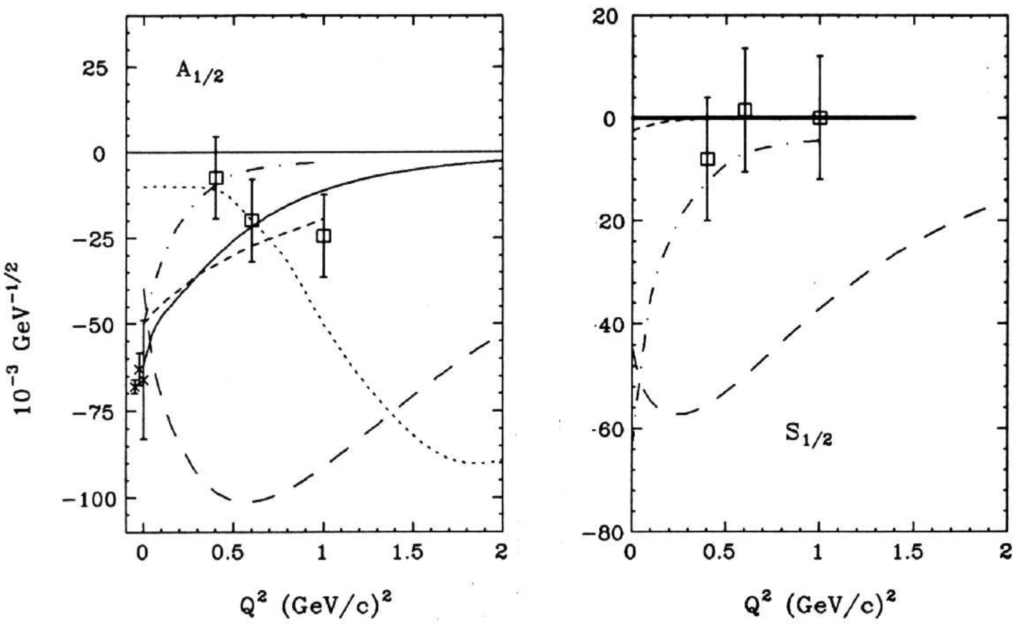

Figure 1.8: *Transverse (left) and longitudinal (right) photocoupling amplitudes for the Roper resonance as measured on proton target. The data point and the short-dashed and dashed-dotted lines are from reference [31]. The long-dashed and solid-lines are the calculation in the assumption of the $[q^3]$ and $[q^3g]$ state respectively.*

the absolute value of the amplitude with Q^2 while the predictions shows a weaker fall off or even an initial rise with Q^2. Furthermore the longitudinal amplitude $S_{1/2}$ shows the same discrepancy from the expected behavior. In fact if the Roper is a radial excitation, then the transition should have a large longitudinal component. An indication of a possible enhancement in the L/T ratio close to the P_{11} position for $Q^2 \sim 1\mathrm{GeV}^2/\mathrm{c}^2$ was found in an evaluation of the existing inclusive data (see ref. [28]) but the longitudinal amplitude is still in disagreement with the theoretical prediction (see figure 1.3.2).

Recent theoretical developments have indicated a possible description of the Roper resonance as an hybrid state composed by 3 quarks and a gluon ($[q^3g]$) [29, 30]. The existence of hybrid mesons has already been predicted by lattice calculation, and even if no such calculations have been performed for baryons, estimates within the framework of the bag models yield masses for the lowest P_{11}^G state around 1.5 GeV. With the introduction of gluonic degrees of freedom, the wave function of the nucleon may be written as

$$|N> = \frac{1}{\sqrt{1+2\delta^2}} \left[|N_0> - \delta(|^4N_g> + |^2N_g>) \right] \tag{1.10}$$

where $|N_0>$ represents the wave function of the 3-quark system, which transforms as a $[56, 0^+]$ state, $|^4N_g>$ and $|^2N_g>$ are the wave function of the q^3g state with spin 3/2 and 1/2 respectively. The parameter δ describe the gluon-quark interaction. The corresponding excited state, orthogonal to the nucleon in the spin-flavor space is

$$|N^*> = \sqrt{\frac{2}{1+2\delta^2}} \left[\delta |N_0> + \frac{1}{2}(|^4N_g> + |^2N_g>) \right]. \tag{1.11}$$

This description predicts a neutron/proton ratio of the $A_{1/2}$ amplitude of -2/3, that agrees with the quark model estimate and with the experimental results.
An interesting result based on the hybrid assumption is that in the $\gamma_v p \rightarrow P_{11}$ excitation, since the gluon has only transverse excitation modes, the longitudinal components is absent. This implies

$$S_{1/2}(Q^2) = 0$$

in agreement with the available data.
The solution of the puzzle regarding the Roper structure would obviously have an enormous impact on our understanding of the baryon structure and the dynamics of the strong interaction in non-perturbative regime. From the plots shown on the Roper topic, it is evident that more accurate data are needed.
In particular a precise measurement of the Q^2 dependence of the transverse photocoupling amplitude would discriminate between the interpretation of the P_{11} as a 3-quark state or as a gluonic excitation. The discriminating power results from the fact that in the hybrid case the 3-quark system transforms within the SU(6) [70] multiplet. This different spectroscopic assignment leads to a different Q^2 dependence of the amplitude that in first approximation are

$$\frac{A_{1/2}[q^3 g]}{A_{1/2}[q^3]} \sim \frac{1}{Q^2} \tag{1.12}$$

One of the more favorable observable that could provide accurate measurement of the photocoupling amplitudes is the helicity asymmetry A_1, defined as

$$A_1 = \frac{A^2_{1/2} - A^2_{3/2}}{A^2_{1/2} + A^2_{3/2}}. \tag{1.13}$$

and directly accessible with double polarization measurement.
This quantity is in fact positive for the Roper while is expected to be negative for the Delta with a value, in the case of M_{1+} dominance, of -1/2. Therefore different assumption regarding the Roper structure would show up in the W dependence of A_1.

1.3.3 Helicity Structure of the $D_{13}(1520)$ and $F_{15}(1680)$

The $D_{13}(1520)$ and $F_{15}(1680)$ are the dominant contributions at low Q^2 in the second and third bumps that appear in the inclusive cross section. Their contribution persists also with increasing Q^2, at least up to $3\mathrm{GeV}^2/\mathrm{c}^2$. At present, in fact measurements of the helicity amplitudes of these two resonances exist up to this Q^2 even if with large error bars.
The photoproduction data have shown a very peculiar feature for these two state [32]. In $\gamma p \rightarrow \pi^+ n$, the total cross section shows three clear peaks which are dominantly the $P_{33}(1232)$, the $D_{13}(1520)$ and the $F_{15}(1680)$ respectively. However, for the collinear production (θ^*=0) the first peak is seen but the second and third has vanished (see figure 1.9). In this kinematics, only s-waves can contribute and therefore the cross section is determined by the helicity-1/2 amplitude alone. Consequently, one infers that at the photon point the excitation of the D_{13} and F_{15} off protons is entirely in the $A_{3/2}$ mode, i.e.

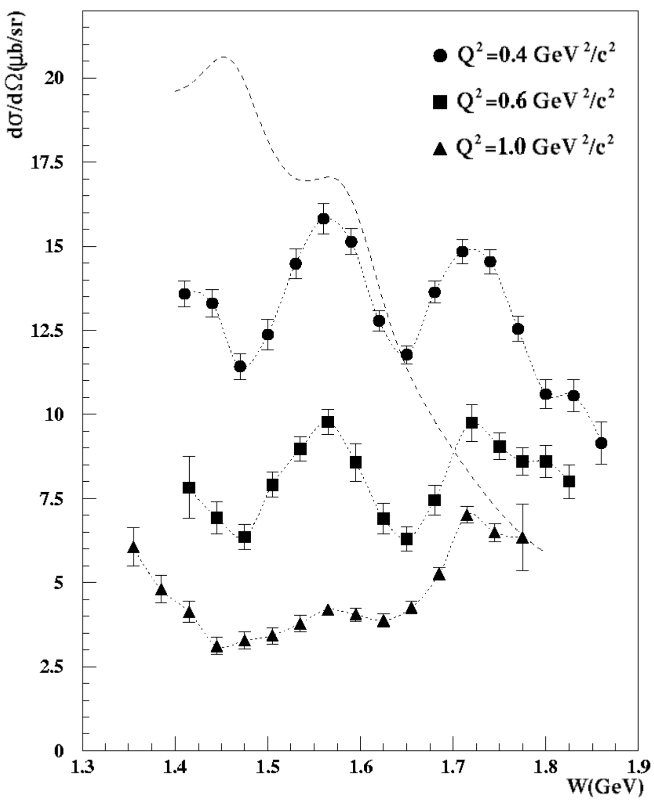

Figure 1.9: *Differential cross section at 0° for different Q^2 values. The dashed line is a fit of the photoproduction data from reference [32]. The data points are from DESY [20, 21] and NINA [24]. The dotted line that connects the points is introduced to guide the eye.*

$$A^p_{1/2}(D_{13}, F_{15}) \approx 0$$

On the contrary electroproduction data indicate that at higher Q^2 the $A_{1/2}$ amplitude is dominant over the $A_{3/2}$ amplitude. The helicity asymmetry A_1 in fact shows a dramatic transition from the -1 value valid at $Q^2 = 0$ to the +1 value at higher momentum transfer (see figure 1.9 and 1.10).

This particular feature can be explained in the framework of the constituent quark model. In the NRCQM the D_{13} belongs to the $[70, 1^-]$ multiplet while the F_{15} is in the $[56, 2^+]$ with excitation energy of $2\hbar\omega$. The transition to these excited state can be written as a sum of spin-flip and orbital-flip matrix element [27]. The resulting photocoupling amplitudes satisfy the relations

$$\frac{A^p_{1/2}}{A^p_{3/2}}(D_{13}) = -\frac{1}{\sqrt{3}}\left(1 - \frac{g\mathbf{q}^2}{\alpha^2}\right) \tag{1.14}$$

$$\frac{A^p_{1/2}}{A^p_{3/2}}(F_{15}) = -\frac{1}{\sqrt{2}}\left(1 - \frac{g\mathbf{q}^2}{2\alpha^2}\right).$$

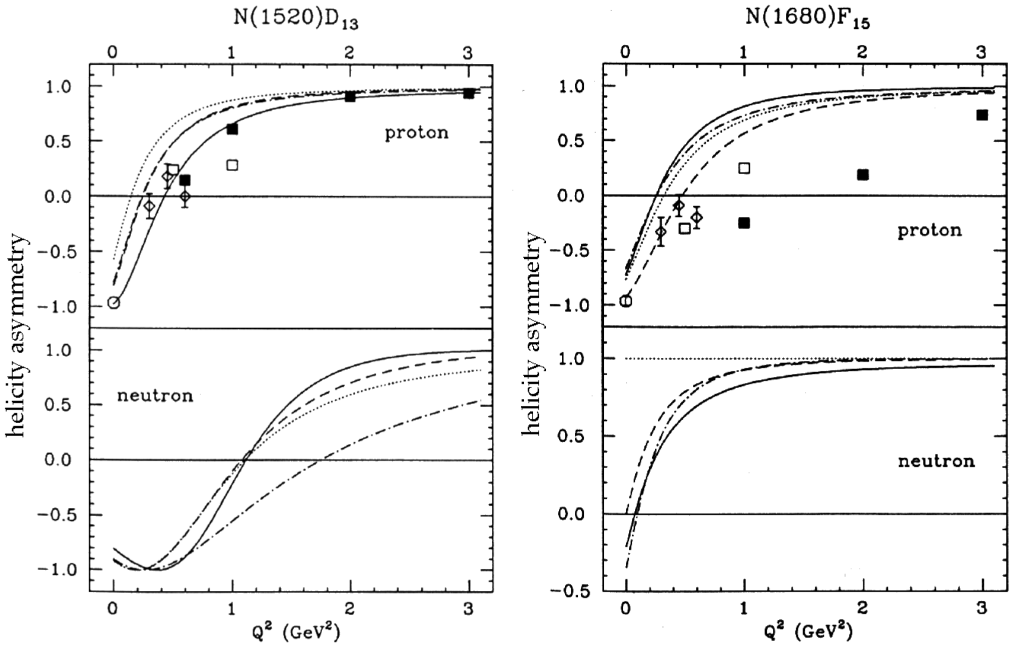

Figure 1.10: *Helicity asymmetry for the transitions $\gamma_v p \to D_{13}$ (left) and $\gamma_v p \to F_{15}$ (right). The plotted lines are the result of calculations by Capstick [29], with different correction to the NRCQM. The data are from reference [37]($Q^2 = 0$, from reference [38] (diamonds), from reference [24] (open squares), and from reference [39, 40] (solid squares).*

The $g\mathbf{q}^2$ term comes from the spin-flip matrix element, where $\mathbf{q}$ is the three-momentum transfer, g is the gyromagnetic ratio for the constituent quarks and α the harmonic oscillator parameter. The two ratios can be made to vanish by choosing $\mathbf{q}^2 = 2\alpha^2/g$. This condition can be satisfied simultaneously for the two excited states by selecting $g = 1$ and $\alpha = 0.17\mathrm{GeV}^2$, and writing the three-momentum transfer in the lab frame. In fact in the laboratory frame for $Q^2 = 0$, $\mathbf{q}^2(F_{15}) \approx 2\mathbf{q}^2(D_{13})$. This result of the quark model leaves many open questions. First of all it is derived in the laboratory frame. In addition, a gyromagnetic ratio of 1 implies a mass for the constituent quarks of $\approx 340MeV$. Hence the use of a non-relativistic approach is unjustified. In particular the spin-orbit term could be important in the interaction. Nevertheless this derivation is considered one of the success of NRCQM.

If one now considers the electroproduction process instead of photoproduction the cancellation between $\mathbf{q}^2$ and α^2/g does not occur any more. The three-momentum transfer depends in fact both on the resonance mass and on the photon mass and therefore is value changes with Q^2. As a matter of fact the $A_{1/2}$ amplitudes is already predicted to be dominant for $Q^2 > 0.5\mathrm{GeV}^2/\mathrm{c}^2$.

This feature was first observed in the model when no data supporting it were available. Later on the electroproduction measurement confirmed this prediction as shown in figure 1.10. Nevertheless those data are not yet sufficient to discriminate between different corrections to the original calculation.

1.4 The Physics Program with Polarized Beam and Target at CLAS

Because of the importance of polarization observables in resonance physics, a significant portion of the CLAS physics program has been dedicated to such measurements. The program includes measurements of both inclusive and exclusive reactions as listed below.

- measurement of polarized structure functions in inelastic electron-proton scattering [41];
- measurement of the structure function G_1^n and of the Q^2 dependence of the Gerasimov-Drell-Hearn sum rule for the neutron [42];
- measurement of spin asymmetries in single pion electroproduction from the proton using polarized beam and target [43];
- study of the $\Delta(1232)$ using double polarization asymmetries [44];
- measurement of spin asymmetries in the reaction $\gamma_v n \to \pi^- p$;
- study of the helicity structure of single pion photoproduction on proton [45];
- measurement of the electron spin asymmetry in $p(e, e'p)\pi^0$ and $p(e, e'\pi^+)n$ in the mass region of the $P_{33}(1232)$ [46] [3].

The proposed inclusive measurements aim at the extraction of the polarized structure functions on proton and neutron. Similar measurements have been performed at SLAC, SMC and HERMES [47, 48, 49], mapping out the deep inelastic region. On the contrary the CLAS experiments cover the low Q^2 region providing information regarding the resonance spin structure (see figure 1.11). These data will also allow the test of the Gerasimov-Drell-Hearn sum rule [50, 51] and of the Ellis-Jaffe sum rule [52].
The other listed proposals are relative to single pion electroproduction (π^+, π^0 and π^-) both on proton and neutron with the purpose of obtaining a complete isospin decomposition of the process.
These measurements require the same experimental configuration and have therefore been included in the same run period, called EG1 (Electron and Gamma polarized beams). As discussed in section 2.9 the CLAS characteristics allow in fact the combination of different measures in a single data taking period. The EG1 run was performed from September to November 1998 providing an impressive amount of data (see section 5.2). A second run, EG2000, has started in September 2000 and will be concluded in February 2001, completing the approved experiments. As shown in figure 1.11, this second run includes also a high energy part that leads to a significant enlargement of the kinematical coverage of the experiments.
The results discussed in this thesis are relative to the measurements of spin asymmetries in the $p(e, e'\pi^+)n$ channel and in particular to the extraction of the double spin asymmetry [43].
In the following section I will describe the particular kinematics of the EG1 run, introducing the precise definition of the spin observables whose measurements is discussed here.

[3] While the other listed experiments have been included in the EG1 run period, this experiments is included in the E1 run (polarized electron beam on liquid hydrogen target) since it does not require the polarized target.

1.4.1 EG1 Kinematics

In the configuration of the EG1 experiment, the target polarization is parallel to the direction of the electron beam and therefore the polarization vector is

$$(P_x, P_y, P_z) = P_t(\sin\theta_\gamma \cos\phi^*, -\sin\theta_\gamma \sin\phi^*, \cos\theta_\gamma),$$

where θ_γ denotes the angle between the virtual photon and the incident electron and ϕ^* the angle between the hadronic and leptonic planes (see figure 1.3). In this case the cross section introduced in eq. 1.7 becomes

$$\begin{aligned}
\frac{d\sigma_v}{d\Omega^*_\pi} &= \frac{|\mathbf{q}|}{q_\gamma^{CM}}\{R_T^0 - P_t R_T^y \sin\theta_\gamma \sin\phi^* + \epsilon_L(R_L^0 - P_t R_L^y \sin\theta_\gamma \sin\phi^* + \\
&+ [2\epsilon_L(1+\epsilon)]^{1/2}[R_{LT}^0 \cos\phi^* + P_t \sin\theta_\gamma (R_{LT}^x - R_{LT}^y)\sin\phi^* \cos\phi^* + \\
&+ P_t R_{LT}^z \cos\theta_\gamma \sin\phi^*] + \epsilon[R_{TT}^0 \cos 2\phi^*_\pi \\
&+ P_t \sin\theta_\gamma (R_{TT}^x \sin 2\phi^* \cos\phi^* - R_{TT}^y \cos 2\phi^* \sin\phi^*) + \\
&+ P_t R_{TT}^z \cos\theta_\gamma \sin 2\phi^*] + P_e\sqrt{2\epsilon_L(1-\epsilon)}[R_{LT'}^0 \sin\phi^* + \\
&+ P_t \sin\theta_\gamma (R_{LT'}^x \cos^2\phi^* - R_{LT'}^y \sin^2\phi^*) + \\
&+ P_t R_{LT'}^z \cos\theta_\gamma \cos\phi^*] + \\
&+ P_e\sqrt{1-\epsilon^2}[P_t(R_{TT'}^x \sin\theta_\gamma \cos\phi^*_+ R_{TT'}^z \cos\theta_\gamma)]\}
\end{aligned} \tag{1.15}$$

The spin dependence of the previous formulas can be schematically summarized as[4]

$$\frac{d\sigma_v}{d\Omega^*_\pi} = \frac{|\mathbf{q}|}{q_\gamma^{CM}}\left\{\frac{d\sigma_0}{d\Omega^*_\pi} + P_e\frac{d\sigma_e}{d\Omega^*_\pi} + P_t\frac{d\sigma_t}{d\Omega^*_\pi} - P_eP_t\frac{d\sigma_{et}}{d\Omega^*_\pi}\right\} \tag{1.16}$$

with

$$\begin{aligned}
\frac{d\sigma_0}{d\Omega^*_\pi} &= \left\{R_T^0 + \epsilon_L R_L^0 + \sqrt{2\epsilon_L(1+\epsilon)}R_{LT}^0 \cos\phi^* + \epsilon R_{TT}^0 \cos 2\phi^*\right\} \\
\frac{d\sigma_e}{d\Omega^*_\pi} &= \sqrt{2\epsilon_L(1-\epsilon)}R_{LT'}^0 \sin\phi^* \\
\frac{d\sigma_t}{d\Omega^*_\pi} &= -(R_T^y + \epsilon_L R_L^y)\sin\theta_\gamma \sin\phi^* + \\
&+ \sqrt{2\epsilon_L(1+\epsilon)}[\sin\theta_\gamma (R_{LT}^x - R_{LT}^y)\sin\phi^* \cos\phi^* + R_{LT}^z \cos\theta_\gamma \sin\phi^*] + \\
&+ \epsilon[\sin\theta_\gamma (R_{TT}^x \sin 2\phi^* \cos\phi^* - R_{TT}^y \cos 2\phi^* \sin\phi^*) + R_{TT}^z \cos\theta_\gamma \sin 2\phi^*]
\end{aligned}$$

[4]The minus sign introduced in the double spin term has been chosen because with this notation the σ_{et} has the same sign of the helicity asymmetry A_1 as defined previously.

$$
\begin{aligned}
\frac{d\sigma_{et}}{d\Omega_\pi^*} &= \sqrt{2\epsilon_L(1-\epsilon)}[\sin\theta_\gamma(R^x_{LT'}\cos^2\phi^* - R^y_{LT'}\sin^2\phi^*) + R^z_{LT'}\cos\theta_\gamma\cos\phi^*] + \\
&- \sqrt{1-\epsilon^2}[R^x_{TT'}\sin\theta_\gamma\cos\phi^* + R^z_{TT'}\cos\theta_\gamma].
\end{aligned}
$$

Therefore the three spin asymmetry introduced in section 1.2 are simply given by

$$
\begin{aligned}
A_e &= \frac{\sigma_e}{\sigma_0} \\
A_t &= \frac{\sigma_t}{\sigma_0} \qquad (1.17)\\
A_{et} &= \frac{\sigma_{et}}{\sigma_0}
\end{aligned}
$$

The goal of this analysis is to extract these spin asymmetries, in particular the double spin asymmetry A_{et} .

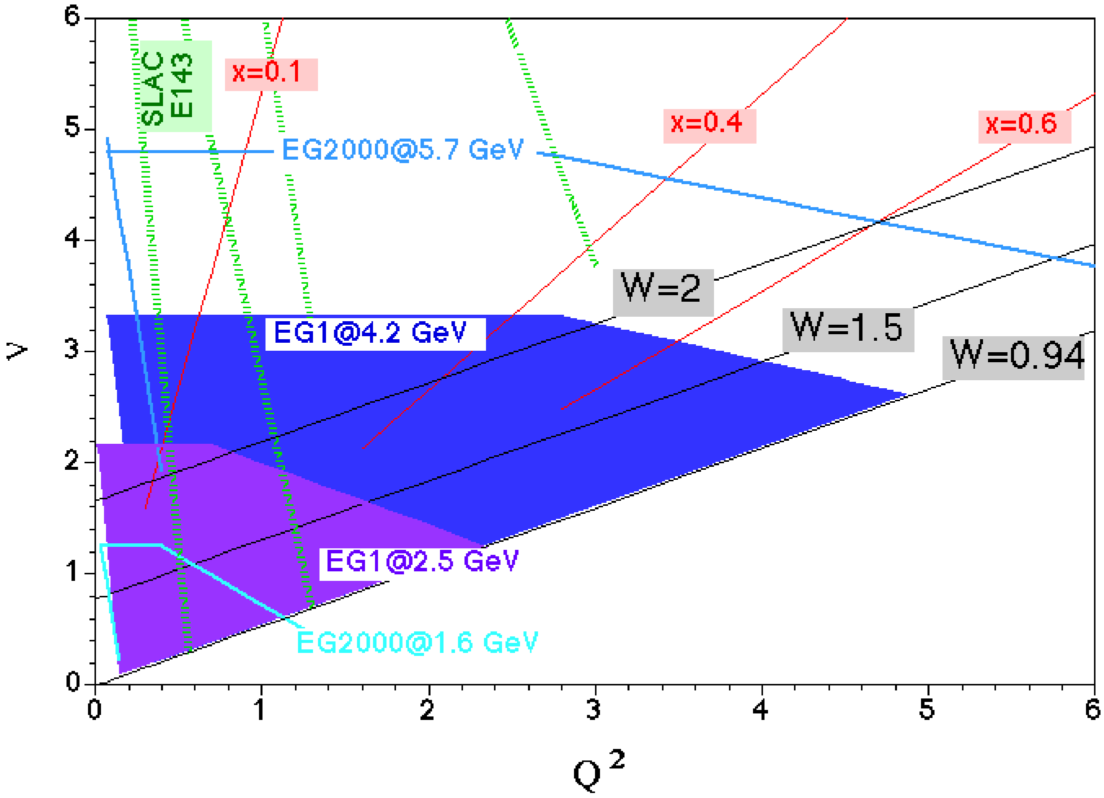

Figure 1.11: *Kinematical region accessible with CLAS in the EG1 and EG2000 runs.*

Chapter 2

The CLAS Detector

2.1 Introduction

The main purpose of the Jefferson Laboratory facility is the basic research in intermediate energy and nuclear physics using electromagnetic probes. Presently most of the available knowledge is essentially limited to the electromagnetic structure of the nucleon as explored in inclusive (e, e') experiments and to the lowest excited states of the baryonic spectrum. In contrast little is known about the higher excited states and to multi-particle final states. The reasons of this limitation can be found in the technical characteristics of previous accelerator facilities and detector equipments. The low duty cycle of several existing electron accelerators makes coincidence experiments difficult. In fact the measurements are limited to the narrow kinematical regions were a sufficient ratio of real-accidental coincidences can be obtained. In addition the standard equipment used at electron accelerator is based on magnetic spectrometers that, in spite of a high resolution ($dp/p \sim 10^{-4}$), cover small solid angles (10^{-3} of 4π) and small momentum range ($\Delta p/p \sim 10\%$). These characteristics allow precise measurements in a limited kinematical range but prevents from detecting many particles final states that would require a large acceptance. Finally experiments in which the luminosity is limited by external factor as beam intensity or target density are practically ruled out.
The solution to these problems is represented by large acceptance spectrometers that used in conjunction with high duty cycle electron beams allow the study of exclusive reactions characterized by multi-particle final states, with high rates and low background. The continuous high quality electron beam (halo-free, 100% duty cycle) of the CEBAF accelerator is ideally suited for the operation of this kind of spectrometer. The CLAS (**C**EBAF **L**arge Acceptance **S**pectrometer) spectrometer in Hall B has in fact been designed for experiments in which the final hadronic states are characterized by several uncorrelated particles or which the luminosity is limited by beam, target or accidental background. CLAS is a magnetic toroidal multigap spectrometer in which the magnetic field is generated by six superconducting coils (see figure 2.1). The particle detection system is based on drift chambers for track reconstruction, Cerenkov counters for electron-pion discrimination, scintillation counters for the time of flight measurement, and electromagnetic calorimeter to identify electrons and neutrals. The six segment are instrumented individually to form six independent spectrometers and leave a field free region in the center of the detector suited for the insertion of a polarized target as described in chapter 3. In

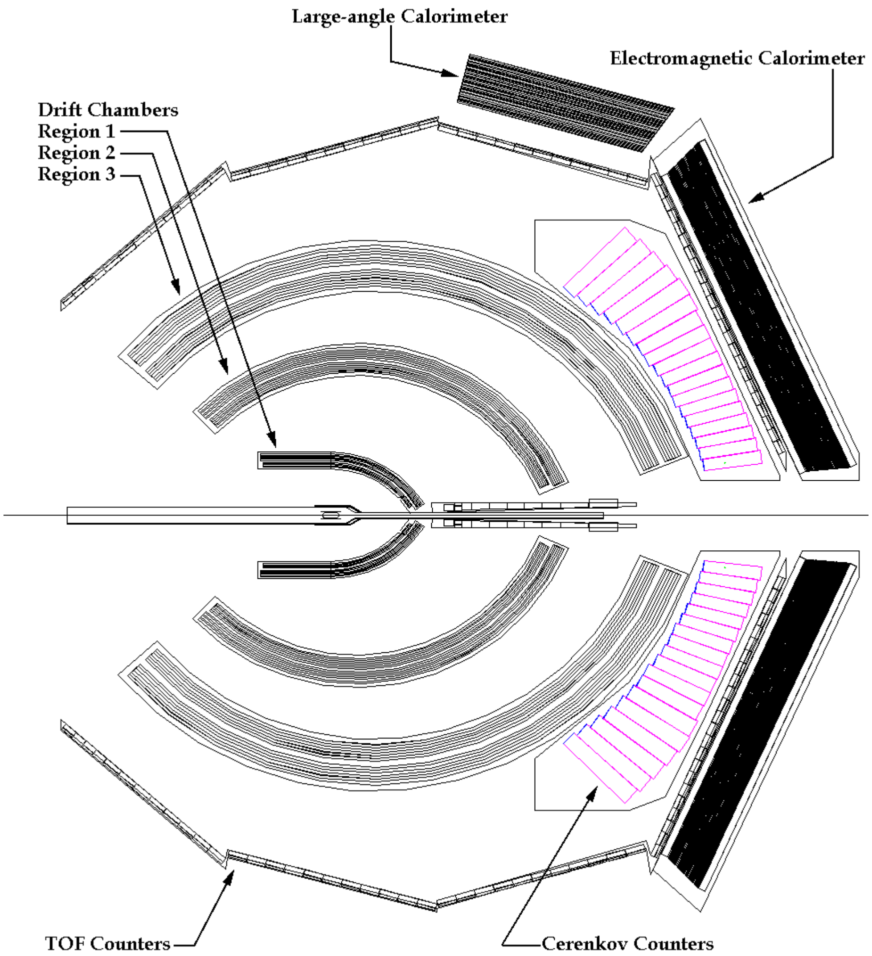

Figure 2.1: *Schematic drawing of the CLAS detector showing a section along the beamline.*

the following the main characteristic of the single detector systems will be discussed as well as of the CEBAF accelerator and beam.

2.2 CEBAF Continuous Electron Beam

The Continuous Electron Beam Accelerator Facility is based on superconducting RF cavities operated in continuous wave (CW) mode. A schematic of the machine is shown in figure 2.2. The electrons, emitted at the injector at an energy of 40 MeV, are accelerated through the two linacs. These are connected on both ends by a set of five recirculating arcs. The accelerating power in each linac is supplied by the 40 niobium cavities separated into 8 cryomodules cooled with liquid helium. The cavities operate at a minimum gradient of 5 MeV per meter and at a frequency of 1.497 GHz. For each turn the electron beam receives a boost of approximately 800 MeV allowing a maximum energy of 4GeV after the 5 passes.
Beam can be delivered simultaneously at the three experimental Halls (Hall A, Hall B and Hall C). Because of the RF frequency of the niobium cavities, the beam is structured in microbunches separated by approximately 0.67 ns. These are delivered in sequence to the three Halls. The microbunches can be accelerated to different energies by recirculating them through a different number of passes so that the beam in the three halls can either be at the same energy or at different multiples of the one pass energy. In addition the bunches can be loaded with different electron densities to provide independent beam currents in the three halls. The three beams are finally separated at the switchyard and delivered to the experimental areas with a separation between the closest bunches of 2.04 ns.
Due to the virtual lack of synchrotron radiation, the energy spread in the beam is approximately $\Delta E/E \sim 10^{-4}$. The accelerator can deliver beam currents ranging from 100 pA to 100 μA.
At present the performances of the machine are significantly above the original specification and a maximum energy of 5.7 GeV has already been reached and maintained in normal operation.
The end stations are equipped with spectrometers for complementary experimental programs. Hall C contains two magnetic spectrometers of medium resolution with $\Delta p/p \leq 10^{-3}$ but different maximum momenta: the High Momentum Spectrometer (HMS) and the Short Orbit Spectrometer (SOS) have respectively maximum momenta of 7 GeV/c and 1.8 GeV/c. Hall A is equipped with two High Resolution Spectrometers (HRS) with $\Delta p/p \leq 10^{-4}$ and maximum momentum of 4 GeV, instrumented for electron and hadron detection. Hall B houses the CEBAF Large Acceptance Spectrometer dedicated to exclusive multi-particle final state measurements.

2.3 The Polarized Electron Beam

Since 1998 the CEBAF electron beam is polarized. The polarization is obtained using the GaAs cathode technique. For this purpose the thermoionic gun used up to that time was substituted with a polarized gun.

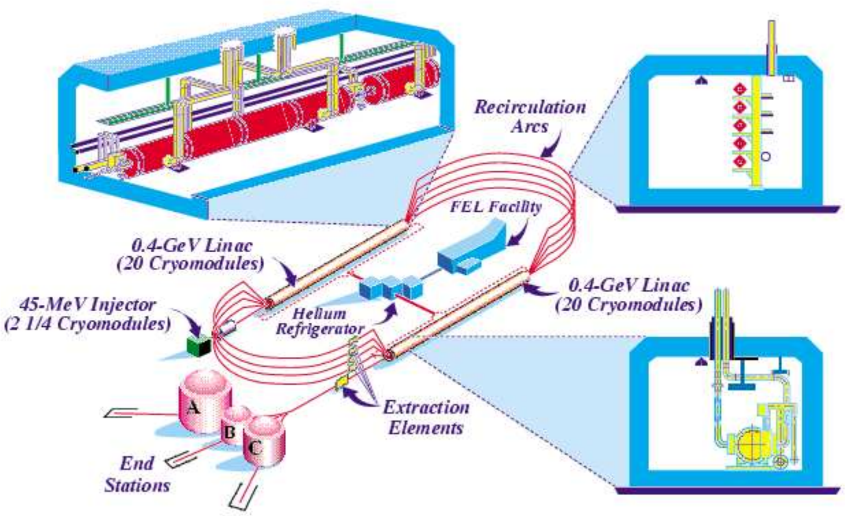

Figure 2.2: *The CEBAF accelerator side.*

The polarized electrons are produced by near bandgap photoemission from the GaAs cathode. The photoemission process is induced by a laser whose circular polarization is transformed into linear polarization for the emitted electrons. The electron polarization is flipped at a frequency of 1 Hz by inverting the laser polarization with a pseudo-random sequence.
The typical polarization obtained with this technique is approximately 70%.
The CEBAF accelerator can provide highly-polarized electron beam simultaneously to the three experimental halls. This is achieved by selecting the appropriate orientation of the polarization at the injector. During the recirculation of the electron beam, the spin orientation undergoes to a precession due to the interaction with the bending magnetic field. The total precession angle θ is function of the number of recirculating passes, of the linac energy and of the injector energy. The maximum polarization is obtained when the precession angle is a multiple of π. This condition can be achieved simultaneously in the three halls choosing a particular combination of the beam energies.
This procedure was used during the EG1 run in '98 since experiments requiring high beam polarization were in progress in Hall A and Hall C.
Since the choice of the beam energies that give pure longitudinal polarization is not always feasible, a fraction of transverse polarization can be present. This, however, does not affect the experiment results since the contribution of the transverse polarization are suppressed by a factor $1/\gamma$.
The beam polarization can be measured at the injector using a Mott polarimeter. In addition the polarization in Hall B is monitored by a Moeller polarimeter located upstream to the target position. The Moeller target consists of an iron foil that can be polarized either parallel or antiparallel to the beam direction by a Helmoltz-coil magnet. The two scattered electrons are detected in coincidence by 2 Pb-scintillating fiber detectors located symmetrically on the two sides of the beam line. Two sets of quadrupole magnets located downstream in respect to the Moeller target drive the scattered electron to the detectors.

The beam polarization delivered to Hall B during the '98 run was very stable, with an average value of approximately $\sim 70\%$ and a standard deviation of $\sim 2\%$.

2.4 The Torus System

CLAS is magnetic spectrometer based on six super-conducting coils arranged around the beam line to produce a field primarily in the ϕ-direction [53]. The choice of this configuration has been driven by the necessity of satisfying precise requirements determined by the physics program:

- homogeneous coverage of a large angular and momentum range for charged and neutral particles;
- good momentum and angular resolution; due to the Lorentz boost, the average momentum increases with decreasing emission angle and the relative $\Delta p/p$ has to improve in the forward direction to maintain the absolute resolution constant;
- good particle identification;
- high luminosity and counting rate capability: typical luminosity is $\sim 10^{34}$ cm^{-2}s^{-1};
- low background from electromagnetic processes (Moller electron, e+e- pairs etc)
- symmetry around the beam axis;
- compatibility with the operation of a polarized target.

The toroidal setup in comparison with the more common solenoid and dipole configuration offers a field free region around the target and a magnetic field that is always transverse to the particle trajectory. The first characteristic allows the installation of a polarized target with no interference between the target and detector magnetic fields. In addition, since the ϕ-pattern of the event is preserved, the determination of ϕ is decoupled from the measurement of the polar angle θ and momentum p. A drawing of the torus system is shown in figure 2.3.
The six coils operate with a maximum current of $5 \cdot 10^6$ A and have been shaped to give the desired $\int B \cdot dl$ and therefore the requested resolution as a function of theta. The coil-operating temperature of 4.5 K is maintained by a forced flow of supercritical liquid helium supplied by the CHL (Central Helium Liquefier).
The absence of strong field close the beam axis helps in limiting the electromagnetic background since forward-going charge particles (e+e- pairs) are not deflected, while low momentum particles emitted at large angle (Moller electron) can be easily screened by an addition magnetic field that in the operation with polarized target is represent by the longitudinal dipole field of the target magnet as described in section 3.3.2.

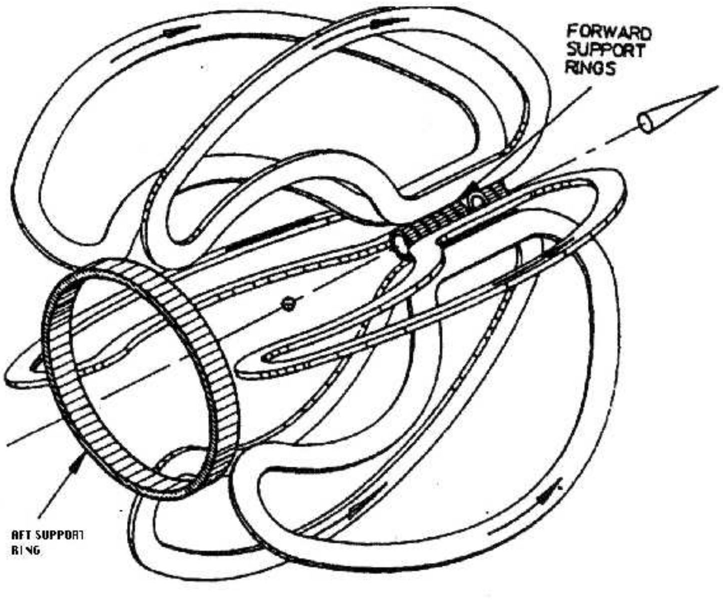

Figure 2.3: *Configuration of the torus coils.*

2.5 Drift Chambers

The measurement of the charged-particle momentum and trajectory is accomplished by a drift chamber system [54, 55]. The principle of operation of a drift chamber is the collection of the electrons produced through ionization of a gas by a charged particle that crosses it. The gas is maintained in an electric field so that the electron and ion created by ionization drift in opposite directions and are collected by the anode and cathode. While drifting, the electron can produce secondary ionization resulting in a multiplication and therefore amplification process. The detection of the corresponding electric signal gives information on the hit position of the original charged particle.
The CLAS tracking system consists of eighteen multi-wire drift chambers subdivided in three regions in each of the six sectors. Region 1 is a low magnetic field region located in the free space left inside the toroidal magnet, region 2 is a high magnetic field region placed within the large toroid while region 3 is located beyond the outer coil of the magnet. The wires are strung in the azimuthal direction and therefore perpendicular to the bend plane of the particle trajectories. The track position along these wires is measured by the 'stereo' wires that are canted by 6.5 deg in respect to the previous ones called 'normal' wires. Each chamber is wedge-shaped and is subdivided in two separate superlayers, one normal and one stereo. Each superlayer consist of six layers of sense wires surrounded by normal wires in an hexagonal arrangement as shown in figure 2.4. Guard wires are located at the borders of each superlayer and their potential is adjusted to simulate the electric field configuration of an infinite grid of hexagonal cells.
This configuration has been chosen because it offers a good independence from the entrance angle and is therefore well suited for this application since tracks are entering from widely varying angles. This design leads to maximum drift distances of 0.7 cm, 1 cm, 2 cm respectively in the three regions.

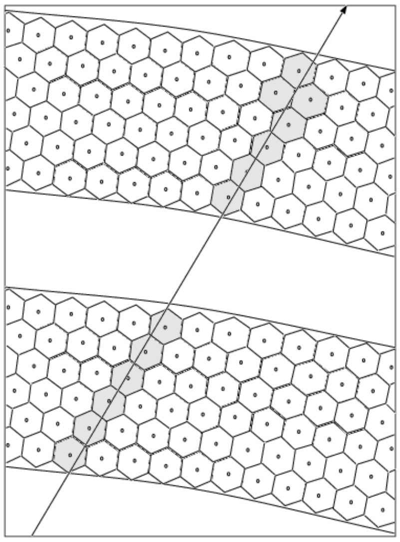

Figure 2.4: *Schematic of a section of drift chambers showing the two superlayers each consisting of 6 hexagonal-cells layers. The cells are electrostatic boundaries determined by field wires located at each corner of the hexagon. The guards wires (not shown) surround each superlayer. A charged particle is shown crossing the drift chambers, with the shadowed area indicating the hit cells.*

The gas used is 90% − 10% mixture of Argon and CO_2. The Argon provides a gain of $\sim 10^4$ while CO_2 is necessary to avoid the occurrence of a cataclysmic ionization avalanche. The intrinsic resolution provided by this gas is $\sim 100\ \mu$m. The final space resolution achieved in operating condition is $\sim 500\ \mu$m, mostly limited by the knowledge of the geometry and time dependence of the calibration parameter. The resulting momentum resolution is $\sim 0.5\%$ for low momentum and 1.5% for high momentum tracks.
The use of small wire diameters and low wire tension makes possible the design of thin end plates that maximizes the solid angle coverage. The use of thin foil entrance windows minimizes multiple scattering. The total amount of material ranges between 0.1 and 0.4 radiation lengths. Circuit boards that provide pulse shaping and discrimination are mounted on the endplates, while the electronics that perform timing and readout for the data acquisition are in common electronics crates.

2.6 Cerenkov Counters

In electron scattering experiments the main source of background is represented by negative pions. For this reason CLAS is equipped with threshold Cerenkov counters that have the function of discriminating between electrons and pions [56].
Charged particles crossing a medium with velocity that is higher than the local phase velocity of light emit radiation known as Cerenkov light. The threshold at which this process occurs is given by $\beta = 1/n$ where n is the refraction index of the medium.
The gas adopted for the CLAS Cerenkov system is perfluorbutate C_4F_{10} which has a

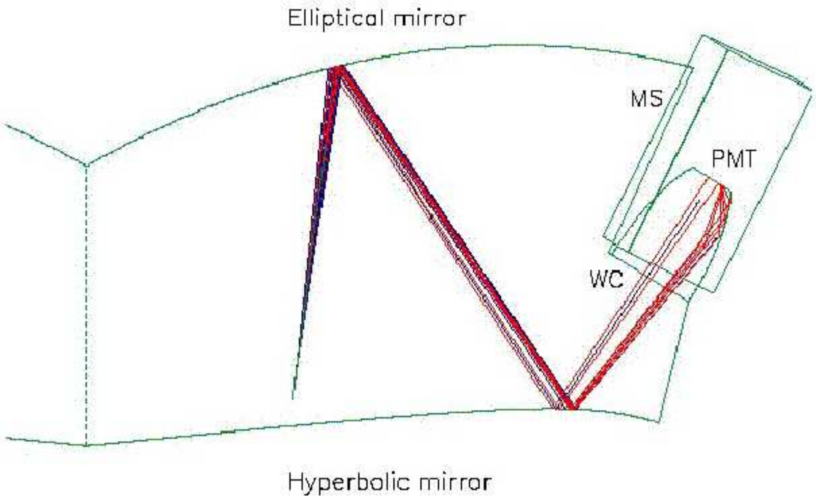

Figure 2.5: *Optical arrangement of one of the 219 modules of the CLAS Cerenkov detector showing the optical and light collection components. The PMTs lie in the ϕ region hidden by the torus coils.*

refraction index of 1.00153. This leads to a threshold for the particle energy of $E > \gamma m$, where $\gamma = 18.09$ and m is the mass of the particle. This results in a threshold for electron of approximately 9 MeV, in comparison to the pion threshold of ~ 2.5 GeV. Above this particle energy the electromagnetic calorimeters becomes the fundamental tool for electron identification. The Cerenkov light is collected by a system of mirrors and focused toward specially positioned photomultiplier tubes. Due to the symmetry of the CLAS toroidal magnet, the azimuthal angle of the scattered particles remains almost unchanged when going through the magnetic field. This allows the realization of a mirror system that focuses the light from particles with different azimuthal angles and fixed polar angle to a point near the coil. The focal area is equipped with an array of photomultipliers, placed in the shadow of the torus coils, with a sensitivity to single photoelectrons.
Monte Carlo simulation were used to study and identify the best geometrical configuration for the mirrors and the results is shown in figure 2.5. Simulation and measurements indicates that the average number of photoelectrons collected is about seven giving a theoretical minimum inefficiency of 1×10^{-3}.

2.7 The Electromagnetic Calorimeter

CLAS is equipped with 8 modules of electromagnetic calorimeter that serve three main functions:

- detection and trigger of electrons at energies above 0.5 GeV;
- detection of photons at energies above 0.2 GeV, allowing π^0 and η reconstruction from the measurements of their 2γ decays;

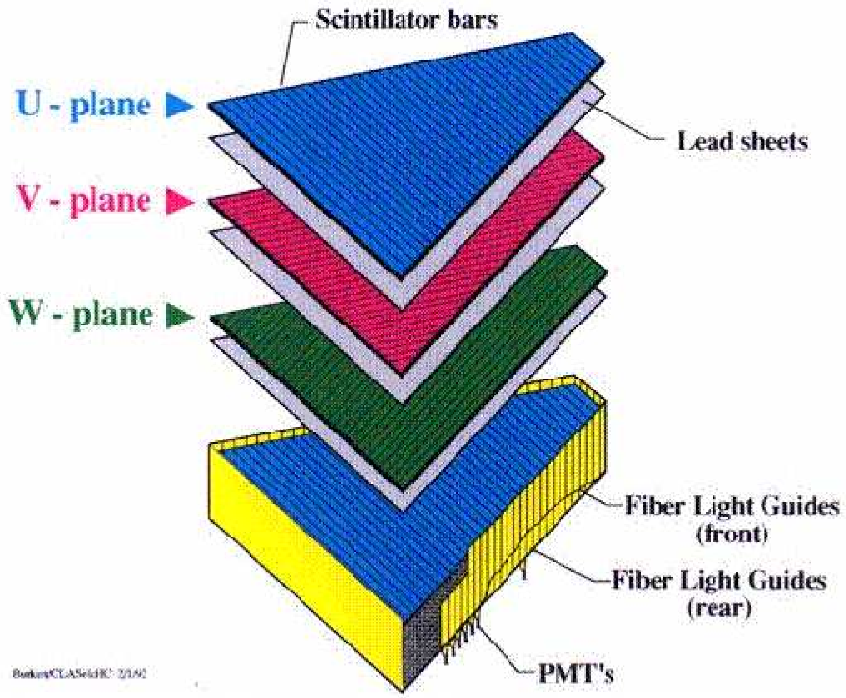

Figure 2.6: *Exploded view of one of the six CLAS electromagnetic calorimeter modules.*

- detection of neutrons, with discrimination between photon and neutrons using time-of-flight technique.

Six of the eight modules are located in each sector in the forward region, covering the polar angles from 10 to 45 degrees (forward angle calorimeter), while the remaining two modules are placed in sector 1 and 2 covering from 50 to 75 degrees (large angle calorimeter).

2.7.1 The Forward Angle Calorimeter

The forward detector consists of six sampling calorimeters made of alternating layers of scintillator strips and lead sheets with a total thickness of 16 radiation lengths [57]. A lead:scintillator thickness ratio of 0.2 was used, requiring 40 cm of scintillators and 8 cm of lead per module. With this configuration, approximately 1/3 of the energy of a shower is deposited in the scintillator.
The choice of readout granularity was a compromise between the cost of photo-multiplier tubes, size constraints and resolution requirements, leading to a cell size of 10 cm.
In order to match the hexagonal geometry of CLAS, the lead-scintillator sandwich has the shape of a equilateral triangle. The sandwich is made of 39 layers, each consisting of a 10 mm BC-412 scintillator followed by a 2.2 mm thick lead sheet. To minimize shower leakage and the dispersion in arrival times, a "projective" geometry, in which the area of each successive layer increases, was used.
Each scintillator layer is made of 36 strips parallel to one side of the triangle, with the

orientation of the strips rotated of 120 degrees in each successive layer. Thus there are three orientations or views each containing 13 layers which provide stereo information on the location of the energy deposition. Each view is further subdivided in an inner (5 layers) and outer (8 layers) stack, to provide longitudinal sampling of the shower for improved hadron identification.
A fiber-optic light readout system transmits the scintillator light to the PMTs. Their signal is sent to ADC and TDC boards that are then read by two FastBus crates. The forward calorimeter provides the main mean of discrimination between electrons and pions for momenta above 2 GeV. For this reason this detector is included in the electron trigger.
The detector performances in running condition have shown that the position resolution estimated is approximately $\sigma \sim 2.3$ cm. This was estimated comparing the position reconstructed from the analysis of the EC signal and the projection of the associated track on the calorimeter plane. The energy resolution for electrons shown by the data is $\sigma/E = 0.003 + 0.093/\sqrt{E}$ (the energy is expressed in GeV) with a sampling fraction, i.e. the fraction of the shower energy collected by the active part of the detector, of ~ 0.27. Neutrals hits in the EC are identified by the absence of a matched DC track. The neutral pion are identified requiring two neutral hits whose reconstructed energies combine to give the mass of a π^0. The data have shown a resolution of $\delta m/m \sim 0.11 - 0.14$ (see figure 4.16). Neutrons can be discriminated from photon thanks to the time resolution of the calorimeter. This has been evaluated to be 500-600 ps. The neutron detection efficiency has been estimated using the $p(e, e', \pi^+)n$ reaction in which the neutron can be reconstructed by missing mass. The data showed an efficiency that rises from zero at 0.4 GeV/c to a plateau of approximately 60% above 1.6 GeV/c, in agreement with the expectation based on nuclear interaction lengths and Monte Carlo simulations.
A more detailed description of the design, calibration and performances of this detector can be found in ref. [57].

2.7.2 The Large Angle Calorimeter

The two large angle modules of the electromagnetic calorimeter (LAC) of CLAS are similar to the forward detectors [58]. In this case the modules are made of the lead-scintillator sandwich with a rectangular shape. They consist of 33 layers, each composed by a 0.20 cm thick lead foil and NE110A plastic scintillator bars with average width of 10 cm and constant thickness of 1.5 cm. The module thickness corresponds to 12.9 radiation lengths and 1.0 absorption lengths. Teflon sheets with 0.2 mm thickness separate scintillators from lead while 0.2 mm thick Teflon strips between each pair of contiguous scintillators bars avoid optical crossover. Each layer is rotated by $90°$ to form a $40{\cdot}24$ matrix of $10{\cdot}10$ cm^2 cells. The bar width increases going from the inner side toward the outer to guarantee the tapering required by the CLAS geometry. The surface exposed to particle fluxes is $217{\cdot}400$ cm^2. The module is vertically divided into an inner and an outer part to improve electron/pion discrimination. Scintillators lying (for the inner and outer part separately) one on top of the other with the same orientation form 128 different stacks. The electromagnetic showers originate in the lead sheets and propagate through the layers: the energy absorbed in the active material produces a light pulse that is collected at both scintillator ends with a Lucite light guide coupled to scintil-

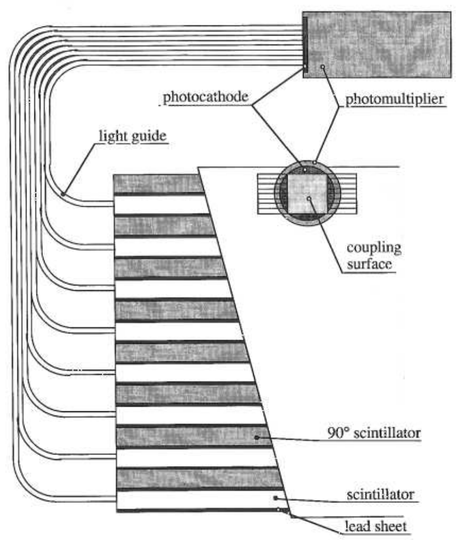

Figure 2.7: *Light collection system for the CLAS Large Angle Calorimeter. The light pulse is collected at both scintillator ends with a Lucite light guide coupled to the scintillators. The collected light is summed for each stack separately before being transmitted to the PMTs.*

lators with an air gap an a 7.0·0.4 cm^2 area. The collected light is summed for each stack separately before a EMI 9945A photomultiplier. Therefore the light pulses emitted from 8 different scintillators are summed up on a single photomultiplier that is placed on the top surface of the LAC module several centimeters away from the scintillators (see figure 2.7). To reduce photocathode-non-homogeneity effects, the light guides are glued together before coupling to photomultiplier. Scintillators placed in the inner and the outer parts are coupled to different photomultipliers. Monte Carlo simulations showed that the LAC performances are strongly affected by the efficiency of light transmission and collection. For this reason, special attention was devoted to the production of high quality scintillators and light guides. In particular, scintillators with a light attenuation length longer than 300 cm and light guides that provide about 5 photoelectrons/MeV when coupled to a EMI 9945A PMT were selected.

2.8 The Time of Flight System

CLAS is equipped with a system of scintillation counters whose purpose is to determine the time of flight for the charged particles and, in conjunction with the tracking system, the particle identification [59]. This detector was designed to ensure a good time resolution ($\sigma \sim 150$ ps) in particular at low polar angles since a large percentage of the scattered particles are emitted in forward direction. This resolution is necessary to be able to discriminate pion and kaons with momenta up to 2 GeV/c. In addition the system was studied in order to match the typical rates expected for CLAS that with a luminosity of 10^{34} $cm^{-2}s^{-1}$ can go up to 100kHz in the forward direction.
The time of flight system consists of scintillator strips (BC-408) that are located perpen-

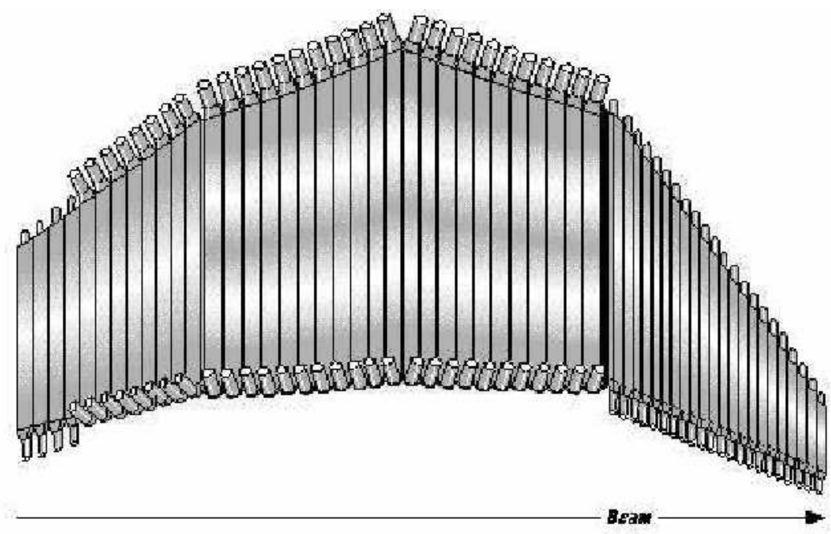

Figure 2.8: *Scintillator strips of the Time of Flight system of the CLAS detector.*

dicularly to the beam direction with an angular coverage of 2° each. The scintillators are located between the Cerenkov counters and the electromagnetic calorimeters. Each sector contains 48 strips with a uniform thickness of 5.08 cm. The width of the scintillators varies from 15 cm for the very forward angles to 22 for the large angles while the lengths are between 30 and 450 cm.
With this design a coverage in the six sector from 8 to 142 degrees was achieved corresponding to a total area of the scintillator system of 206 m^2.
Each scintillator strip is read by to photomultipliers that are located between the nearby sectors, in the shadow of the torus coils. The light is transmitted to the PMTs by light guides.
For each photomultiplier both the time and pulse height are measured. This allows the evaluation of the time-walk correction. In addition the measure of the pulse height allows the reconstruction of the energy released by the crossing particle, providing additional information for the particle identification. In relation to this feature, it's important to notice that for particle momenta below 500 MeV/c the energy resolution that characterizes the time of flight system is better than the resolution of the tracking system that for these low momenta is limited by multiple scattering.
Calibration with cosmic rays showed an intrinsic time resolution that varies from 80 ps for the forward angle up to 160 ps for the large angle strips. Real data were also used to study the time resolution of this system and, by comparing the interaction time reconstructed from the electron time of flight traced back to the vertex with the accelerator RF time, a resolution of ~ 160 ps was found.
This resolution is sufficient to separate, as requested, pion from kaons up to 2 GeV/c. The time of flight signal can also be used to define the trigger: this possibility is exploited in photon runs to define hadron triggers.

Detector	**Threshold (mV)**	**Threshold (GeV)**
EC	150 mV	600 MeV
CC	38 mV	*< 1 photo electron*

Table 2.1: *Trigger thresholds for the Cerenkov Counter and the Electromagnetic Calorimeter*

2.9 Data Acquisition System and Event Trigger

The signals seen by the different detectors are recorded by the data acquisition when the event satisfies the chosen trigger condition. In electron scattering experiment with CLAS, the trigger is given by the detection of an electron in the final state. This condition is defined by a simultaneous hit in the Cerenkov counter and in the Electromagnetic calorimeter above a selected threshold. The thresholds used in the present case are reported in table 2.1. This loose condition allows the simultaneous measure of both inclusive and exclusive channels in a large W and Q^2 range. The Cerenkov threshold was below the single photoelectron peak in the PMTs to avoid the introduction of a bias. The EC threshold was chosen to maximize the accessible W range while maintaining a good electron versus pion selectivity. With this configuration approximately 60% of the recorded events contains an electron. The remaining 40% consists of events in which the trigger is due to noise in the Cerenkov Counters or to hadrons, that interacting with the detector structure, produce showers. These events are easily rejected in the event reconstruction process.
A schematic of the Data Acquisition system is given in figure 2.9. The system was developed by the CODA group at Jefferson Lab and by the DAQ group of CLAS.
After passing the pre-trigger discriminators, the signals from the different detectors are sent to the Level-1 trigger that contains the final configuration of the Event Trigger. When these requirements are satisfied the data are sent to the Trigger Supervisor, which communicates with 17 FASTBUS crates. The data are therefore read out, converted to digital information and transferred through the ROC memory and the network to the Event Builder. The Event Recorder finally receives the information from Event Builder through the main Data Distribution shared memory. The data are written to a local disk to be later transferred to a tape silo for massive storage.
During the EG1 experiment, the typical performances of the DAQ system were characterized by a rate of $\sim 2. - 2.5$ kHz and a live time of 85-90% for a luminosity of $0.5 \cdot 10^{34} cm^{-2} s^{-1}$.
An online monitoring system is used to have continuous control on the status of the detector components and of the acquisition system. For this purpose events from the main Data Distribution system are transferred to a satellite computer where monitoring programs run during the data taking.

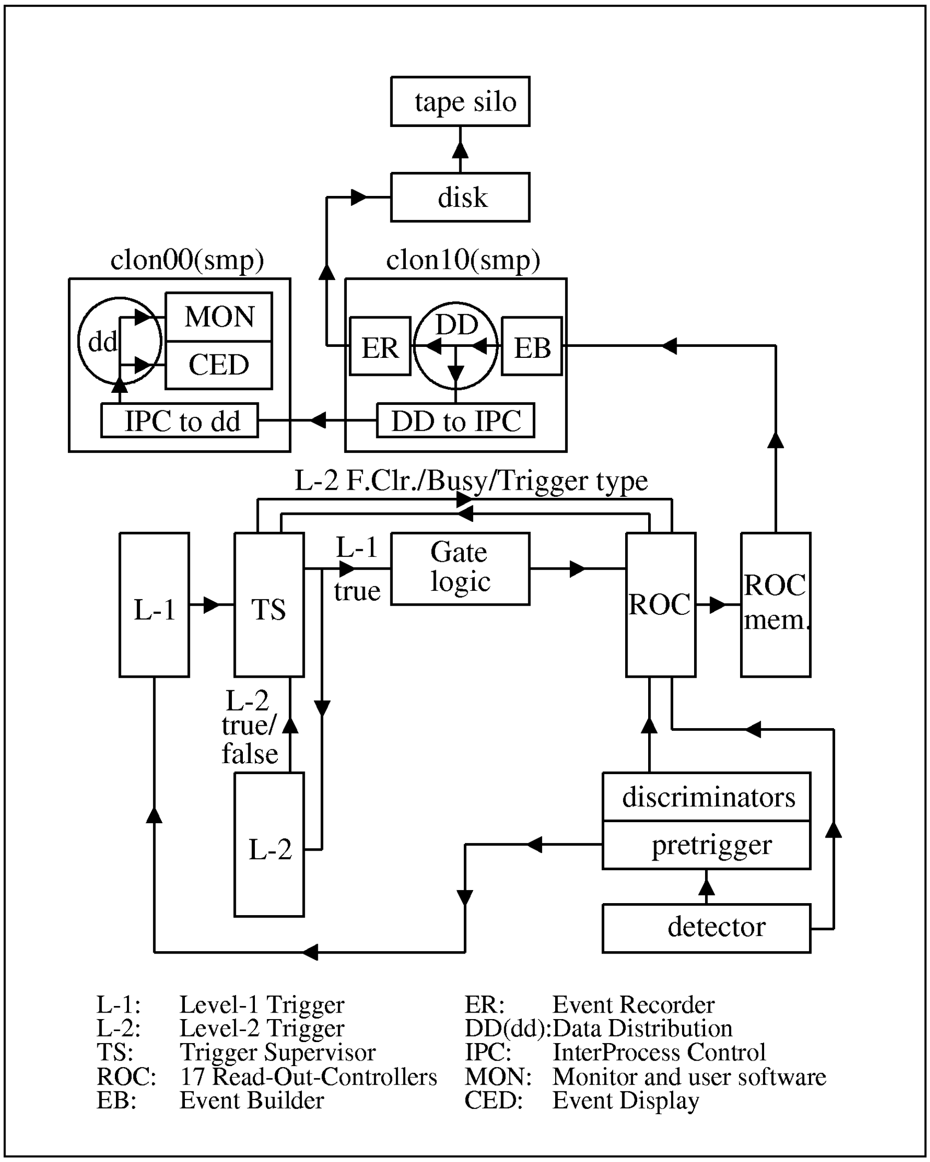

Figure 2.9: *Schematic diagram of the DAQ Acquisition system (diagram courtesy of Kostantin Loukachine).*

Chapter 3

The Polarized Target

3.1 Introduction

The knowledge and technology for the realization of polarized targets to be used in scattering experiments has been developed in the last 30 years and the research in this field is still in progress.
Several experiments that used polarized target like SMC [48], E143, E155 [47] have been concluded and their results are available. At present new experiments are in progress at Mainz, Hermes and Jefferson Lab while others are planned at GRAAL and Spring 8.
In spite of the experience that has been accumulated in these years, the technical aspects of measurements that exploit polarization degrees of freedom always need to be planned and studied very accurately to overcome the complexity of the polarized target operations. The choice of the target type and design need also dedicated studies considering the constraints represented by the running condition, the detector geometry and the beam characteristics.
In the present case the main constraint is given by the layout of the CLAS detector: its particular geometry increases the complexity of target operation limiting the available clearance.
In this chapter I will describe the characteristics of the polarized target that was designed and built for the EG1 experiment.
I will first introduce the existing techniques in the realization of polarized nuclear targets and I will explain the reasons of the choice that was made for the Hall B target. I will then describe the design that was chosen, including the description of the target cryostat, the refrigerator system, the target system, and how these have been built to match the characteristics of the CLAS detector. Finally I will briefly summarized the performances of the polarized target during the EG1 run.

3.2 Polarization Techniques

Most of the techniques used to polarize a system of nuclei or nucleons are based on the interaction of their magnetic moments with an external magnetic field and on a low temperature environment. The interaction with the magnetic field leads in fact to a splitting by Zeeman effect of the energy levels of the system that corresponds to different orienta-

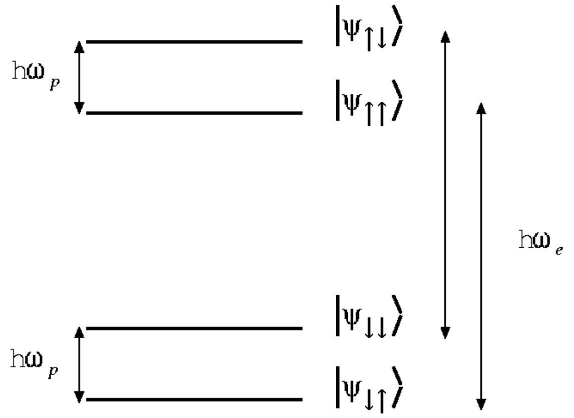

Figure 3.1: *Scheme of the energy levels of a two spin 1/2 particle with opposite charges, interacting with an external field. The system is characterized by four eigenstates as shown in the picture. If the two spin 1/2 object interacts, the hamiltonian describing the system will include a perturbation term, and the eigenstates will be given by linear combination of the 'free' hamiltonian eigenstates.*

tion of the target spin relative to the direction of the external field. The low temperature reduces the thermal motion in the system, allowing the control of the spin direction.
A polarization technique deals therefore with the control of the population of the energy levels: modifying these populations it is possible to change and also to reverse the polarization value, while changing the direction of the magnetic field it is possible to change the polarization direction.
Several different techniques have been developed and are presently used. The choice of the technique depends on several factors as:

- the beam type (photons, muons, electrons, ...) and intensity (accumulated or extracted beam);
- the available clearance and the interference with the detecting system;
- the radiation level that will affect the target.

These factors determine the type of target (solid or gas), the maximum magnetic field intensity, the operating temperature and the type of material. For example a limited clearance for the target can influence the choice of the refrigerator system and limits the dimension of the target magnet and therefore the field intensity. The maximum field is also determined by the interference with the detector whose operation can be deeply affected by the target field. In addition, the necessity of reaching high luminosity limits the use of gas target only to the cases of high beam currents as for accumulated beams, while extracted beams, whose current is of the order of few tens or hundreds of nanoAmps, require solid targets.
Since in Hall B the beam current is of the order of few nanoAmps, in the following I will discuss only the case of solid targets and the materials used for these applications.

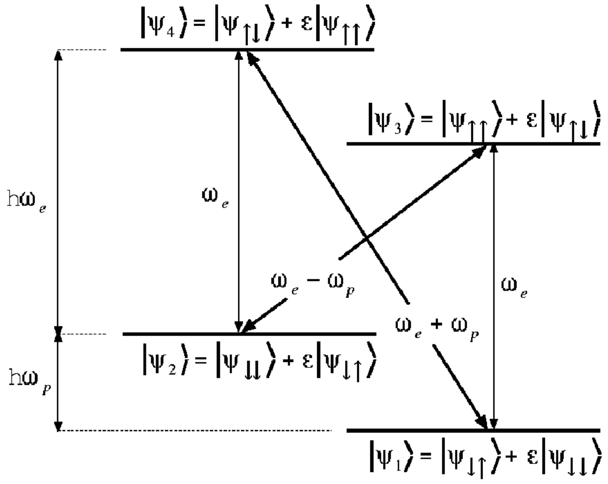

Figure 3.2: *Schematic of the allowed two-spin transition in a system characterized by spin-spin interaction. Due to the mixture of the system eigenstates introduced by the spin-spin interaction, transition in which both particles change their states are possible. The probability of these transitions is small in comparison to the single-spin transition since is connected to the parameter ϵ that describes the pure-states mixture. These processes are anyhow the basis for the dynamic transfer of polarization*

3.2.1 Polarization Techniques for Solid Target

The main means to get significant polarization for solid target are, as mentioned above, high magnetic field and low temperature. In fact, a system of polarizable particles in these conditions gains a natural polarization known as thermal equilibrium polarization. For example spin 1/2 particles as protons with a magnetic moment μ, located in a magnetic field B at a temperature T, and in the the absence of any additional interaction have a polarization $P = tanh(\mu B/KT)$. In the case of atomic polarization, where the typical magnetic moment is represented by the electron Bhor magneton, a magnetic field of 1 Tesla and a temperature of 1 K is sufficient to reach a polarization of 95%. On the contrary for nuclear system, for example protons whose magnetic moment is 2000 smaller, the same condition gives a polarization of 0.1%. In this case is therefore necessary to exploit additional methods.
The simplest technique, known as 'brute force' [60], is based on an extremely high magnetic field and a very low temperature. The basic idea is in fact to maintain the thermal equilibrium condition and to maximize the factor B/T. The maximum factor ever reached is 1700 Tesla$\cdot$K^{-1} corresponding to a magnetic field of 17 Tesla and a temperature of 10 mK [60]. In the case of proton this condition would give a polarization of 94%.
In spite of its simplicity, this technique is hardly usable in standard scattering experiments. The strong magnetic field would in fact disturb the detector operation while the very low temperature that is required is achievable only for weakly interacting beams like photon beams and with expensive and complex refrigerator systems. A more complex but very successful technique is the so called Dynamic Nuclear Polarization or DNP [60, 61]. This method has been developed for solid target and can be applied to particular

materials that contain paramagnetic centers[1], in addition to the particles that need be polarized. In this case a high polarization can be easily achieved for these paramagnetic centers (for example free electrons) by keeping the material in a magnetic field and at low temperature with a B/T ratio of the order of 5 (5 Tesla and 1 K, or 2.5 Tesla and 0.5 K) that is sufficient to give an atomic polarization of the order of 99 %. This high polarization is then transferred to the nuclear system (for example protons) using a radiofrequency field with a appropriate frequency. If the 'free electrons' are in adequate concentration and uniformly distributed in the material, a spin-spin interaction between these objects and the protons can be present. In this case the energy levels of the system, corresponding to different orientation of the two spins (see figure 3.1) relatively to the external magnetic field, are mixed together. Thanks to this mixing an electromagnetic perturbation with a frequency equal to the sum or difference of the Larmor frequencies of the two interacting systems can induce transitions in which both spins are flipped (see figure 3.2). In this way is possible to create a 'dynamic' transfer of polarization from the electrons to the protons. After the double spin transition, the electron will quickly decay to its fundamental state with a relaxation process based on the interaction with the lattice and will be used for a second transfer. The proton on the contrary will remain in the new state since its interaction with the lattice is limited by the small magnetic moments. Typical relaxation times are in fact of the order of 1 ms for the electrons and of the order of hours for the proton [61]. The transferred polarization can then be spread from the protons surrounding the free electrons to the rest of the material by spin-spin interaction.

This technique leads to typical polarization for proton of 80-90% and has also been used for deuterons with polarization of 30-40%.

The required conditions are less extreme and therefore more compatible with the typical constraints of a scattering experiment. In particular temperature of the order of 1 K can be maintained with electron-beam currents up to one hundreds nanoAmps with Helium-4 evaporation refrigerators or dilution refrigerators.

On the contrary the choice of the material is more problematic. The chosen compounds are intrinsically not 'clean' (NH_3, butanol, propandiol, LiH and the corresponding deuterated molecules). This is necessary because most of the clean samples including the obvious H_2 and D_2 are not polarizeable at low temperature due to the conversion to para-state.

In addition the technique requires the presence of the free radicals, that have been inserted succesfully by chemical doping or irradiation only for particular materials (further information about the materials used with DNP can be found in ref. [62, 63, 64, 65, 66, 67]).

A third method that has been used successfully is the frozen spin technique [60]. In this case after reaching high polarization for example with DNP, the nuclear spins are 'frozen' by lowering the temperature to few milliKelvin. In these conditions, the relaxation time for the system becomes longer, reaching values of few days. The radiofrequency source can then be turned off and the magnetic field intensity lowered, ending up with a target than can be used for days, without the additional complexity of high intensity magnetic field and radiofrequency generator. One disadvantage of this method is that the very low temperature can be maintained only with photon beams that release small amounts of

[1] Paramagnetic centers are atomic systems, as free electrons, lattice vacancies or free radicals, that can be polarized.

energy in the target. Furthermore the polarization is maintained by holding coils usually designed to surround completely the target, so that the scattered particles have to cross the magnet structure.

3.3 The Polarized Target for CLAS

The CLAS polarized target has been built in collaboration between Jefferson Lab, the INFN of Genova, and the University of Virginia.
The main goal in the design was to match the characteristics of the detector and to satisfy the constraints created by the electron beam. In particular, the dominant limitations are given by:

- the limited space available for the target structure: this has in fact to fit inside the first drift chamber region of the CLAS detector;
- the local heating produced by the electron beam;
- the radiation damage that may affect the target material;
- the multiple scattering and energy loss inside the target material and the target cryostat;
- the requirement of large scattering windows for the outgoing particles.

Considering these requirements the natural choice was a standard $^{15}NH_3/^{15}ND_3$ target polarized via DNP. A superconducting magnet provides the magnetic field (5 Tesla) and a Helium-4 refrigerator system maintains the material at a temperature of 1 K.
In the following I will describe the different part of the target system, including the target material, the target cryostat with the superconducting magnet, the refrigerator, the radiofrequency system, the NMR used for the polarization measurement and the target insert, showing how the different parts have been constructed to satisfy the mentioned requirements.

3.3.1 The Target Material

The ammonia target was chosen because of its very good resistance to radiation damage. Ammonia can stand an accumulated dose of $10^{15} - 10^{16}$ electrons/cm^2 before showing a significant decrease in the polarization. In addition the initial performances can be restored with an annealing process [2] [65, 66]. For the same reason materials like butanol are excluded for electron beam experiments: the paramagnetic centers, introduced by chemical doping, are destroyed by the irradiation and cannot be restored.
The ratio between free and bound nucleons (3/18), called dilution factor, is one of the higher for hydrogenated samples (butanol has a factor of 9/74 and ^{7}LiH has 1/7).

[2] The annealing process consists in heating the damaged material to a temperature of 70-80 K. This procedure has been shown to reestablish the initial performances of a damaged target. The reason is that, additional paramagnetic centers that are created in running condition (on-beam cold irradiation) and that tend to disturb the DNP process are destroyed in the heating process.

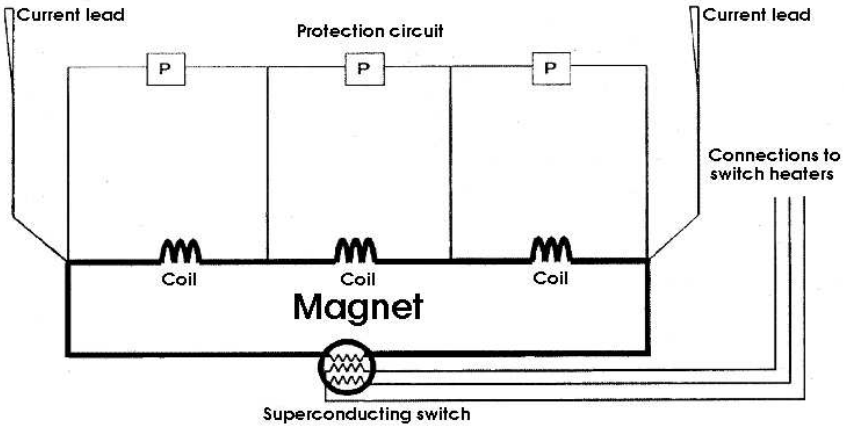

Figure 3.3: *Electric circuit of the 5 Tesla magnet. The schematic shows the superconductive switch, used to change the magnet operation to persistent mode, and the protection circuit.*

The only disadvantage is represented by the presence of polarizeable nuclei. The nitrogen, in fact, during the dynamic polarization of the hydrogen nuclei gains a small degree of polarization following with good approximation the EST prediction (see ref. [68]). The positive aspect in using ^{15}N is that the nucleus polarization is completely carried by the unpaired proton and its effect can be corrected.

3.3.2 The Superconducting Magnet and the Target Cryostat

The superconducting magnet that provides the 5 tesla field has been built by Oxford Instruments. The magnet and target cryostat were designed on the basis of the SLAC polarized target [63]. It consist of a number of coaxial solenoid sections in dipole configuration wound using multifilamentary superconducting wire. This technique limits the flux jumping, i.e. the movement of the flux tube inside the superconducting material that induces heating. The magnet material is a Niobium-Titanium alloy whose critical temperature is ~ 9 K.
The magnet can be operated in persistent mode using the superconducting switch (see figure 3.3) [3]. In this type of operation, the superconducting circuit is close to form a continuous loop, and the power supply can be switched off leaving the magnet 'at field'. In this situation the energy dissipation, that in a superconducting system is mainly due to the current flowing in the magnet leads, is absent. In persistent mode the field decays only very slowly. The rate usually depends on the inductance, the design and the number of superconducting joints and the choice of conductor. In the present case the current decay rate is 1 part in 10^6 per hour.

[3] A superconducting switch consists of a piece of superconducting material that is located in the magnet circuit to form a parallel with the magnet itself. During the energization of the magnet the switch is warmed up by a heather to hold it open. In this state, the resistance of the switch, even if only of a few Ohms, is so much higher than that of the magnet that almost all the current flows trough the magnet. When the energization is complete the heather can be turned off. When the power supply is ramped down and the current in the magnet leads is reduced, the current flowing trough the switch gradually rises until it carries the full current of the magnet.

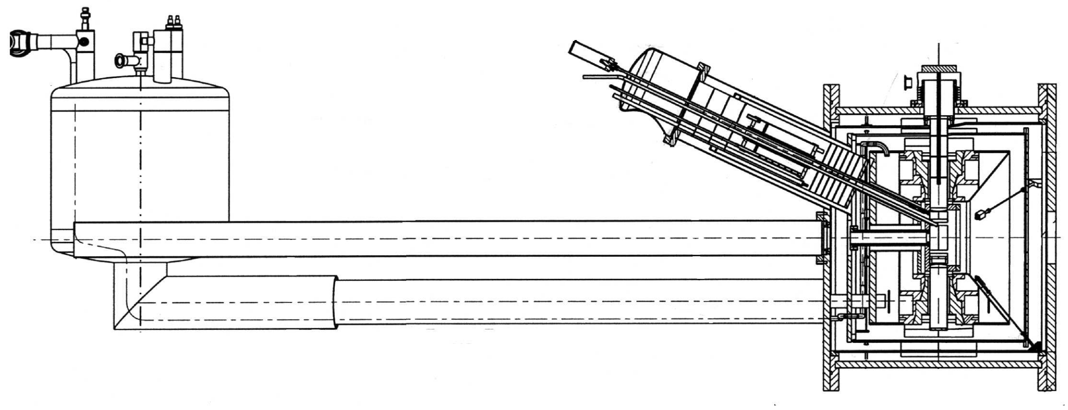

Figure 3.4: *Schematic of the target cryostat. The superconducting magnet is enclosed in the dewar located at the right end and is cooled down by the helium supplied from the reservoir located at the other end of the cryostat. The two dewars are connected by a permanent tube.*

Protection resistors and diodes are provided for all the magnet sections (see figure 3.3). They are mounted in the same helium reservoir as the magnet. Diodes are used in the protection circuit to ensure that all the current flows through the magnet under normal operation so that the energization current is proportional to the magnetic field. They also reduce the heat load from ohmic heating in the protection resistors and hence the system boil off while the magnet is sweeping. If the magnet quenches, the barrier voltage of the diodes is exceeded and the protection comes into operation automatically.
The magnet axis is parallel to the electron beam direction: as a result this is also the direction of the target polarization. This configuration is extremely favorable to this application. First of all the magnetic field at the axis is completely longitudinal and, consequentely, it does not interfere with the incoming electrons. In addition the target region that corresponds to dipole center is characterized by a very uniform field (see table 3.1); this is a fundamental factor for the proper functioning of the DNP process and also for the NMR measurement of the target polarization [4]. Finally the dipole configuration has shown a very good capability of shielding the drift chambers from Moeller electrons: these low energy particles are in fact deflected by the magnetic field and focused toward the forward hole of the detector without hitting the wire chambers.
The effect of the field on the scattered particles is to bend them in the azimuthal direction while the polar angle remains almost unchanged. The target field decreases very rapidly ($1/r^3$) in the radial direction, so that it becomes almost negligible inside the drift chamber volume. Nevertheless the target magnetic field is taken into account in the particle reconstruction as explained in chapter 4.
The magnet is enclose into a cryostat that is connected to a buffer dewar by a permanent connecting tube (see figure 3.4). The system is cooled down using liquid helium at 4.2 K: at this temperature the magnet can be energized. The helium is supplied to the buffer dewar from a 500 litres dewar that is filled directly from the CEBAF cryogenic system. The helium can be transferred from the buffer dewar to the magnet chamber by

[4]As mentioned before the DNP process is based on the irradiation of the target material with a radiofrequency field whose frequency has to match the magnetic field value. A uniform magnetic field is necessary to be able to polarize also extended samples with a fixed frequency.

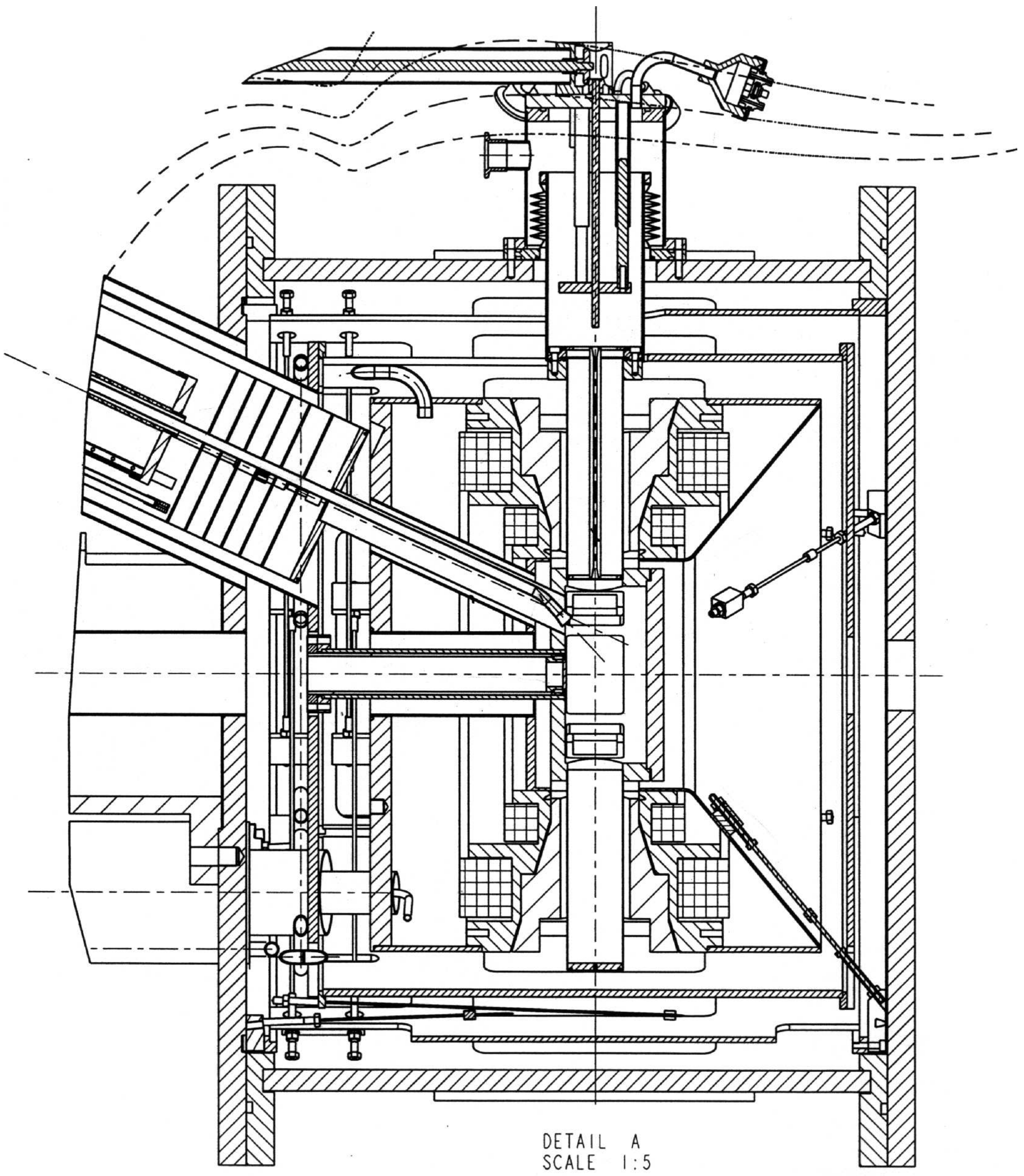

Figure 3.5: *Section of the target cryostat showing the magnet chamber. The magnet can was shaped to provide the necessary apertures for the outgoing particle both in the forward and side direction. The target chamber or 'banjo' is located in the central bore of the magnet and is accessible through the vertical tube. The helium is supplied to the 'banjo' by the refrigerator located at an angle of 30°. The horizontal tube is the final part of the beamline.*

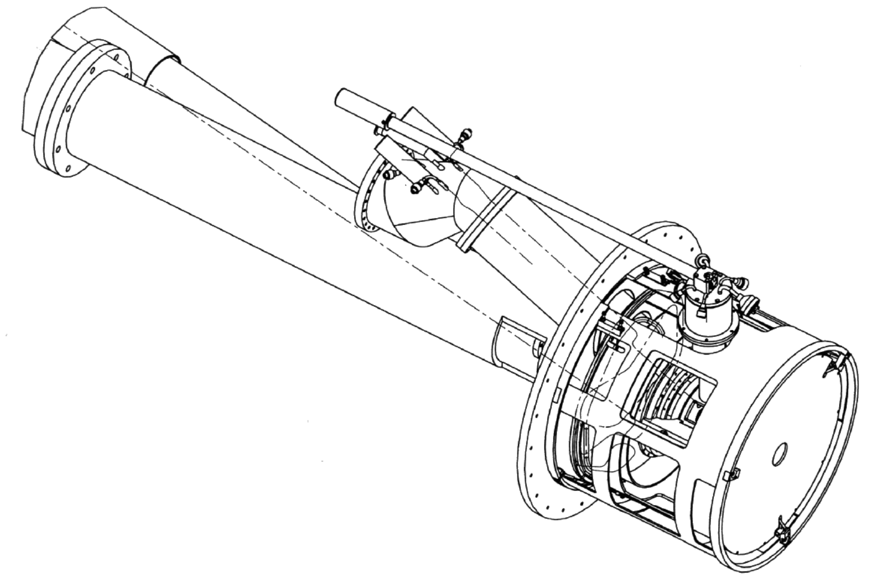

Figure 3.6: *Drawing of the target cryostat showing the apertures of the magnet can for the detection of the scattered particles. The apertures on the side match the CLAS sectors and have an opening polar angle from* $\pm 15^\circ$ *while in the front the radial aperture has an opening angle of* $\pm 50^\circ$*.*

overpressuring the former or simply by gravity. The helium evaporating from the magnet chamber flows first through a heat exchanger tube that cools the radiation shields surrounding the magnet and then along the connecting tube, and is finally recovered with the helium evaporating from the buffer dewar. The buffer dewar and the connecting tube are also partially cooled by cold gas. The liquid helium reservoirs are thermally insulated from ingress of heat by using

- low thermal conductivity materials,
- high vacuum chamber between the reservoirs and the room temperature,
- gas cooled radiation shielding and multi-layers superinsulation.

The all cryostat is vacuum insulated. The outer vacuum chamber (OVC) of the system is fitted with a large diameter pressure relief valve at the buffer dewar. This avoids a build up of dangerously high pressure in the OVC in the case of a cryogenic leak in the vacuum space.
The two-dewar design of the cryostat (magnet dewar and buffer dewar) has been chosen because of the limited space available in CLAS (see figures 3.4 and 3.9). In fact only the magnet dewar is located inside the detector while the buffer dewar is located upstream and holds the all structure.
The outer part of the cryostat at the magnet side has been equipped with large scattering windows both in the front and in the lateral direction. The windows matches the magnet apertures (see figure 3.6). The front window has an opening angle of $\pm 50^\circ$ while the six lateral windows (one for each sector of the CLAS detector) located at each side of the hexagonal case of the magnet enclosure have opening angles of $50^\circ \times 30^\circ$. This

Superconducting Magnet Characteristics	
Guaranteed maximum central magnetic field at 4.2 K	5.1 Tesla
Current for full field	123.646 A
Field/Current ratio	0.04125 Tesla/A
Homogeneity (over 20 mm diameter cylindrical volume)	1 part in 10^4
Magnet clear bore diameter	200 mm
Scatter angle	100°
Nominal inductance	61.7 henries

Table 3.1: *Characteristics of the 5 tesla superconducting magnet.*

windows have been manufactured at Jefferson Lab and consist of an aluminum alloy with a thickness of 275 μm for the axial window and 125 μm for the radial ones.

3.3.3 The Refrigerator System and the 1 K Chamber

The target material is located at the center of the magnet in a separate chamber. This is shown in figure 3.7 and is called 'banjo' because of the particular shape. This chamber is thermally insulated from the magnet being simply sustained from the top of the cryostat through a 5 in. stainless-steel tube and being surrounded by high vacuum. The tube gives access to the banjo for the sample insertion and is thermally sinked to the 75 K shield of the magnet to reduce the heat load. The circular part or banjo occupies the central bore of the magnet and has a diameter of 200 mm. Six windows are equally distributed on the side corresponding to the apertures of the magnet can to allow the exiting of the particles emitted from the target, located at the center. A 2 in. aluminum window (thickness 70 μm) is located on the back plane for the beam entrance, while a conical window closes the banjo from the front. The conical shape has been used to limit the distance between the entrance and exit windows to few millimeters more than the target length. The banjo is filled with liquid helium and cooled to 1 K by the refrigerator system. This consists of a vacuum insulated tube that connects the banjo to the pumping system. The fridge enters in the banjo at an angle of 30° because of the limited space left by CLAS in the vertical direction (see figure 3.9).
The refrigerator components are a separator pot, two series of heat exchangers located on the two sides of the separator, and two needle valves for the regulation of the helium flow. The separator pot is a copper cylinder with one inlet, two exits for the liquid helium regulated by the two valves and an exit for the vapor; its main function is to separate the liquid from the vapor phase. Liquid helium is supplied to the separator pot from the magnet buffer dewar with a vacuum-insulated and vapor-cooled transfer line. A rotary pump connected to the vapor exit of the separator pot maintains the flow. The separator pressure is below one atmosphere, approximately at 600 mbar, and the helium that enters is therefore pre-cooled to approximately 3.5 K. The liquid-vapor separation is performed by a sintered filter that allows the accumulation of the liquid phase at the bottom of the pot while the vapor are pumped out through the exit. The outgoing vapor

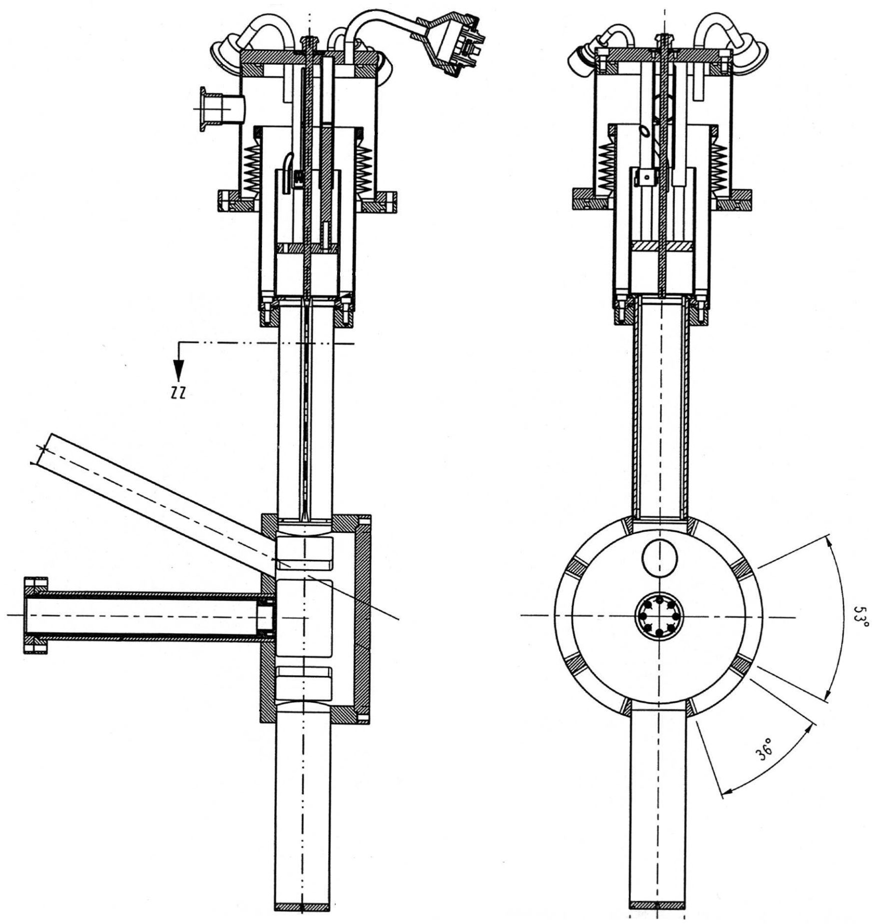

Figure 3.7: *Drawings of the target chamber or 'banjo'. The right drawing shows the front view. The position and angles of the side windows are indicated. As shown from the left drawing the beampipe enters in the banjo with a horizontal tube ending with a thin window (25 μm in thickness and 22. mm in diameter) to separate the pipeline vacuum from the cryostat vacuum. The vertical tube is the main access to the chamber and is use for the target insertion.*

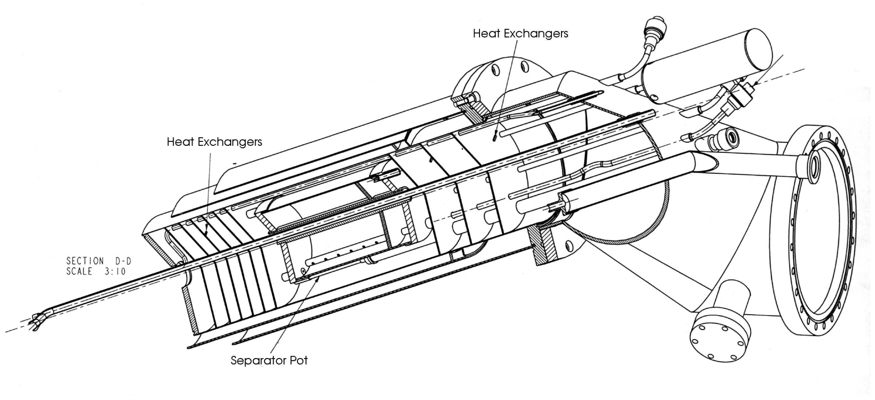

Figure 3.8: *Drawing of the refrigerator system.*

are used to cool down the upper heat exchangers (see figure 3.8).
The accumulated liquid can be used to cool down and fill the banjo volume. This operation can be performed opening the needle valves that regulate the flow of the two helium exits of the separator pot. In the initial part of the operation both valves are left open to guarantee the maximum flow. The main difference between the two valves called 'bypass' and 'run' is that the former regulates the flow through a straight tube that ends in the banjo while the latter regulates the flow through a spiral tube thermally sinked to the lower heat exchanger. The bypass valve is therefore more useful in the preliminary part of the procedure to cool down the banjo while in running condition it is kept closed and the liquid level in the banjo is maintained with the run valve. The liquid helium that flows through the run tube is in fact additionally cooled by the outgoing vapor.
A stable flow of liquid in the banjo is maintained by the pumping system that is directly connected to the refrigerator tube. The pumping system is made of two twins three-stage systems connected in parallel. The three stages consist of a mechanical pump Alcatel 2063H wiht pumping speed of 65 m^3/h, and two ruvacs pumps Alcatel RSV600 and RSV2000 with pumping speed of 600 m^3/h and 2000 m^3/h respectively. With this configuration the pressure in the banjo can be lowered to approximately 1 mbar corresponding to a temperature of $\sim$ 1.1-1.2 K.

3.3.4 The Microwave System

The microwave irradiation to enhance the target polarization is provided by a microwave generator (EIO-VKT2438P5, produced by CPI) located at the top of the refrigerator tube. It consists of a klystron in which electron emitted from a hot filament are accelerated toward a collector through a resonant cavity where radiation at a fixed frequency is emitted. The frequency can be changed modifying the dimension of the resonant cavity. The total allowed adjustment is $\pm 2\%$ around the central frequency that in the present case is 140 GHz, corresponding to the electron Larmor frequency for a 5 T field. The EIO generator is connected to a power supply that control the cathode, anode and collector voltages.
The microwave field produced by the generator is driven to the target material by a

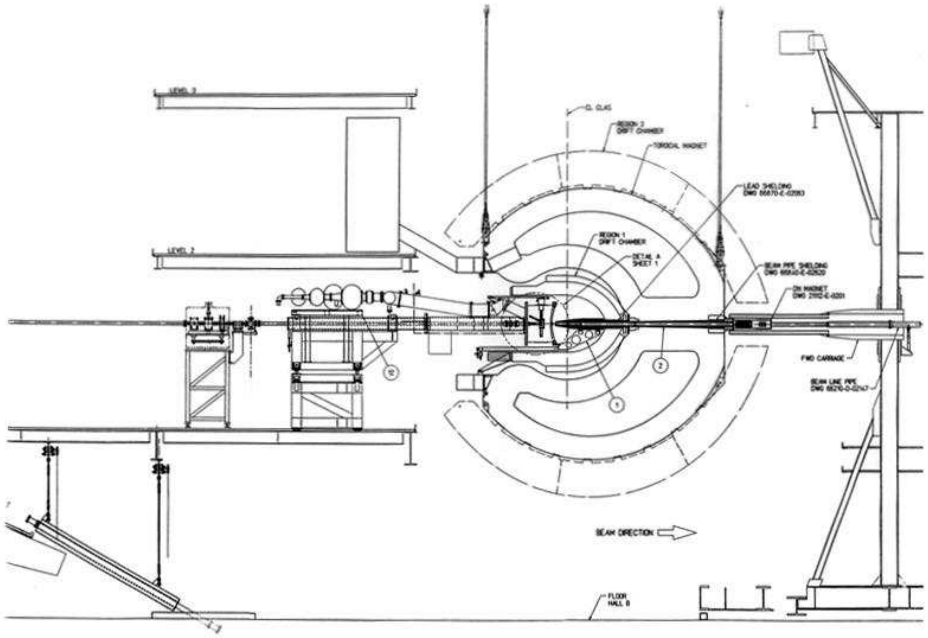

Figure 3.9: *Schematic of the polarized target when inserted in the CLAS detector.*

system of wave guides. The wave-guide line, composed both of rectangular and circular segments, reaches the banjo through the refrigerator tube that is equipped with a vacuum tight port for this purpose. The line ends with a trumpet for the irradiation of the target. This trumpet is located on the side of the target insert (see section 3.3.6) in order to allow the up and down movement of the insert.

3.3.5 The NMR System

The target polarization is monitored using a NMR system. It consists of a pick up coil, located close to the target material, that is inserted in a resonant circuit (a RCL series circuit). The presence of the material affects the value of the coil inductance and therefore the circuit impedance. In fact, if the RCL circuit is fed with a signal at the Larmor frequency of the polarized material, a magnetic resonance process is induced in the target with a corresponding absorption or emission of energy. This phenomenon affects the Q-curve of the circuit that plotted as a function of the frequency will show a peak at the target Larmor frequency. In our system the Q-curve is measured by a standard Q-meter produced by Ultra Physics Ltd..
The polarization is proportional to the area of the peak and its absolute value is obtained calibrating the system at a known polarization value. This is usually the thermal equilibrium condition (absence of microwave) where the polarization is given by the Curie law $P = \mu B/KT$. The peak area is extracted from the Q-curve by subtracting an 'unpolarized' Q-curve.
This method is traditionally used for solid polarized target and is fundamental during the

experiment since it provides an on-line monitor of the target polarization. Nevertheless in the present case, as will be shown in section 5.6, the polarization for the final analysis is extracted from elastic scattering. This approach has been found to be very accurate and reliable and does not suffer for the typical drawbacks of the NMR measurement, like non linearity of the system response (the NMR system is used from thermal equilibrium condition with typical polarization of 0.1-0.5% up to enhanced polarizations that for a proton target can reach 90-95%, spanning therefore more than 2 order of magnitude), systematic effects due to the peak extraction or non uniformity of the coil sensitivity (the NMR signal is mainly determined by the polarization of the material that is closer to the coil with a dependence as the sixth power of the distance).

3.3.6 The Target Insert

The target material is supported in the helium bath by an insert that can be introduced in the banjo from a port located at the top of the cryostat. A drawing of the target insert is shown in figure 3.10.

The insert, realized by the INFN of Genova, consists of an aluminum structure that holds 4 target cells. The cells (1 cm in length and 1.5 cm in diameter) are made of a plastic material (PCTFE) with a wall thickness of 0.2 mm to minimize the amount of material surrounding the target. This particular plastic compound was chosen because of its good resistance to the radiation damage, fundamental for an electron-scattering experiments, and for the absence of polarizeable molecules that would disturb the NMR measurement and would create a background for the experiment.

The aluminium structure is attached to a brass disk that is thermally grounded to the 75 K shield of the magnet to provide a low temperature point and therefore to minimize the heat load due to irradiation. A teflon segment is inserted between the brass disk and the aluminum support to ensure a good thermal insulation and a low heat conductivity along the all structure. The brass disk is then connected to the top flange by a threaded stainless-steel rod.

In operating condition three of the four target cells are filled with NH_3 and ND_3 for the physics measurement, with carbon (a 2.2 mm thick graphite disk) for background measurement and systematic checks, while the last cell is left empty. Each target cell can be located on the beam axis by moving the insert in the vertical direction. The movement is allowed by the threaded rod whose rotation, controlled remotely by a stepping motor, is converted in an up and down movement. With this design it has been possible to accomplish simultaneously measurement on proton and deuteron without a replacement of the target material that would require long times and complex operations.

Cryogenic coaxial cables connect the NMR coils, wrapped on the outside of the NH_3 and ND_3 cells, to the upper flange. Several temperature sensors, both thermocouples and resistors, are located on the insert to constantly monitor the material condition. A heather, placed between the NH_3 and ND_3 cells, is used for the annealing process.

Microwaves for the DNP process reach the target cell from the MW trumpet located on the side of the insert.

The target cells are closed on the back by a 25 μm aluminum window and on the front by a 50 μm kapton window that can be mounted on the cell after the filling with ammonia beads. For the cell windows, as well as for the all insert construction, a particular care was dedicated to the choice of non-magnetic and low-temperature resistant materials.

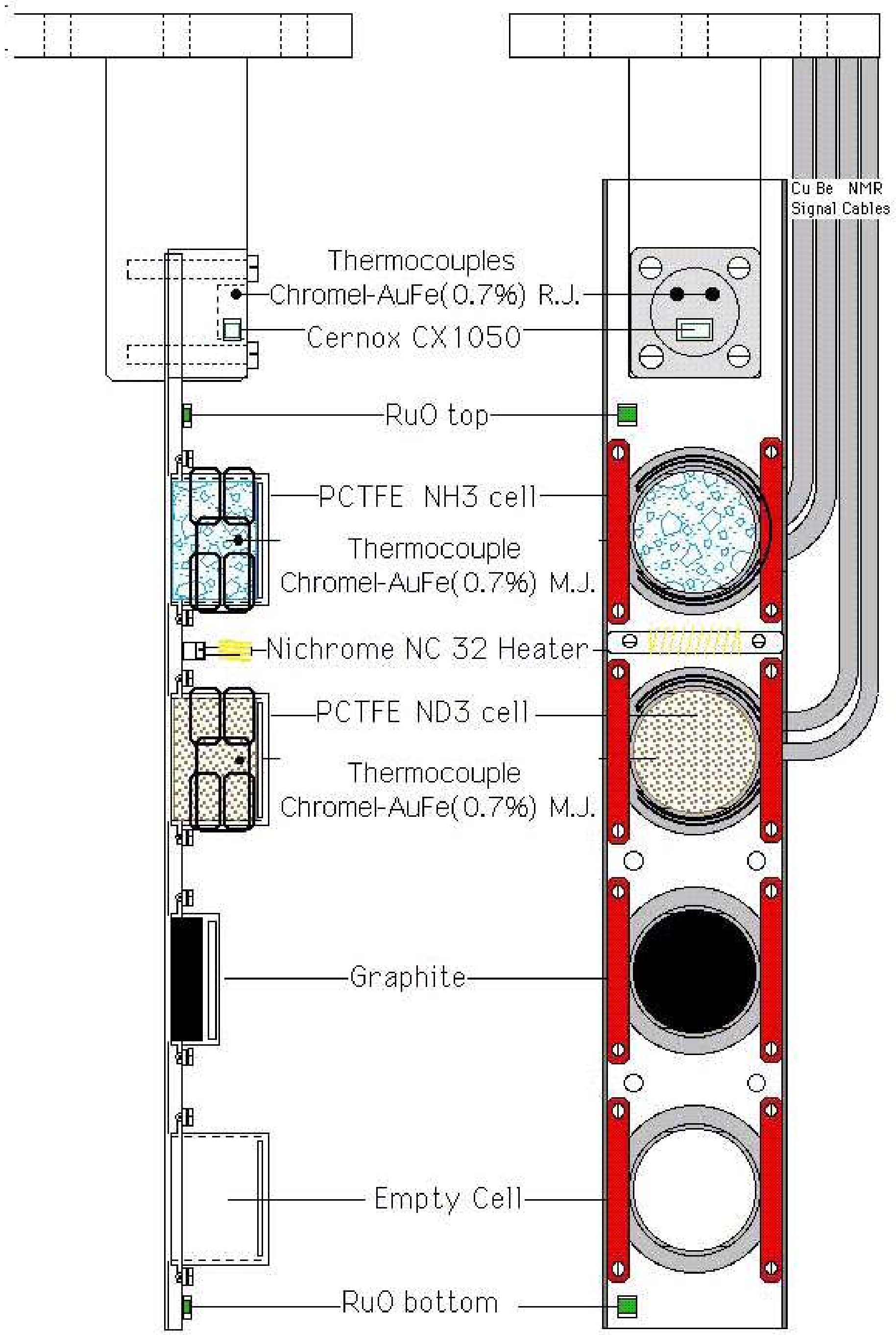

Figure 3.10: *Schematic of the target insert. The drawing shows the position of the four target cells. These are supported by the top flange through an aluminum structure.*

3.4 The Target Installation and Performances

The CLAS polarized target was used for the first time in '98 in a three months run for the first part of EG1. The target was installed in the inner part of the region 1 drift chambers supported by a horizontal tube attached to the pumping system cart (see figure 3.9). The target center was located approximately 60 cm upstream the CLAS center. This configuration allows the detection of the scattered electron down to very small angles and therefore improves the coverage at low Q^2. All the system including the magnet, the pumping system and helium supply, the microwave system, the NMR and the insert operation were controlled remotely. This was achieved using an Epics interface for the cryogenic part and a Labview-based system for the magnet, microwave, and NMR controls. The Labview code was developed in collboration between the JLAB electronic group, The University of Virginia, and the Genova section of the INFN.
The final temperature in presence of electron beam was $\sim$ 1.2 K and both the NH_3 and ND_3 target were used with typical polarizations of 70% and 20%. This values were limited by a loss of microwave power along the wave guides that was not possible to eliminate during the time of the experiment.
The overall performances of the system were stable maintaining a 75% efficiency in the operations similar to other CLAS experiments with cryogenic targets.
At present the target is employed in the second part of the EG1 experiment (EG2000) that will run till February 2001. The target has been tested in the mean time obtaining several improvements. In particular the lower temperature (1 K) and the improved microwave system (more than 1 W delivered to the target) has allowed to reach in this new run polarizations of 90% and 40% for the proton and deuteron targets.

Chapter 4

Event Reconstruction

4.1 Introduction

The CLAS event reconstruction code consists of several packages whose function is to analyze the information of the single detectors and combine them to obtain the complete determination of each physics event. Because of the complexity of the detector, the reconstruction process is subdivided into several steps. Initially the detector raw information (ADC and TDC values) is converted into the corresponding physical quantities (energy, time, etc.). All these information are then matched together to obtain the particles related variables (trajectory, time of flight, etc.). These quantities are finally analyzed to give the particle identification.

Both the input and output information of the reconstruction code are stored in BOS format. BOS is a fortran-77 based dynamic memory management system [70]. The information in the BOS files is subdivided into 'banks'. A bank is a collection of data words formed by a 'header' and a 'body'. The header provides the information on the number of columns and rows of the banks, the bank identifier and the location of the following bank. The body contains the real information. In the raw data files, each bank contains the information of a single detector or of a part of a detector. These banks are elaborated during the reconstruction process to give the physical quantities. For example, the raw time of flight bank, that contains the ADC and TDC values for each PMT, is transformed into the reconstructed bank that contains the energy and timing information for each signal. The final output of the reconstruction is represented by few high level data banks that contain the four-vectors for each particle in the physics events and all the relevant information that will be used in the physical analysis (live time, accumulated charge, etc.).

In this chapter I will describe the different steps of the event reconstruction. I will first describe the calibration procedure and the basic part of the reconstruction process, including the tracking and start time reconstruction. I will then discuss the particle identification for electrons and hadrons. Finally I will focus on the correction that are applied in the physics analysis and in particular in the selection of the reaction of interest for this thesis, i.e. the $ep \rightarrow e'\pi^+n$ channel.

4.2 Data Processing

4.2.1 Detector Calibration

The first part of the data processing is represented by the detector calibration. In this preliminary phase, a selected sample of data ($\sim$ 10% of the total) is processed to check the detector response. The data sample is chosen uniformly during the entire run period to verify the time stability. Both the energy and time calibration of each detector component are checked and the corresponding calibration constants are adjusted to give the correct behavior. This procedure is applied for each different run period to take into account the different running conditions, the hardware modification that may have occurred and the drift of the detectors response over time. The obtained results are checked monitoring the significant variables.
When the reconstruction has reached to the desired level of accuracy the calibration constants are 'frozen' and the final data processing is performed.

4.2.2 Final Reconstruction Process

After the completion of the detector calibration, the full data processing is performed. The time required for the reconstruction of a single event is approximately 50-100 ms on a 600Mhz CPU, leading to a total time for the full processing that is $\sim$100 times larger than the corresponding data taking. This is a direct consequence of the complexity of the CLAS detector.
Because of the large amount of data and the complexity of the reconstruction code, a particular care is dedicated to monitoring this process in order to identify any failure of the code or problem that may affect the data quality. This part of the process is also used to identify bad data files that are affected by hardware faults of the detector not seen at the time of the data taking. The outputs of the monitoring programs (trk_mon, pid_mon, sc_mon, rf_mon, scaler_mon, pdu_mon), for example number of tracks per sector, mean energy released by electrons in the calorimeters, etc., are saved together with the reconstructed data. An examples of monitoring histograms is shown in figure 4.1. A similar analysis is performed again at the level of the physics analysis (see section 5.3) to check in details the quantities of interest of that particular reaction.
The result of the monitoring process are summarized in a database that is automatically updated during the data processing and can be browsed to perform an accurate selection of the 'golden' runs.

4.3 Tracking Reconstruction

The reconstruction of charged particle tracks is the most complex part of the reconstruction code.
The tracking process is performed in two stages. In the first stage, individual tracks are fit only to the hit-wire position in a procedure known as 'hit-base' tracking (HBT). In this part, tracking data are combined into track segments within the individual superlayers and these segments are then linked to form tracks across the three Regions within

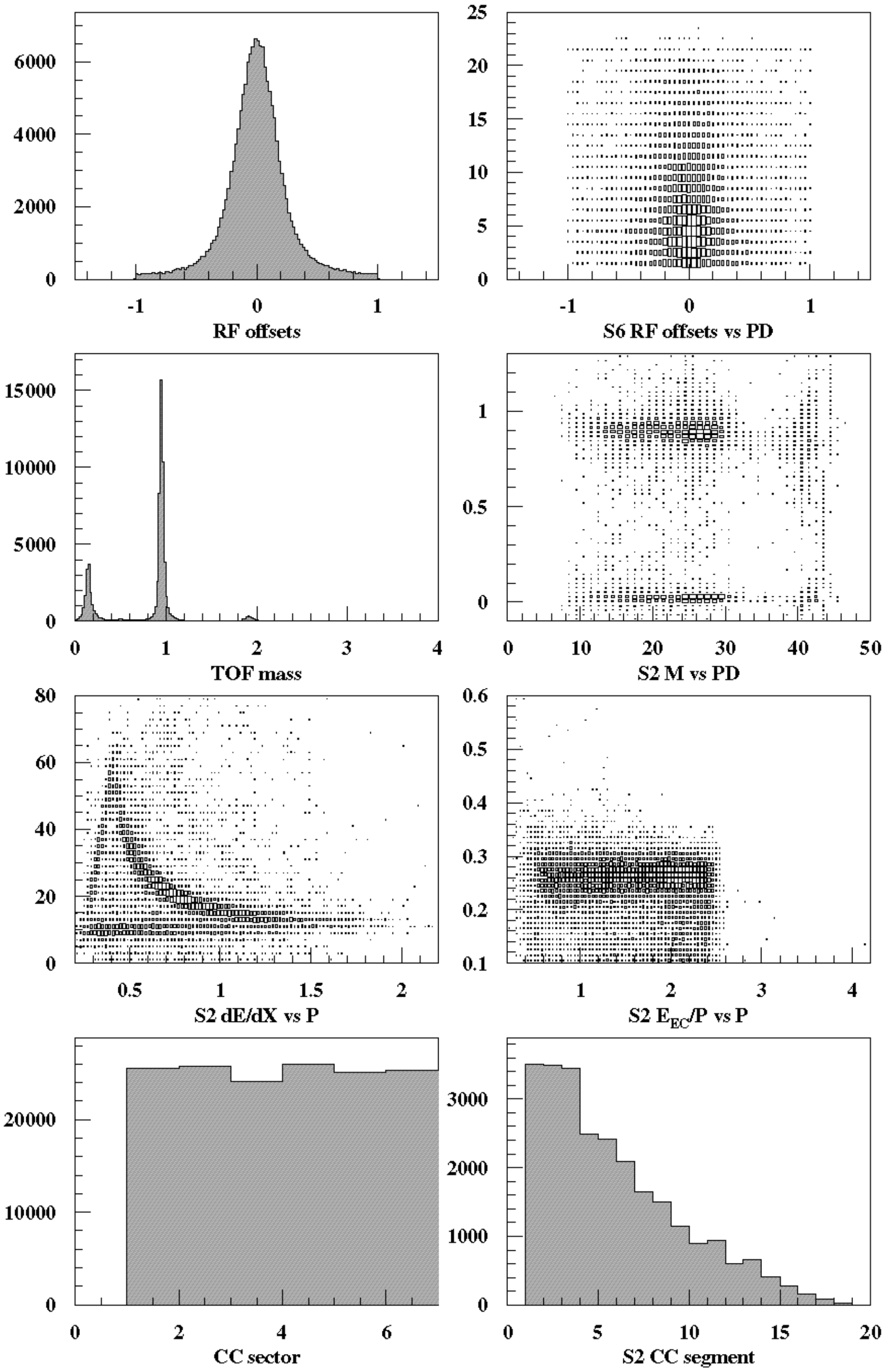

Figure 4.1: *Sample of the monitoring histograms used to check the data quality. The top left plot shows the distribution of the RF correction. The same quantity is shown in the top right plot as a function of the time of flight paddle in sector 6. The third and fourth plots are typical examples of the reconstructed hadron mass. The fifth plot shows the dE/dX versus momentum distribution reconstructed from the electromagnetic calorimeter, while the sixth plot represents the ratio between released energy and momentum for the primary electron. The bottom plots shows the number of hits in the Cerenkov Counter as a function of the CLAS sector and of the Cerenkov segment.*

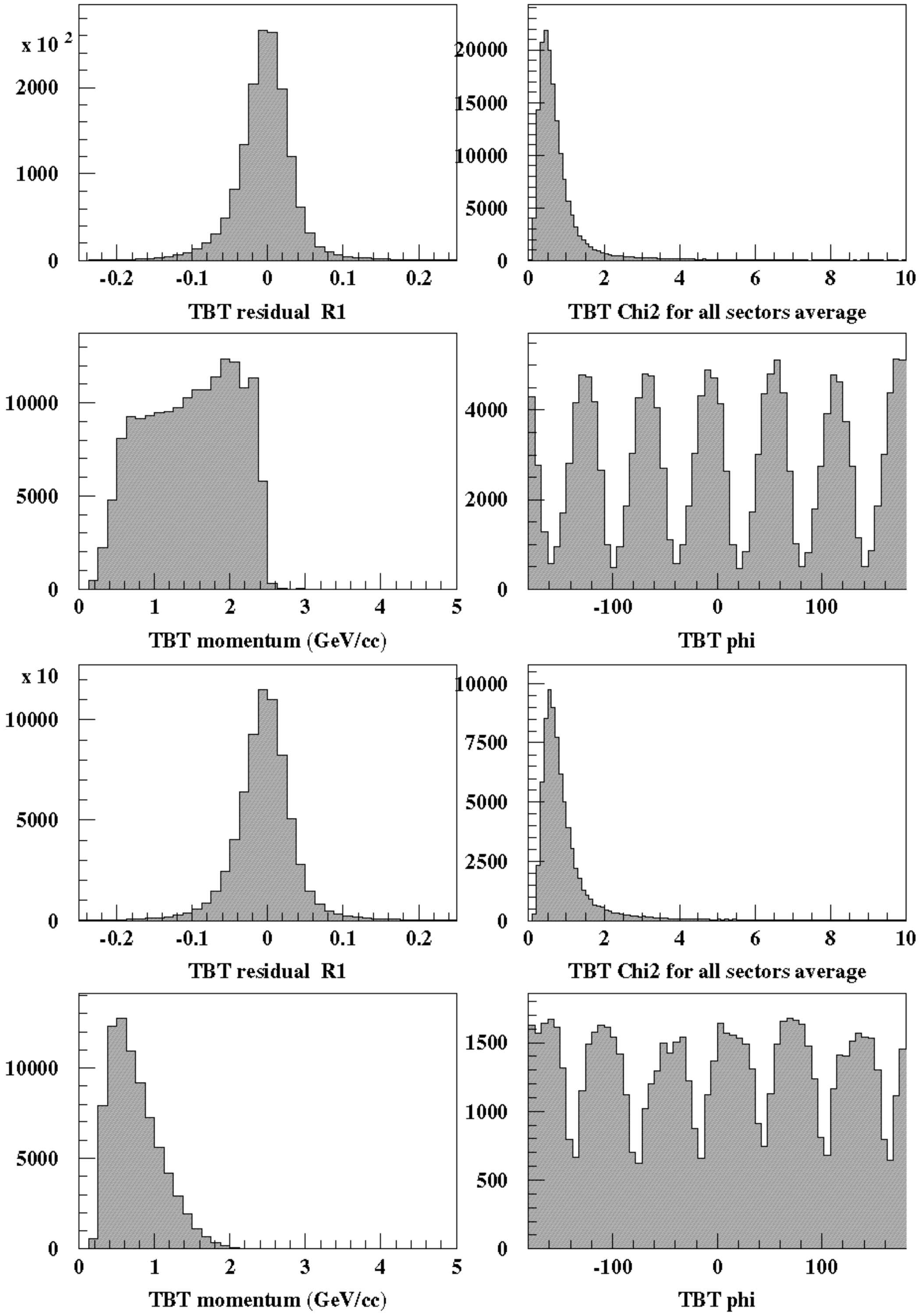

Figure 4.2: *Sample of the monitoring histograms that are used to verify the quality of the tracking reconstruction. The top plots show the time base tracking residual (the distance between the measured and fitted hit position) and χ^2 for the primary electron, while the plots in the second row are a typical example of the momentum and ϕ distribution of the reconstructed electron candidates. The other plots represent the same quantities bu in the case of a proton candidate.*

one sector. The segments finding procedure utilizes a dictionary of known segments that is generated from simulation. The same procedure is also used to link the segments to form a track: in this case a dictionary of tracks is used and the segments combination is considered a track candidate when a match for at least five superlayers is found. The candidate track is then fit using the cell centers as hit position to obtain the associated particle momentum. Due to the comparatively small size of the drift cells and the large number of wire layers, the track momenta can already be reconstructed with a resolution of 3% to 5%. Additional information on these tracks from the Cerenkov, time of flight and electromagnetic calorimeters, allows the determination of the identities and speeds of the charged particles.
In the second stage of the analysis, the drift time information is used to improve the tracking resolution. The particle time of flight from the target to the outer scintillators is used to correct the measured TDC times. A pre-determined table is then used to convert the corrected drift times to drift distances. These corrected track positions in each drift cells are fit in a procedure known as 'time based' tracking in order to determine the final track parameters.
The drift time is given by the following expressions:

$$t_{drift} = t_{start} + t_0 - t_{TDC} - t_{flight} - t_{prop} - t_{walk} \tag{4.1}$$

where t_{start} is the event start time, t_0 is the fixed time delay for the wire, t_{TDC} is the raw time measured by the TDC, t_{flight} is the flight time of the particle from the reaction vertex to the wire, t_{prop} is the signal propagation time along the wire, and t_{walk} is a time-walk correction made for short drift times due to different ionizations for slow and fast particles. The t_{TDC} is subtracted in the previous equation because the TDCs are operated in common stop mode[1]. All these parameters are fixed during the calibration of the drift chamber system.
Through the use of an appropriate function, the drift time determines the distance of closest approach (DOCA) of the charge-particle track to the sense wire. However there remains an ambiguity regarding which side of the sense wire the track passed by. This 'left-right ambiguity' is resolved within the individual superlayers by comparing the χ^2 values for the fit for all different combinations of the drift-distance sign. After the selection of the full set of drift-distance signs, a final fit results in improved track parameters.
The tracks that compose the dictionary used for fitting have been generated in the standard CLAS configuration, i.e. without the polarized target magnetic field. For this reason all these reference tracks are in ϕ-constant plane. In the EG1 configuration, a charged-particle trajectory is bended also in the ϕ direction by the target magnetic field. The effect is mainly limited to the space region inside the first drift-chamber layer since the target magnetic field decreases rapidly with the distance. The EG1 reconstruction code has been therefore modified to fit the track only from the first drift chamber layer to the outside. Knowing the track momentum, hit, and direction at the first drift-chamber layer the track is then traced back to the vertex by calculating the field path integral (see figure 4.3) in the inner region.

[1]The start signal to the TDCs is provided from the individual wire hits, while the stop is provided by a delayed version of the CLAS trigger

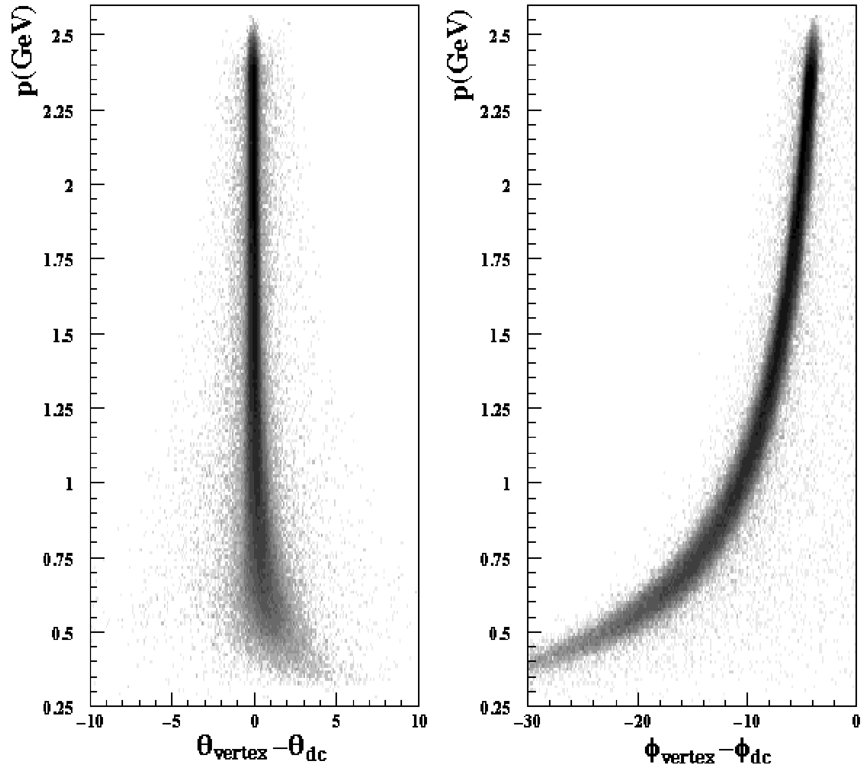

Figure 4.3: *Effects of the reswimming of the charged particle track from the drift chambers to the interaction vertex. The left plot shows the difference between the track polar angle at the vertex and at the first drift chamber layer as a function of the track momentum for electrons. The right plot shows instead the difference of the azimuthal angles. The effect of the target magnetic field is to modify the azimuthal angle of the outgoing particle while the polar angle, ecept for very small momenta, remains unchanged.*

4.4 Start Time Reconstruction

During electron scattering experiments in CLAS there is no direct measurement of the start time, i.e. the time when the interaction between the projectile and the target occurred. This information is derived indirectly by identifying the primary scattered electron in the event and reconstructing the event start time from its measured time of flight. The electron identification can in fact be performed independently from the the time of flight information by analyzing the signal detected by the Electromagnetic Calorimeter and Cerenkov Counter and requiring the match with a negative track. As explained in section 2.9 these two detectors form in fact the electron trigger. When the electron is identified, its signal in the time of flight can be used as reference time and the path information provided by the tracking can be used to trace back the time of the interaction. The start time is given by the following expression:

$$t_{start} = t_{tof} - \frac{l}{\beta c} \tag{4.2}$$

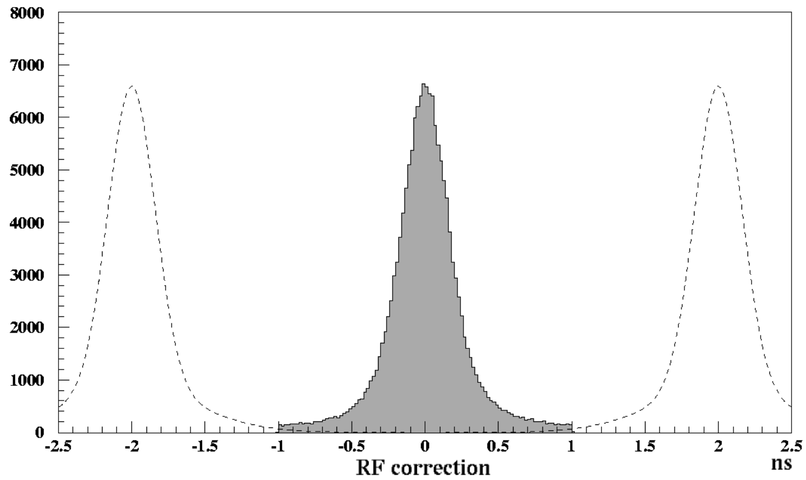

Figure 4.4: *Time difference between the reconstructed start time from the time of flight information and the accelerator RF signal. The time of flight resolution is approximately 160 ps, resulting in the shown distribution. The use of the RF information allows the improvement of the start time definition. However, as indicated by the plot, there is a finite probability of assigning the electron to the wrong bunch since there is an overlap between the distributions of the close bunches. This overlap is anyhow less than 1%.*

where t_{tof} is the time corresponding to the electron signal in the time of flight, l is the path length of the electron track from the interaction vertex to the scintillators, and since the electrons are ultrarelativistic β is equal to 1. The resolution resulting from this method is affected by the intrinsic resolution of the time of flight system. This, as reported in section 2.8, varies from 80 ps to 160 ps moving from the forward angle to large angle strips.
The determination of the start time can be improved exploiting the information of the RF structure of the electron beam. A signal synchronous with the arrival of the electron bunches is in fact recorded in the data stream. This signal has a period of $\sim$ 2 ns corresponding to the time delay between to subsequent bunches. For an infinite time of flight resolution, the start times reconstructed using eq. 4.2 should correspond exactly to the arrival time of one of the electron bunches. Since the resolution is finite, the reconstructed start times gather around the RF signal with a width given by the time of flight resolution (see figure 4.4). The time difference between the event-reconstructed start time and the arrival time of the closest bunch gives the RF correction. The corrected start time is therefore given by

$$t_{start} = t_{tof} - \frac{l}{\beta c} + t_{RF}. \tag{4.3}$$

As shown in figure 4.4, the start time distributions for events belonging to different electron bunches overlap, giving a non zero probability of associating an event to the wrong bunch. The resulting effects is represented in figure 4.5, that shows the β versus p distribution for positive hadrons obtained with RF correction. In addition to the expected pion, kaon, proton and deuteron lines, spurious lines appear when the start time is shifted by 2ns. This affects only a very small portion of the events giving instead

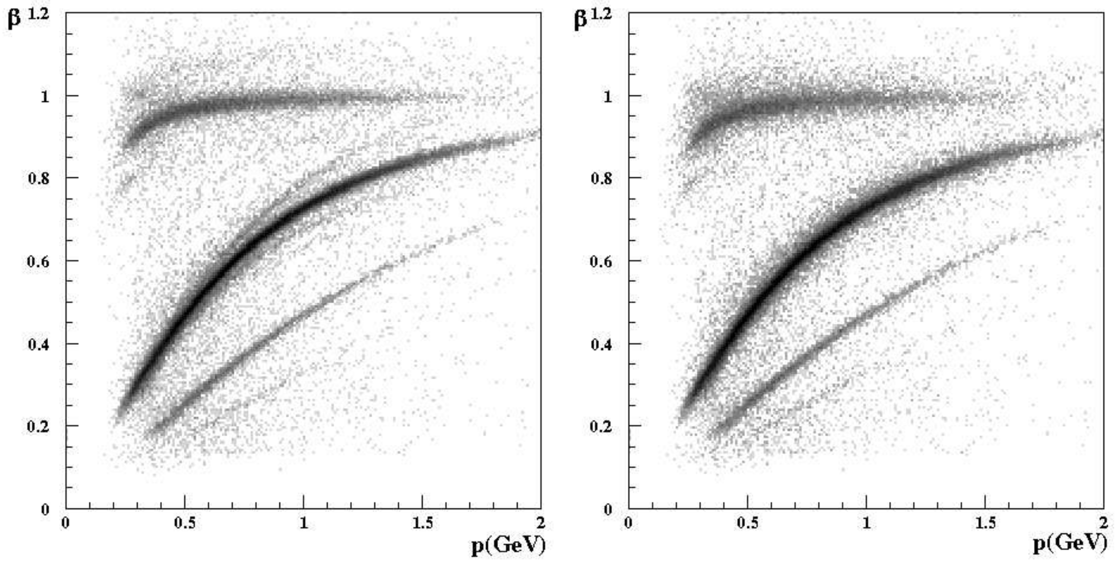

Figure 4.5: *β versus p distribution for positive-charged hadrons with (left plot and without (right plot) RF correction.*

a significant improvement in resolution necessary for the kaon detection.
For pion and proton detection the RF correction is not strictly necessary since while pion and proton produce an overwhelming contamination on the kaon sample, the kaon rate is intrinsically too low to produce a significant effect on the other hadrons. In this analysis no RF correction have been applied.

4.5 Matching with the Outer Detectors

After the completion of the tracking reconstruction, the identified track paths are prolonged to hit the outer detectors. A hit in the outer detectors within a limited distance from the projected hit is associated with the track. The matching cut is chosen differently for each detector.
For the Cerenkov Counter the required condition is a maximum polar angle of 12° between the projected track intersection with the CC plane and position of the detected hit. Since the Cerenkov Counter does not provide information on the azimuthal angle of the hit no further selection is applied. The cut correspond to approximately 3 Cerenkov segments and is therefore a very loose cut.
The matching of the track with the time of flight hit is fixed requiring a maximum distance between the hits projection on the z-axis of 30 cm. The z-axis projection of the time of flight is completely determined by the geometry and simply depends on the scintillator strip that detected the signal. Again no information on the azimuthal position of the hit is used.
The hit position in the Electromagnetic Calorimeter is reconstructed from the location of the scintillator strips that detected the signals. As reported in section 2.7.1 in each stack of the forward calorimeter the scintillators are positioned in three 'views' rotated by 60°

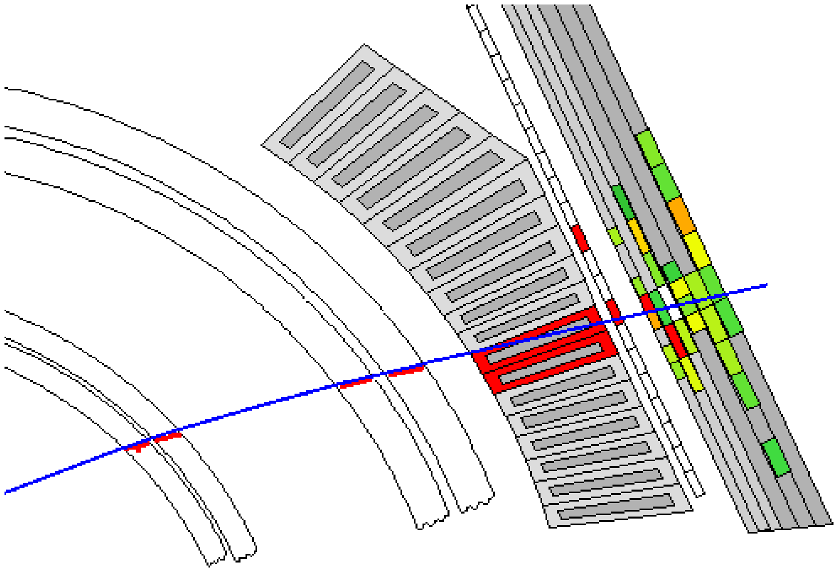

Figure 4.6: *Matching between an electron track and the Cerenkov Counters and the Electromagnetic Calorimeter signals.*

relative to each other and give a direct information on the hit position. The matching requirement consist on a radial cut of 30 cm from the detected hit.
An example of match between a charged particle track and its hit in the outer detectors is given in figure 4.6.

4.6 Particle Identification

4.6.1 Electron Identification

Since the EG1 trigger was a coincidence of the electromagnetic calorimeter and the Cerenkov Counter, each event has an electron candidate. At the level of the reconstruction process events in which the presence of an electron is not confirmed are rejected since no start time reconstruction is possible. The percentage of electron candidates that remains after the reconstruction depends on the beam energy, on the toroidal field and on the trigger thresholds. For the 2.5 Gev data, whose analysis is discussed in this thesis, the reconstruction efficiency was approximately 60%, that means that $\sim$ 40% of the triggers do not have a negative track.
At this stage an electron is represented by a negatively charged particle with track hits in the EC, CC, and TOF detectors. Since the matching requirements are given by loose cuts, the electron sample after the reconstruction can be still affected by contamination from other negative particles. The electron selection is improved at the level of the physics analysis by using additional cuts on

- energy released in the electromagnetic calorimeter,
- signal in the Cerenkov counters,

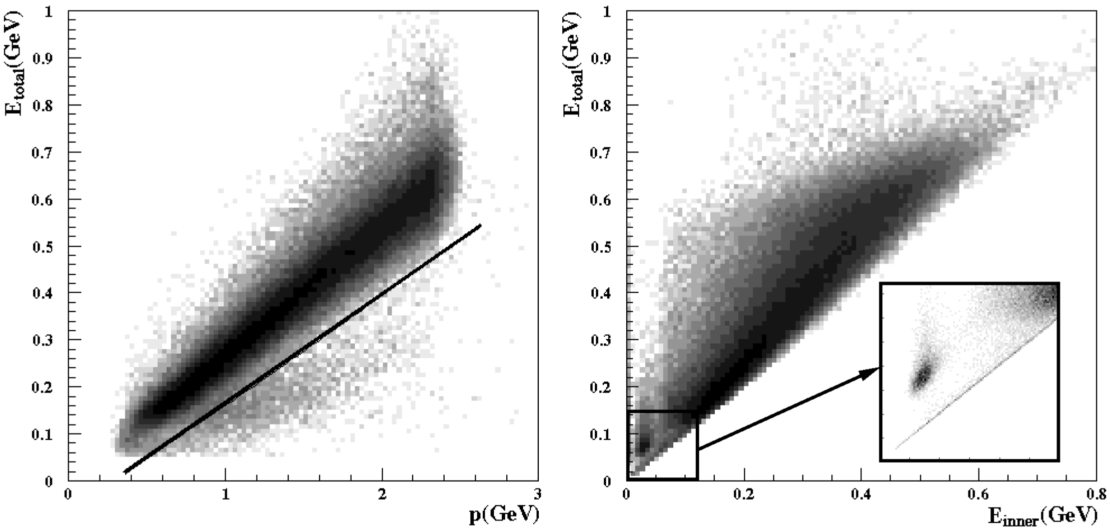

Figure 4.7: *EC_{tot} versus p and EC_{tot} versus EC_{in} distributions for electrons. As shown in the left plot, electrons are expected to release a constant fraction of their energy. This feature is exploited to remove the possible contamination in the electron sample. As highlighted in the right plot the electron sample is in fact contaminated by minimum-ionizing particles that can be recognized by the typical behavior. This contamination has been eliminated removing the isolated spot.*

- vertex cut.

The first cut makes use of the different modes in which electron and pion deposit energy in the calorimeter. Electrons interact producing showers and release a total energy that is proportional to their kinetic energy. The typical distribution of deposited energy versus momentum for electrons is shown in figure 4.7. The sampling fraction $\alpha = E_{total}/p$ is determined by the characteristic of the detector and in the present case is ~ 0.27. When the electron hit is close to the calorimeter edges, part of the shower can 'leak' outside and in this case the energy is not fully reconstructed. The problem is solved by choosing the electrons within a safe region that exclude the detector edges (see left plot in figure 4.7). After this selection we have still applied a cut represented by the lines in the right plot

$$\frac{E_{total}}{p} > \alpha(1 - 3\sigma) \tag{4.4}$$

where σ is the width of the E_{total}/p distribution, i.e. $\sim 10\%$. On the contrary the primary mode of interaction for pion is ionization. In particular for minimum ionizing particles the energy that is deposited both in the inner and outer stack of the calorimeter is almost independent on the pion kinetic energy and is only related to the detector thickness. Therefore this condition is identified by a precise correlation between E_{tot} and E_{innner} ($E_{total} : E_{inner} = 13 : 5$). Particle with this feature inside the electron sample are a clear symptom of pion contamination (see right plot in figure 4.7). The distribution of these particles in the E_{total} versus E_{inner} plot does not overlap with the real electrons and can therefore be suppressed by a cut in the E_{total} vs. E_{inner} plane to reject the spot highlighted in figure 4.7. This cut was simply chosen to be $E_{inner} > 50$ MeV.

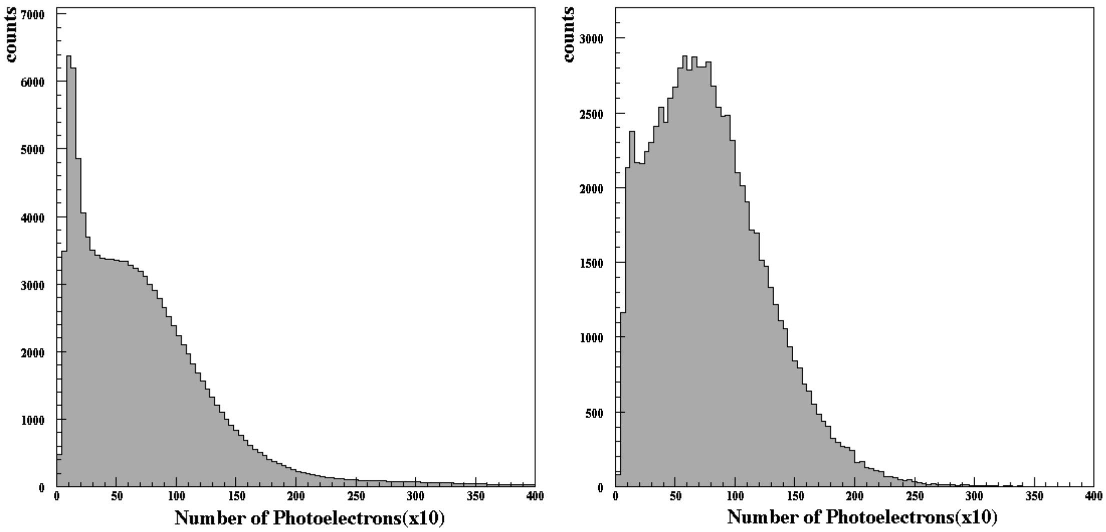

Figure 4.8: *Distribution of the number of photoelectrons detected in the Cerenkov counter. The left plot shows the original distribution obtained for electrons with no cuts applied. The right plot shows the same distribution for the* $ep \to e\pi^+ n$ *channel requiring the electron to be wtihin the fiducial cuts.*

In addition to the EC signal, the electron identification is performed requiring a signal in the Cerenkov Counter. The typical photoelectrons distribution is shown in figure 4.8. The distribution is the result of the convolution of the poissonian distribution that describes the emission of Cerenkov light with the response of the PMTs. The peak at ~ 2 photoelectrons is mainly due to a bad recollection of the Cerenkov light that occur for a particular kinematics. It has been shown in fact that for fixed-momentum electrons there is a particular combination of the electron angles ϕ and θ for which the Cerenkov PMTs do not receive the light (see left plot in figure 4.9). This clear inefficiency is eliminated by defining a fiducial region as shown in the right plot in figure 4.9 that exclude this holes as well as the fringes created by the mirror geometry. This fiducial cuts is defined as a function of the electron momentum and angles. As a result of this selection the 2-photoelectrons peak in the Cerenkov response disappear (see right plot in figure 4.8). In addition this fiducial region excludes the edges of the calorimeter so that the shower of the accepted electrons is fully reconstructed.
The elastic cross-section was measured using these cuts and the result agreed within few percent with the known cross section.
The definition of the fiducial region has been studied separately for the six sectors of CLAS. The cuts have been defined excluding the regions that present low rates not only for the inefficiency of the Cerenkov detector but also for additional hardware problems, as dead PMTs in the Time of Flight system or broken wires in the Drift Chambers. An examples of these additional cuts is given in figure 4.10.

The final selection on the electron sample is performed by studying the vertex distribution. An example of the z coordinate of the vertex as reconstructed from the tracking is shown in figure 4.12 as a function of the azimuthal angle ϕ. The evident dependence from the angle is given to the non-perfect alignment of the polarized target in respect

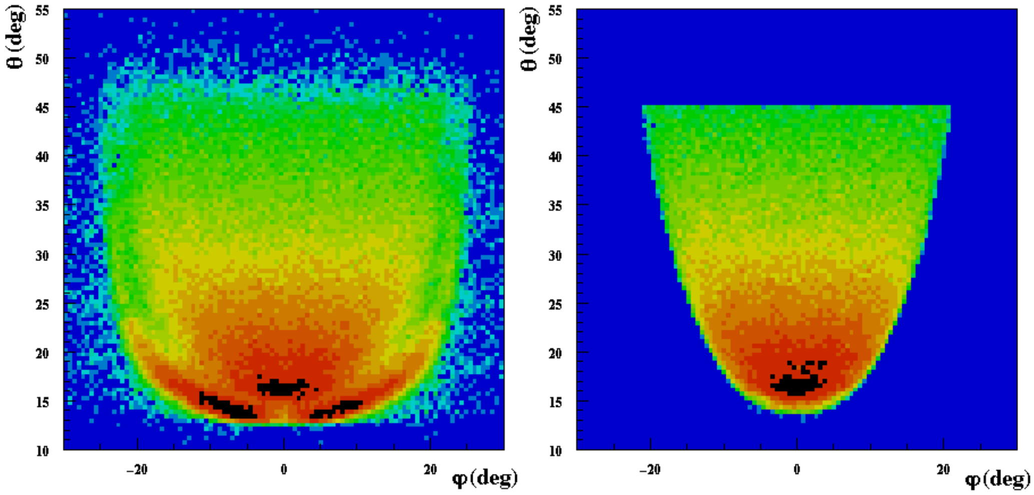

Figure 4.9: *Fiducial region for the scattered electron. The left plot shows the θ versus ϕ distribution of the scattered electrons in one sector. The fringes created by the Cerenkov Counters are evident at low θ. The fiducial region (right plot) is defined to reject these low efficiency regions.*

to the center of the detector that is not taken into account by the reconstruction code. The shift can be easily corrected by calculating the true vertex coordinate as

$$z_{true} = z_{meas} + a \tan\theta \sin(\phi - \phi_0)$$

where the parameter a represents the distance between the target axis and the detector axis and ϕ_0 is the angle between the plane that contains the target and detector axes and the horizontal plane. The corrected vertex coordinate does not show any ϕ dependence (see figure 4.12) and the resulting distribution allows a precise selection of the electrons associated with the real target material. The final cut was chosen to be

$$-60cm < z_{true} < -50cm$$

excluding completely the contribution from the cryostat windows.

4.6.2 Charged Hadron Identification

Hadrons are identified by the combined information of the drift chambers and time of flight. The two detectors provided in fact the path and time of flight information necessary for the calculation of the β of the particle. This is obtained as

$$\beta = \frac{l}{tc} \tag{4.5}$$

where the l is the path length from the vertex to the time of flight plane and t the correspondent time obtained, as explained in section 4.4, as $t_{TOF} - t_{start}$.
The mass of the hadrons can then be calculated as

$$m = \sqrt{\frac{p^2}{\beta^2} - p} \tag{4.6}$$

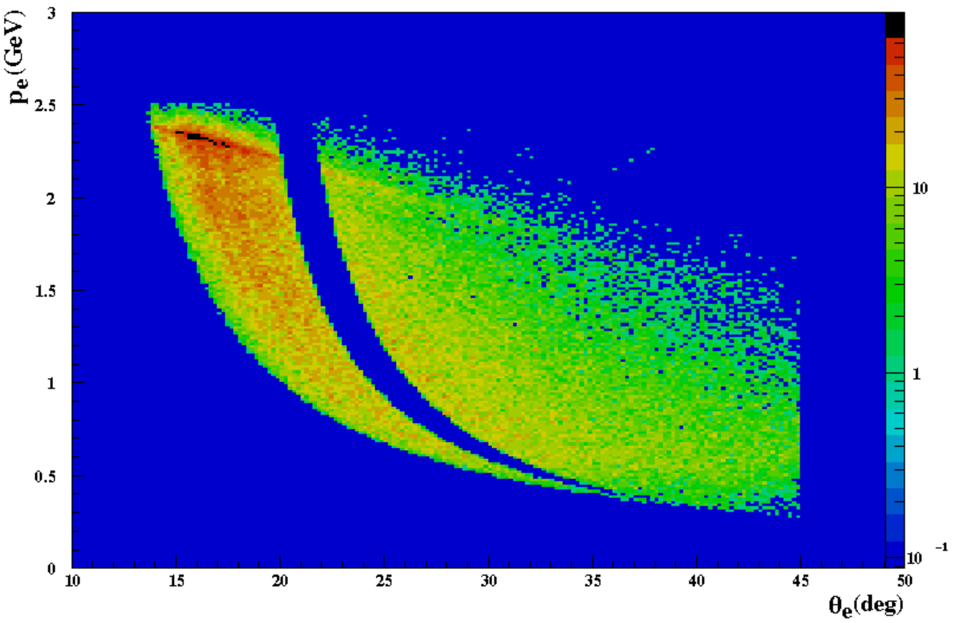

Figure 4.10: *Momentum versus polar angle distribution for the scattered electrons in one sector. The solid lines represent the cut that were defined to reject the low efficiency regions due to hardware faults in the time of flight system or dead wires in the drift chambers.*

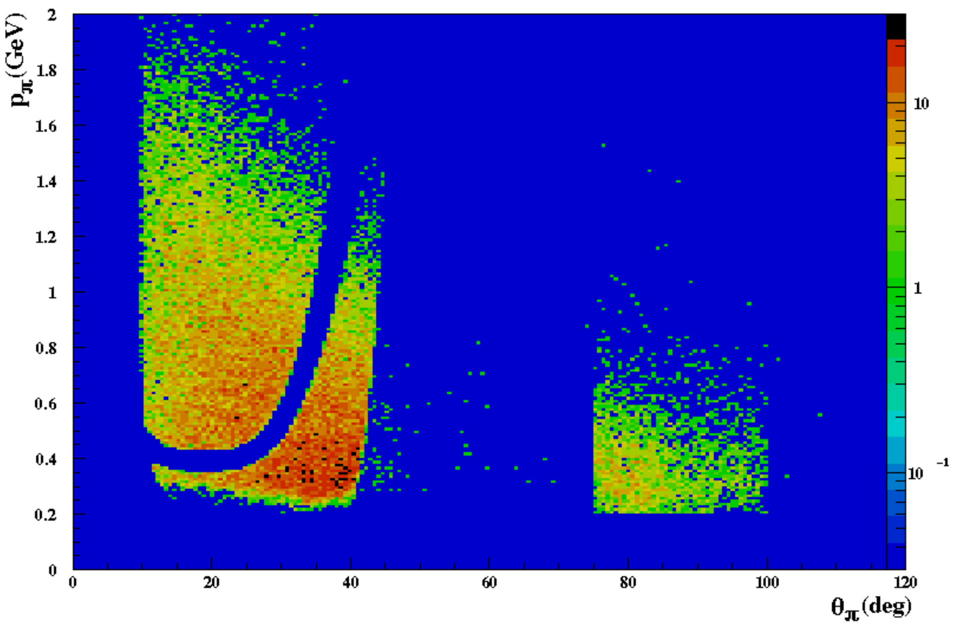

Figure 4.11: *Momentum versus polar angle distribution for the scattered pion in one sector. The blind region between 45 and 75 degrees correspond to the coils of the target magnet. The empty band represents a cut that was defined to reject the low efficiency regions due to hardware faults in the time of flight system or dead wires in the drift chambers.*

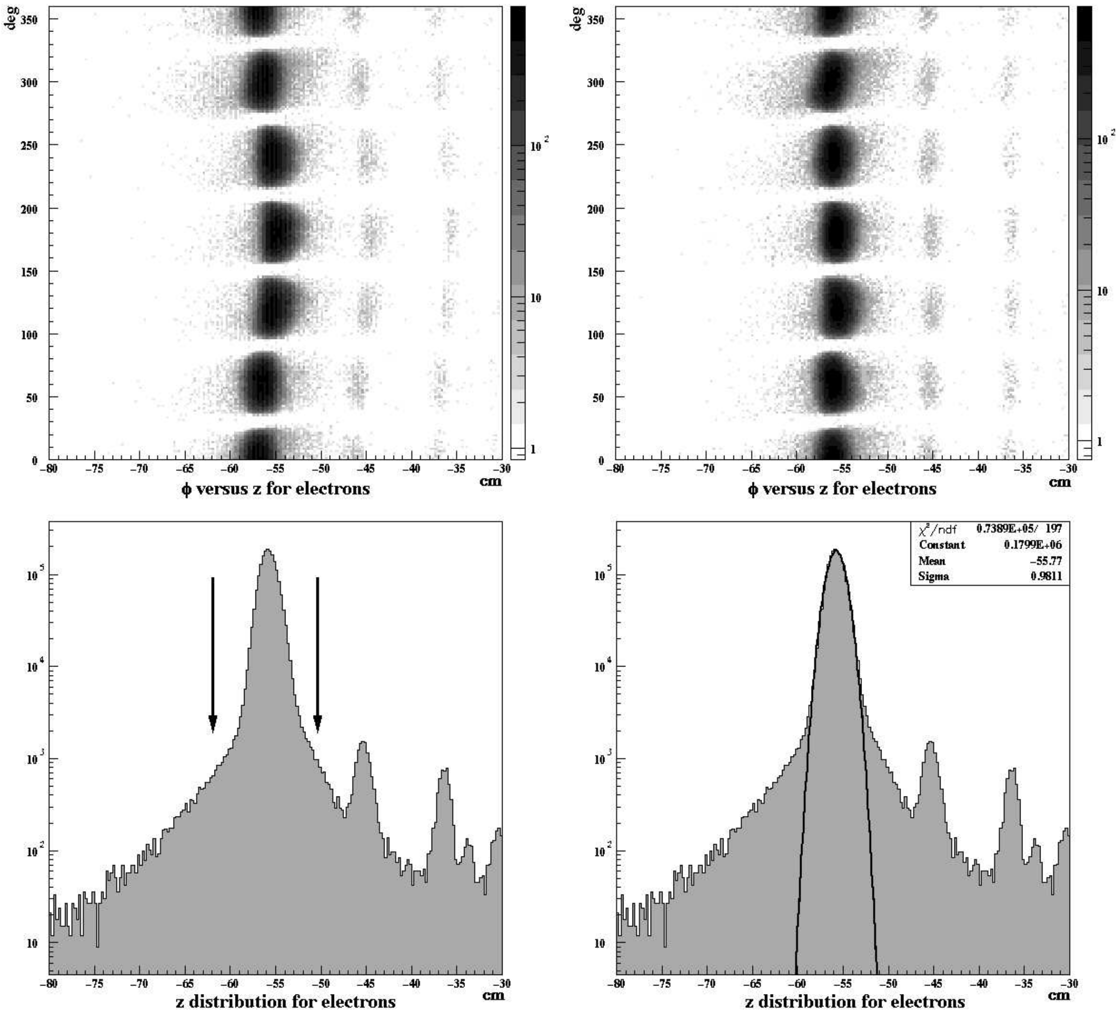

Figure 4.12: *Vertex reconstruction for the primary electron. The top-left plot shows the ϕ versus z distribution as reconstructed from the data processing. The reconstructed z coordinate is corrected to take into account the shift of the target position and the result is shown in the top-right plot. The projection (bottom left) shows clearly the cryostat windows that are removed using the cut indicated by the two arrows. The remaining distribution has a sigma of approximately 1 cm, compatible with the target length.*

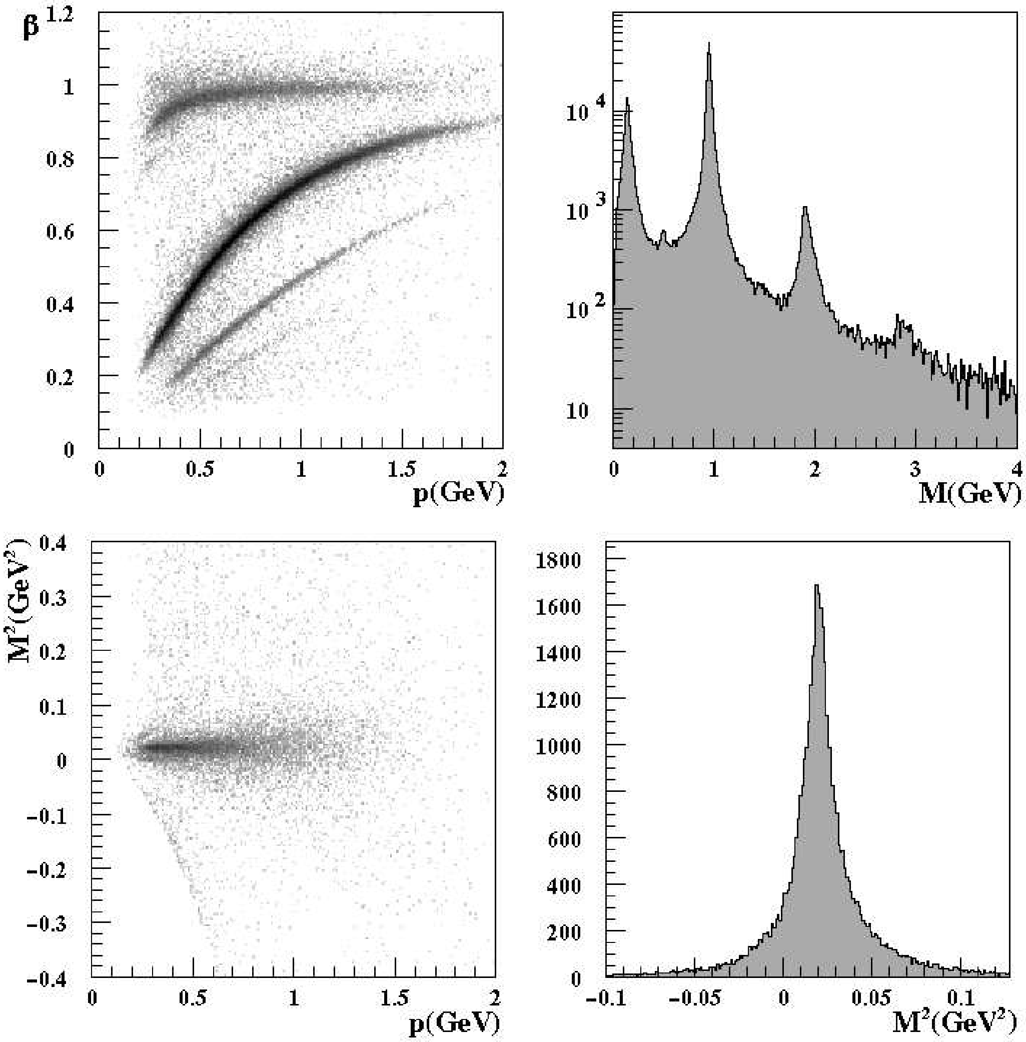

Figure 4.13: *Identification of charged hadrons. The top-left plot shows the β versus p distribution for positive-charge hadrons while the top right plot shows the reconstructed mass. The bottom left-plot shows the mass squared versus momentum distribution for identified pions while the bottom right plots shows the projected squared mass.*

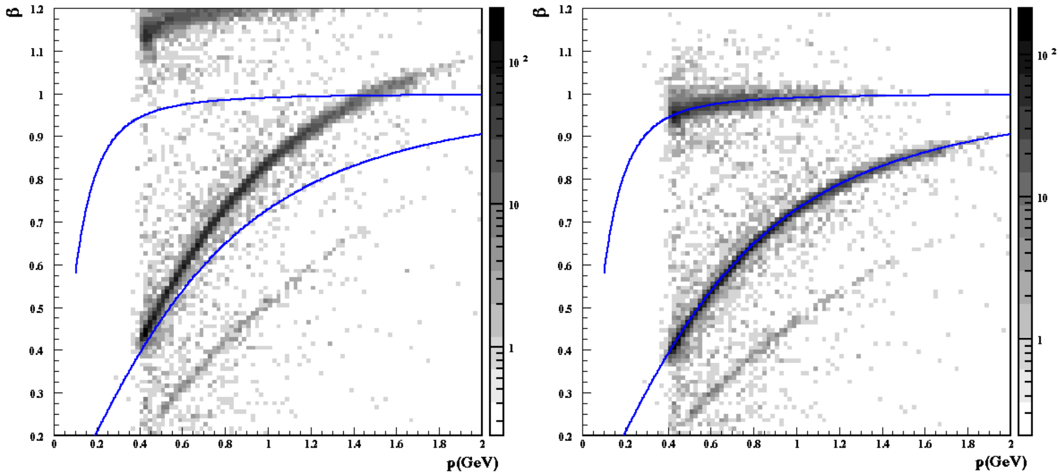

Figure 4.14: *β versus momentum plot for positive particles for a specific time of flight paddle before (left) and after (right) the correction of the calibration constant.*

The resulting mass distribution for positive hadrons is shown in figure 4.13. Since the mass resolution depends on the time resolution that decreases for very fast particles, the final hadron identification is performed with cuts in the β versus p distribution that are chosen according to that resolution. A typical example is shown in figure 4.15.
The choice of the β versus p cuts for positive pions was studied in details in the present analysis both to remove any possible contamination from positrons and to exclude any distortion of the angular distribution caused of the PID cut. The response of each scintillator paddle was checked separately to identify the malfunctioning or miscalibrated scintillators. The calibration procedure can in fact fail when a scintillator has one dead PMT or TDC. In this case the signal is still seen by the other PMT and the corresponding event is reconstructed. Nevertheless the resulting β can be shifted in respect to correct value or the resolution can be worse. Scintillators showing a shift in β can be recovered performing an additional dedicated calibration. This is obtained recalculating the event start time from the positive hadrons information and in the assumption of a pure pion sample

$$t^{\pi}_{start} = t_{TOF} - \frac{\sqrt{p^2 + m_\pi^2}}{p}\frac{l}{c} \tag{4.7}$$

The resulting time distribution presents a clear peak corresponding to the real pions in the hadron sample for which the mass assumption was correct and a smooth background for the remaining hadrons. The difference between this recalculated start time and the original start time gives the time shift that need to be applied (see figure 4.14).
Paddles with a bad resolution can instead be recovered by using wider β versus p cuts. This problem affects in particular the large angle part of the time flight system where two scintillator strips are connected to the same TDC for the time measurement. This configuration does not create an intrinsic problem since only low momentum particles reach the large angle strips and the resulting resolution is anyhow sufficient to separate the different hadrons. Nevertheless to avoid distortion in the hadron angular distribution, it is important to consider this feature in the definition of the particle id cuts. An example of 'paddle dependent' cuts is given in figure 4.15.

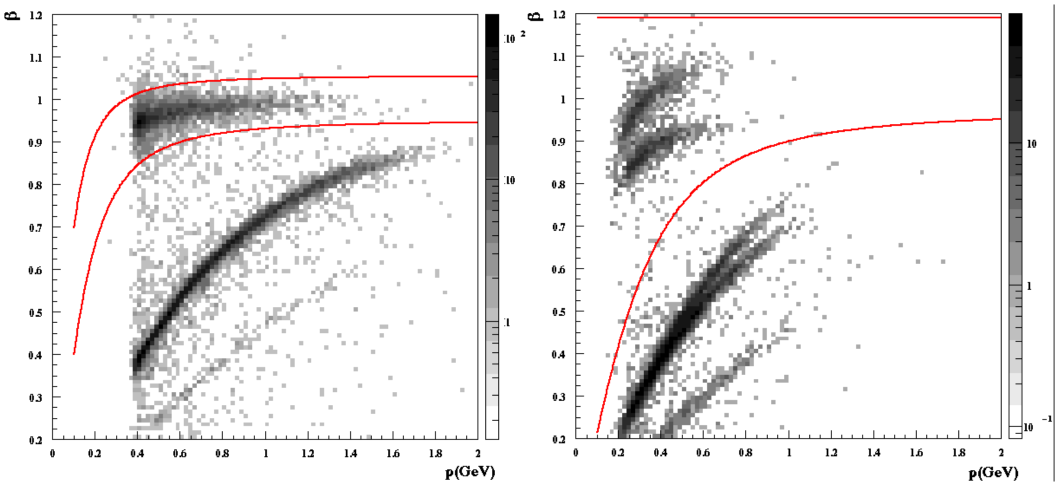

Figure 4.15: *β versus momentum plot for paddle 22 (left) and 43 (right). The lines represent the cuts that have been chosen for the particle identification. For large angles paddles, like the right one, wide cuts were chosento be able to select simultaneously the particles detected from the two paddles that are connected to the same tdc.*

The few scintillator strips that cannot be recovered with these methods (4%) are usually rejected from the analysis. This is accomplished by introducing also for hadrons a set of fiducial cuts that define the high-efficiency regions of the detectors. These were originally meant to exclude the edges of the drift chambers where loss of efficiency can occur (see figure 4.11) but have been modified to reject the region corresponding to malfunctioning paddles of eventual holes in the drift chambers. The effect of this cuts is included in the evaluation of the CLAS acceptance as explained in section 5.8.

4.6.3 Neutral Particle Identification

The detection of neutral particles in CLAS is performed by the electromagnetic calorimeters. The presence of a hit without a matching track represents in fact a neutral candidate. Such signal is then analyzed by the reconstruction code to reconstruct the β of the particle. The trajectories of the neutral particles are obviously not affected by the magnetic field and therefore the path length can be simply calculated as the distance between the vertex and the detected hit position. The β is therefore obtained as in eq. 4.5. The resolution of the electromagnetic calorimeters is sufficient to obtain good photon-neutron discrimination up to a particle momentum of 1.5 GeV. At higher momenta, neutrons can be better identified by excluding the hits in the inner part of the calorimeter. Although this reduces the neutron detection efficiency, it efficiently removes photons since they rarely passes through six radiation lengths without depositing detectable energy.
Candidate events corresponding to $\pi^0 \rightarrow 2\gamma$ decays are obtained requiring two photon hits in the calorimeters. From the measured energy E_γ and polar angle θ_γ of each photon, the invariant mass can be reconstructed as

$$M_{2\gamma} = 2E_{\gamma 1}E_{\gamma 2}(1 - \cos(\theta_{\gamma 1} - \theta_{\gamma 2})). \tag{4.8}$$

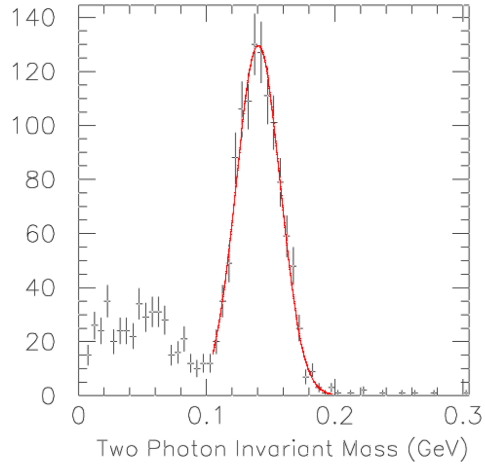

Figure 4.16: *Gaussian fit to the measured π^0 mass. This was reconstructed as the invariant mass of the two photon detected by the electromagnetic calorimeter.*

A typical example of the reconstructed π^0 mass is given in figure 4.17.
The CLAS capability of detecting neutrals is in principle an important characteristic since the studied reaction has a neutron in the final state. Nevertheless since the angular coverage for neutral detection is limited, it's preferable not to require the detection of the neutron but to use instead the missing mass technique to select the event contribution to the π^+n channel. This procedure is describe in details in section 4.7

4.7 Missing Mass selection of the $p(e, e'\pi^+)n$ channel

The selection of the $ep \to \pi^+n$ channel is performed using the missing mass technique. The scattered electron and pion are detected in the final state and, applying the constraints of energy and momentum conservation, the mass of the missing particle is calculated. In the present case this is given by

$$M_X^2 = (p_i + k_i - k_f - p_\pi)^2 \tag{4.9}$$

where, using the notation introduced in section 1.2, k_i and k_f are the four-momenta of the incoming and outgoing electron, p_i is the four-momentum of the proton and p_π is the four-momentum of the pion. The previous can be explicitly written for example in the center of mass frame as

$$M_X^2 = W^2 + m_\pi^2 - 2WE_\pi^* \tag{4.10}$$

where E_π^* is the pion energy in this frame.
This approach is preferable than the full detection of the final states since the resulting angular coverage for the reaction is not affected by limited acceptance of the neutron. In addition thanks to the good resolution of CLAS, this technique allows to maintain an excellent separation between the single pion channel and the multi-pion reaction.
An example of missing mass distribution obtained from the EG1 data at a beam energy of 2.5GeV is given by the left plot in figure 4.17. In this case since the target consist

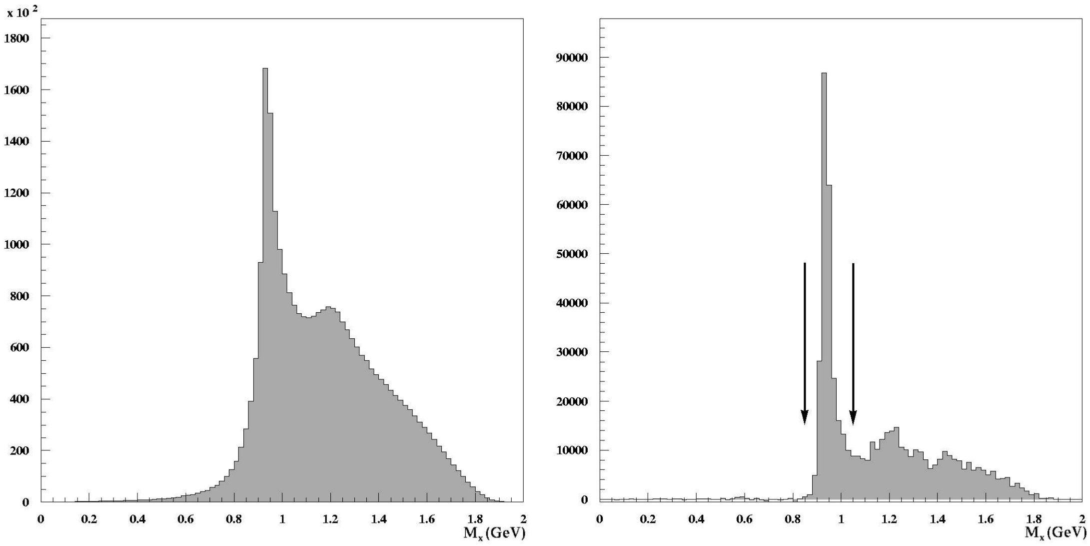

Figure 4.17: *Missing mass plot for the $e\pi^+$ channel. On the left, the plot represents the result obtained from the NH_3 target. The right plot shows the proton contribution separated from the nitrogen using the subtraction method. The two arrows represent the cuts that were used to select the π^+n channel.*

of $NH3$, the clear peak at the neutron missing mass peak is superimposed on a large background due to the nitrogen contribution. At higher missing mass values the two pions contribution appears clearly. The right plot in figure 4.17 shows the same distribution where the hydrogen contribution has been isolated with a subtraction method (see section 5.7).
The good separation between the neutron missing mass peak and the multi-pion contribution is in this case evident. The cut, used to perform the final channel selection, was chosen as indicated by the two arrows as

$$0.85 < M_x < 1.1.$$

The effect of this cut of the final results has been studied in details as discussed in section 6.3.

4.8 Momentum Correction

After the event reconstruction, the W distribution for inclusive electron is one of the tools to check the quality of the tracking. In particular the width of the elastic peak is a direct indication of the accuracy of the momentum reconstruction. In addition since W is an invariant quantity, the value corresponding to the elastic peak should be independent from the kinematics and in particular from the electron angles. However a small angular dependence of the elastic peak position in the W spectrum is observed in the data. This feature has been studied and understood as due to a non perfect description of the drift chamber position in the tracking code and to a small shift of the torus magnetic field map.

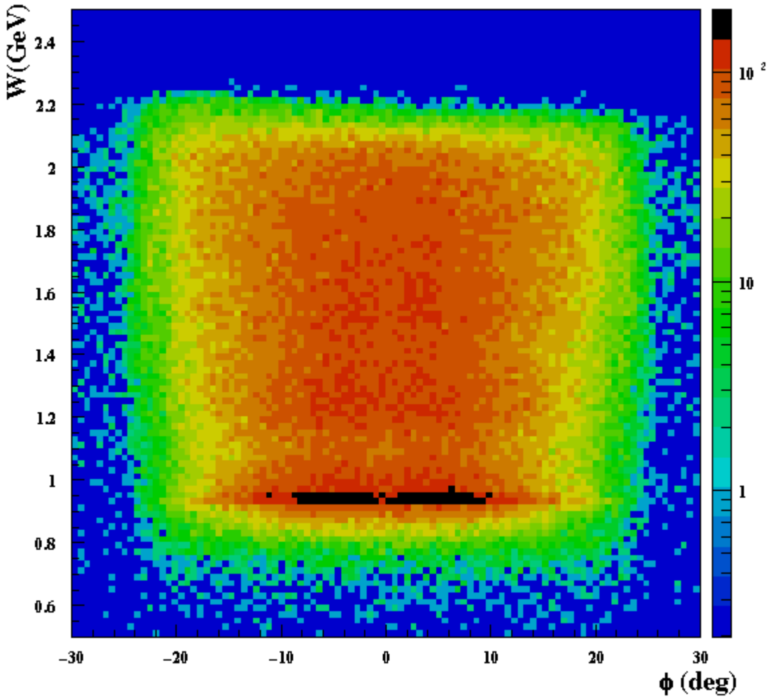

Figure 4.18: *W verus ϕ distribution. After the momentum correction, the position of the elastic peak (dark line) does not show any dependence from the azimuthal angle of the electron.*

To correct for this deviation, the magnitude of the reconstructed electron momentum is adjusted according to the formula

$$p_{corrected} = p_{measured}(a + b\phi + c\phi^2)\frac{d\theta - f}{g\theta - h} \tag{4.11}$$

where the 7 parameters are fitted to the data using as constraint the corrected position of the W elastic peak. The fit is performed separately for the six sectors to account for the possibility of independent shifts in the position of the six parts of the detectors.
The resulting correction on the electron momentum is of the order of $\sim 0.1\%$ and tend to decrease for increasing electron polar angle. The primary effect of this correction is shown in figure 4.19 where the elastic peak in the inclusive W spectrum is shown with and without the correction.
In principle a similar correction should be applied also to the charged hadrons, as the pion in this analysis. Nevertheless the corresponding effect for these particles, observed for example in the angular dependence of the neutron missing mass peak, is negligible. The reason for this is that the correction decreases strongly for increasing θ of the charged particle. The average θ for the detected π^+ is of the order of $35°$ in comparison with the $22°$ observed for electrons.
However the correction on the electron momentum has a positive effect also on other observables as the missing mass distribution. As shown in fact on figure 4.20 the $e\pi^+$ obtained after the correction has a smaller width and is centered on the corrected mass value for the missing neutron.

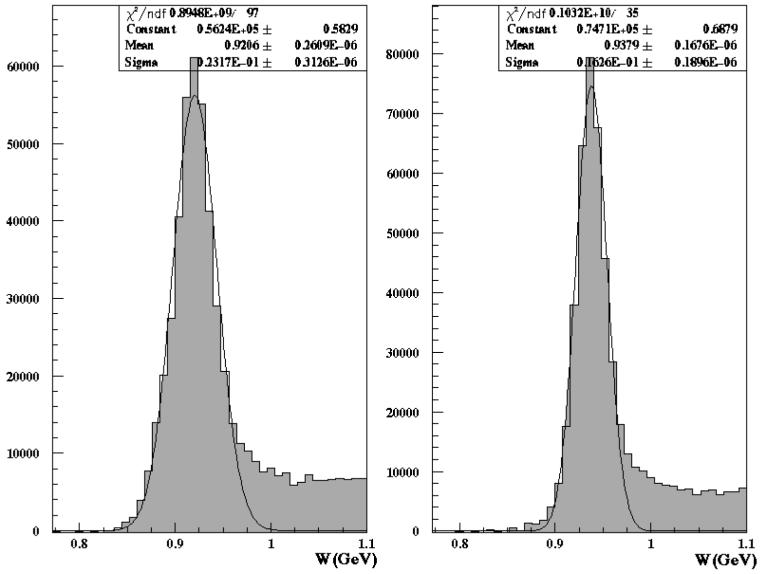

Figure 4.19: *Elastic peak before(left) and after(right) the momentum correction. After applying this correction the elastic peak position is in correspondence of the expected W and the peak width is reduced.*

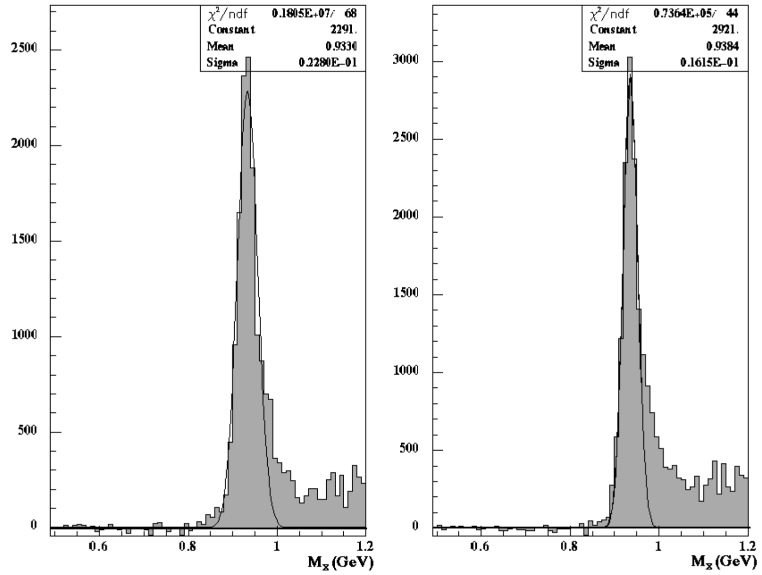

Figure 4.20: *Neutron peak in the missing mass plot before(left) and after(right) applying the correction on the electron momentum. After the correction both the peak position and width show an improvement.*

Chapter 5

Data Analysis

5.1 Introduction

In this chapter I will describe the procedure that I developed and used for the extraction of spin asymmetry in the $ep \rightarrow \pi^+ n$ channel. The final goal of this analysis is the extraction of the double spin asymmetry in this reaction.
The data analysis has been separated into several steps to obtain, starting from the data sample whose selection has been described in the previous chapter, the final results.
In the following I will discuss each step of the analysis starting from the data selection, to the method used to extract spin asymmetries. The correction for the false asymmetry induced by the helicity dependence of the beam current will be discussed in section 5.5. A thorough description of the technique used for the evaluation of the polarization and dilution factor will be given in section 5.6 and 5.7. Finally the last two sections will be dedicated to the discussion of the acceptance and radiative corrections.

5.2 CLAS Data

The present analysis is based on the data from the EG1 run, concluded in December 1998. This run corresponds to approximately 1/3 of the approved beam time and, as mentioned in section 1.4, a second run is presently in progress. Nevertheless the 1998 has already provided more than $3{\cdot}10^9$ triggers and the analysis both of the inclusive and exclusive reactions is in progress.
During the run, both 2.5 GeV and 4.2 GeV electron beam were used and data on hydrogen (NH_3) and deuteron (ND_3) target were recorded. A summary of the '98 run is given in table 5.1.
In this thesis I will discuss the analysis of the 2.5GeV data on proton target with inbending torus configuration ($I = 2250A$)[1]. The main reason for the choice of this particular configuration is the large kinematical coverage available in the resonance region. The Q^2 versus W range accessible with these data is shown in figure 5.1. In addition this set has a similar amount of data with both target polarities that are in fact necessary for the full extraction of the double polarization asymmetry.

[1]The term 'inbending' is used to identify the magnet polarity for which negative particles are bended towards the beam line

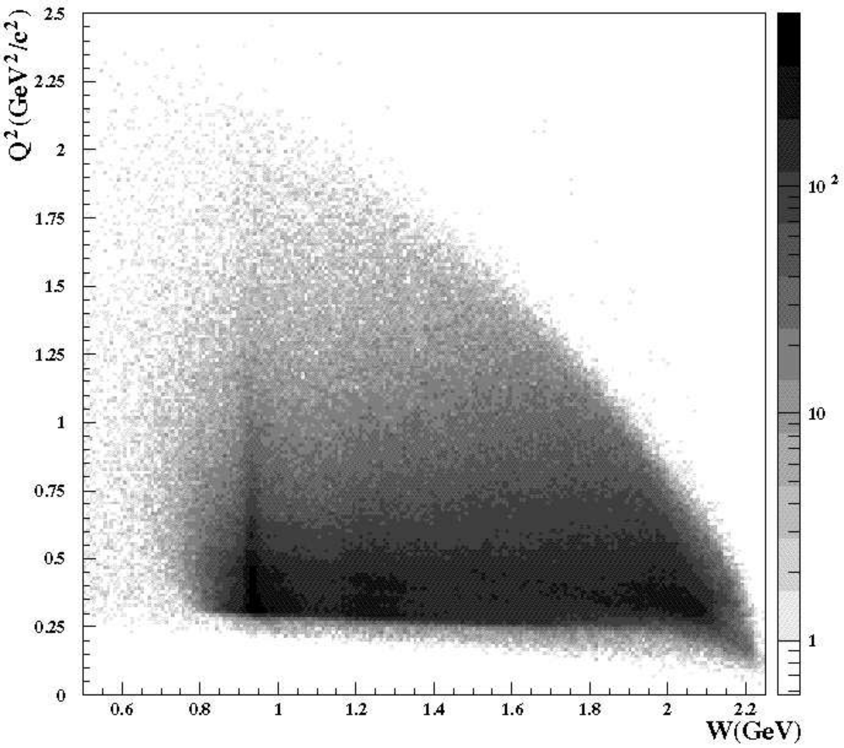

Figure 5.1: *W versus Q^2 range accessible with a 2.5GeV beam in CLAS. The elastic peak is clearly visible in the high density region at $W \sim 1GeV$.*

The total amount of triggers recorded in this configuration is $\sim 250 \cdot 10^6$, corresponding to $\sim 125 \cdot 10^6$ electrons. From this sample and using the selection procedure describe in chapter 4, approximately $0.65 \cdot 10^6$ $\pi^+ n$ events were identified. A full summary of the selectivity of the cuts used for the channel identification is given in table 5.2.
In addition to the NH_3 data, I have analyzed the data at the same energy and magnetic field recorded on Carbon target. These data have been used to evaluate the nitrogen contribution, as will be explained in the section 5.7.

5.3 Quality Checks and Run Selection

A large statistics is one of the necessary conditions to reach a good accuracy in an asymmetry measurement. The absolute statistical error on an asymmetry evaluated from a number of events equal to n is in fact given by $\sigma \sim 1/\sqrt{n}$. As shown in table 5.1, CLAS has provided a significant amount of data, and the EG1 experiment has in fact the basis to provide accurate measurements. Nevertheless when accumulating statistics, it is fundamental to perform an accurate selection of the data runs. This is in general an important control when performing a data analysis. It prevents in fact from using data that may have been affected by a malfunctioning of the detector or of the data acquisition system that was not seen during the data taking or during the event reconstruction. In the case of an asymmetry measurement, this data selection is even more important since

Beam Energy	Target	Torus Field	Current	P_t	$\lambda/2$	Trigger Rate	Events
2.562 GeV	NH_3	-1500 A	0.5 nA	> 0	IN	1500 Hz	182.2 M
2.562 GeV	NH_3	-1500 A	0.5 nA	< 0	IN	1500 Hz	184.9 M
2.562 GeV	NH_3	-1930 A	0.5 nA	> 0	IN	1500 Hz	13.5 M
2.565 GeV	NH_3	+1500 A	1.6 nA	> 0	IN	1300 Hz	106.6 M
2.565 GeV	NH_3	+1500 A	1.6 nA	< 0	IN	1300 Hz	86.6 M
2.565 GeV	NH_3	+2250 A	2.0 nA	> 0	IN	1000 Hz	143.0 M
2.565 GeV	NH_3	+2250 A	2.0 nA	< 0	IN	1000 Hz	101.4 M
4.278 GeV	NH_3	-2250 A	2.0 nA	> 0	IN	2000 Hz	129.1 M
4.278 GeV	NH_3	-2250 A	2.0 nA	< 0	IN	2000 Hz	272.1 M
4.239 GeV	NH_3	+1930 A	2.5 nA	> 0	IN	1500 Hz	176.6 M
4.278 GeV	NH_3	+1930 A	3.2 nA	< 0	ININ	2000 Hz	88.1 M
4.068 GeV	NH_3	+1930 A	3.2 nA	> 0	ININ	2000 Hz	172.2 M
4.068 GeV	NH_3	+1930 A	3.2 nA	< 0	ININ	2000 Hz	187.7 M
4.278 GeV	NH_3	+2250 A	4.0 nA	> 0	IN	2000 Hz	35.8 M
4.278 GeV	NH_3	+2250 A	4.0 nA	> 0	ININ	2000 Hz	230.2 M
4.278 GeV	NH_3	+2250 A	4.0 nA	< 0	ININ	2000 Hz	175.4 M
2.562 GeV	ND_3	-1500 A	0.5 nA	> 0	IN	1500 Hz	153.9 M
2.494 GeV	ND_3	-1500 A	0.5 nA	< 0	IN	1500 Hz	83.2 M
2.565 GeV	ND_3	+2250 A	2.2 nA	> 0	IN	1500 Hz	338.8 M
2.565 GeV	ND_3	+2250 A	2.2 nA	< 0	IN	1500 Hz	23.5 M

Table 5.1: *Run summary for the EG1 run period. Each data set is characterized by the energy, toroidal field value, target type, beam current, target polarity, trigger rate and event number. In addition in the sixth column, the presence of the $\lambda/2$ plate used to reverse the laser polarization and therefore the electron helicity is reported.*

Channel Identification		
	$P_t > 0$	$P_t < 0$
Number of Triggers	143.0 M	101.4 M
Number of Reconstructed Events	53.4 M	33.6 M
Number of Events after Electron selection	25.6 M	16.3 M
Number of $e\pi^+$ *Coincidences*	1.88 M	1.21 M
Number of $e\pi^+n$ *Candidates*	0.245 M	0.406 M

Table 5.2: *Summary of the statistics for the 2.5 GeV data as a function of the selection cuts used for the channel identification.*

any of the problem mentioned above may be a source of false asymmetries.
As mentioned in section 5.2, the present analysis has been performed for the data at 2.5 GeV and torus current +2250A. The available data have been therefore filtered applying precise quality criteria before proceeding with the extraction of the asymmetries. Several quantities have been monitored for each run. These quantities are:

- number of inclusive electrons;
- number of elastic electrons;
- number of inelastic electrons;
- number of ep coincidences;
- number of eπ^+ coincidences;
- number of $e\pi^+n$ events;
- average number of particles per event;
- vertex position;
- vertex distribution width;
- dead time;

As mentioned in section 4.2.2, in addition to this quantities, other parameters were monitored during the reconstruction process. These include the average number of photoelectrons in the six sectors of the Cerenkov Counter, the tracking residuals in the three regions of drift chambers, the average energy released by the primary electron in the electromagnetic calorimeters. To be able to compare the listed parameters for different runs, all the rates have been normalized to the accumulated charge for that run. The charge is measured during the data taking by a Faraday Cup and the corresponding values are recorded every 10 s in the data stream. These quantities are also corrected for the live time of the acquisition. The charge accumulated at the Faraday Cup is integrated with a conversion factor of 10 counts/nA. This implies that for a one-hour run at 2 nA, i.e. the typical current at 2.5GeV, the charge measurement has an accuracy of 1 part in 10^5.
The electrons, pions, and proton rates have been defined using the particle identification

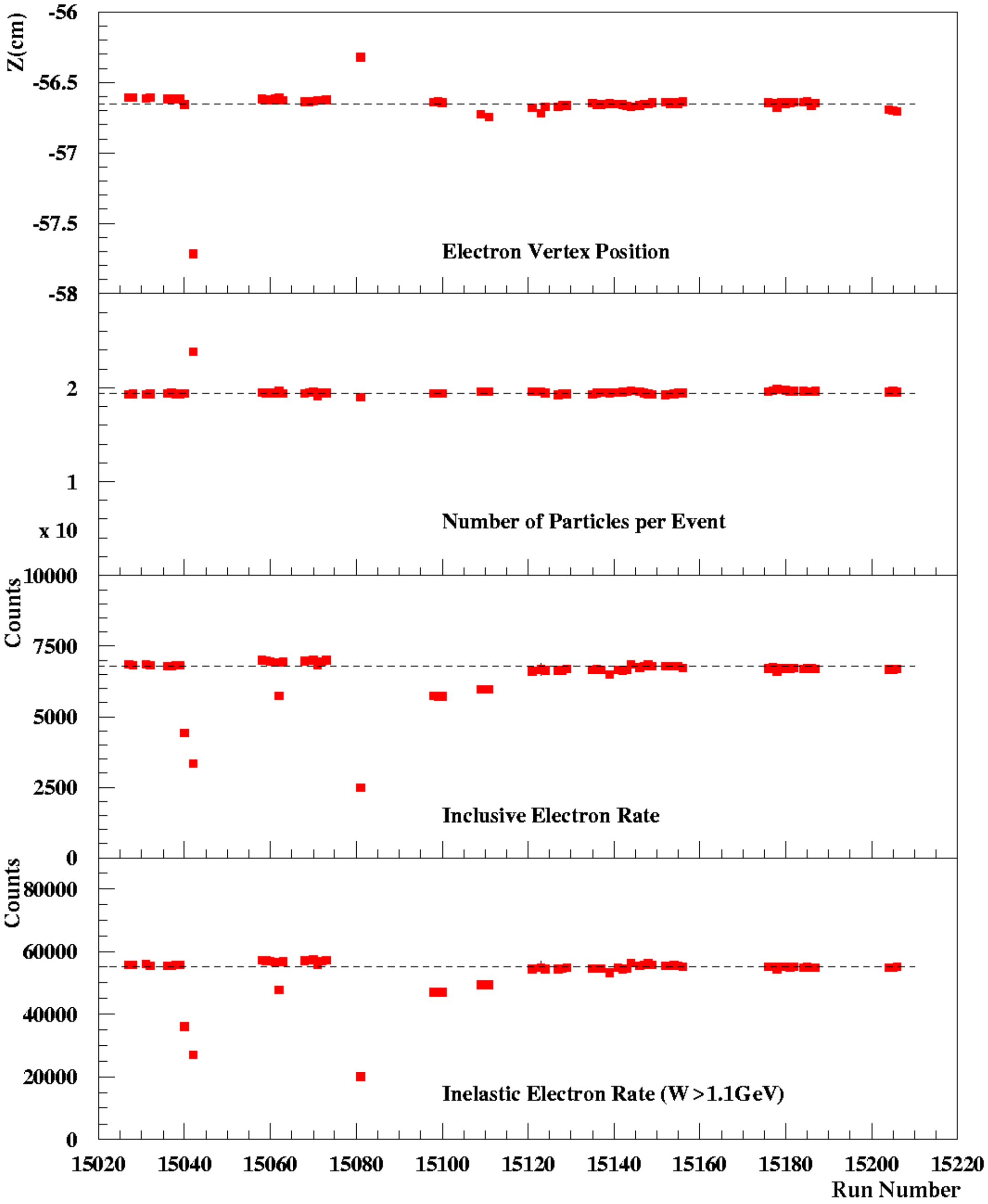

Figure 5.2: *Sample of the quality check developed for the 2.5 GeV data. The four plots show as a function of the run number the reconstructed z coordinate of the vertex, the average number of detected particles per event, the inclusive electron rate and the inelastic electron rate, both normalized to the Faraday Cup.*

cuts defined in chapter 4. The fiducial region introduced for electron and hadrons have been included to reject the low efficiency region of the detector whose response may be less stable in time.
All the above parameters have been also calculated for each of the CLAS sectors separately. In this case the fiducial regions were modified to be able to compare the absolute rates of the different sectors; for this reason the same number of time of flight paddles and Cerenkov strips were rejected in each sector.
A sample of these quality checks is shown in figure 5.2.
The first result of this analysis is the identification of abnormal runs in which one of the monitored parameters was clearly far from the observed average value. For example run 15040 (see figure 5.2) shows very low electron rates in three of the six sector. This problem is related to a malfunctioning in the high voltage system of the electromagnetic calorimeters. For this reason the trigger rate and therefore the electron detection efficiency are almost zero in those sectors, while hadrons show normal rates. Obviously all these runs were excluded from the analysis.
This study has also demonstrated that the six sectors have different rates in particular for electrons emitted at low angles. For inelastic events, that are the basis of this analysis, the difference is smaller and can be estimated to be of order of few percent ($\pm 3\%$). The total rates (summed over the six sector) are instead very stable with variations of $\approx 1.5\%$.
The impact of these variations on the final result has been studied and the conclusions are discussed in section 6.3.

5.4 Analysis Procedure

In this section I will describe the procedure used to extract the final asymmetry from the data.
As mentioned in section 1.4.1, the cross section for pion electroproduction with polarized beam and target can be schematically written as

$$\sigma_v = \sigma_0 + P_e\sigma_e + P_t\sigma_t - P_eP_t\sigma_{et}. \tag{5.1}$$

The three quantities, σ_e, σ_t, σ_{et} can be extracted from double spin measurements. In fact using different sets of data with the two opposite beam helicities and the two opposite target helicities it is possible to separate, in a complete model independent way, the different components of the cross section. The spectra recorded with the four combinations of proton and electron polarization can be in fact expressed as

$$\begin{aligned}
N_{\uparrow\uparrow} &= D_1\left[\sigma_0 + P_e^a\sigma_e + P_t^a\sigma_t - P_e^aP_t^a\sigma_{et}\right] \\
N_{\downarrow\uparrow} &= D_2\left[\sigma_0 - P_e^a\sigma_e + P_t^a\sigma_t + P_e^aP_t^a\sigma_{et}\right] \\
N_{\uparrow\downarrow} &= D_3\left[\sigma_0 + P_e^b\sigma_e - P_t^b\sigma_t + P_e^bP_t^b\sigma_{et}\right] \\
N_{\downarrow\downarrow} &= D_4\left[\sigma_0 - P_e^b\sigma_e - P_t^b\sigma_t - P_e^bP_t^b\sigma_{et}\right]
\end{aligned} \tag{5.2}$$

where $N_{\uparrow\downarrow}$ for example represents the number of events with electron spin ($\uparrow$) parallel to the beam direction (positive helicity) and proton spin ($\downarrow$) antiparallel to the electron

beam. The four parameters D_1, D_2, D_3, D_4 correspond to the total luminosity in each configuration. Since the target is the same for each of the four measurements the luminosities can only differ for the accumulated charge in each setting that can in general have different values. The factors P_i^a and P_i^b represent the beam and target polarization for the sets of runs a and b, characterized respectively by positive and negative target polarization. The choice of these polarization parameters is based on the fact that, while the electron polarization is flipped every second, the target polarization was inverted only twice during the data taking of the full 2.5 GeV data set. For this reason while data sets with the same target polarization but opposite electron polarization will share the same polarization, sets with opposite target polarization may have different values for both the electron and proton polarization.
To extract the spin-dependent cross sections, is therefore necessary to determine the 8 parameters D_1, D_2, D_3, D_4, P_e^a, P_t^a, P_e^b, P_t^b. We can observe that the charge factors D_1, D_2 are related to the accumulated charge recorded during the same set of runs but for the two electron helicities. These quantities are in principle equal except for a possible helicity-related charge asymmetry in the beam. The presence of such asymmetry has been observed in the CEBAF beam and as been measured to be approximately -0.3% as discussed in section 5.5. The factors D_1, D_2 differ therefore only for this small effect. The same is valid for D_3 and D_4. Nevertheless correcting for this false asymmetry, for example redefining

$$\begin{aligned} N_{\uparrow\uparrow} &\to \frac{D_2}{D_1} N_{\uparrow\uparrow} \\ N_{\downarrow\downarrow} &\to \frac{D_3}{D_4} N_{\downarrow\downarrow}, \end{aligned} \tag{5.3}$$

it's possible to reduce the charge factors to only two: $D_+ = D_2$, $D_- = D_3$. In addition it's convenient to normalize the different polarization to a chosen one, for example P_e^a and P_t^a, introducing the factors

$$\alpha_e = \frac{P_e^a}{P_e^b} \qquad \alpha_t = \frac{P_t^a}{P_t^b} \qquad \alpha_{et} = \frac{P_e^a P_t^a}{P_e^b P_t^b}.$$

With this approach the number of absolute parameters that must be derived separately is reduced to 4 only, while most of these normalization factors parameters, including α_{et}, can be extracted directly from the data.
For example in inclusive scattering due to the absence of single spin asymmetries, the previous formulas are simplified and become

$$\begin{aligned} N_{\uparrow\uparrow} &= D_1 \left[\sigma_0 - P_e^a P_t^a \sigma_{et}\right] \\ N_{\downarrow\uparrow} &= D_2 \left[\sigma_0 + P_e^a P_t^a \sigma_{et}\right] \\ N_{\uparrow\downarrow} &= D_3 \left[\sigma_0 + P_e^b P_t^b \sigma_{et}\right] \\ N_{\downarrow\downarrow} &= D_4 \left[\sigma_0 - P_e^b P_t^b \sigma_{et}\right]. \end{aligned} \tag{5.4}$$

From these expressions, just requiring the two cross sections σ_0 and σ_{et} to be equal in the data sets with opposite target polarization, it is possible to obtain

$$d = \frac{D_+}{D_-} = \frac{N_{\uparrow\uparrow}\frac{D_2}{D_1} + N_{\downarrow\uparrow}}{N_{\uparrow\downarrow} + \frac{D_3}{D_4} N_{\downarrow\downarrow}} \qquad \alpha_{et} = \frac{1}{d} \frac{N_{\uparrow\uparrow}\frac{D_2}{D_1} - N_{\downarrow\uparrow}}{\frac{D_3}{D_4} N_{\downarrow\downarrow} - N_{\uparrow\downarrow}}.$$

The other parameter α_e is simply obtained from the Moeller measurement while α_t is not independent since is given by the ratio α_{et}/α_e.
Based on this calculation and introducing

$$\begin{aligned}
\bar{N}_{\uparrow\uparrow} &= N_{\uparrow\uparrow}\frac{D_2}{D_1} \\
\bar{N}_{\uparrow\downarrow} &= N_{\uparrow\downarrow} \\
\bar{N}_{\downarrow\uparrow} &= N_{\downarrow\uparrow}d \\
\bar{N}_{\downarrow\downarrow} &= N_{\downarrow\downarrow}\frac{D_3}{D_4}d
\end{aligned} \tag{5.5}$$

it's finally possible to extract the three asymmetry

$$\begin{aligned}
A_e &= \frac{\sigma_e}{\sigma_0} = \frac{1}{P_e^a}\frac{(\bar{N}_{\uparrow\uparrow} - \bar{N}_{\downarrow\uparrow}) + \alpha_{et}\,(\bar{N}_{\uparrow\downarrow} - \bar{N}_{\downarrow\downarrow})}{(\bar{N}_{\uparrow\uparrow} + \bar{N}_{\downarrow\uparrow}) + \alpha_t\,(\bar{N}_{\uparrow\downarrow} + \bar{N}_{\downarrow\downarrow})} \\
A_t &= \frac{\sigma_t}{\sigma_0} = \frac{1}{fP_t^b}\frac{(\bar{N}_{\uparrow\uparrow} + \bar{N}_{\downarrow\uparrow}) - (\bar{N}_{\uparrow\downarrow} + \bar{N}_{\downarrow\downarrow})}{(\bar{N}_{\uparrow\uparrow} + \bar{N}_{\downarrow\uparrow}) + \alpha_t\,(\bar{N}_{\uparrow\downarrow} + \bar{N}_{\downarrow\downarrow})} \\
A_{et} &= \frac{\sigma_{et}}{\sigma_0} = \frac{1}{fP_e^aP_t^b}\frac{(\bar{N}_{\downarrow\uparrow} - \bar{N}_{\uparrow\uparrow}) + \alpha_e\,(\bar{N}_{\uparrow\downarrow} - \bar{N}_{\downarrow\downarrow})}{(\bar{N}_{\uparrow\uparrow} + \bar{N}_{\downarrow\uparrow}) + \alpha_t\,(\bar{N}_{\uparrow\downarrow} + \bar{N}_{\downarrow\downarrow})}
\end{aligned} \tag{5.6}$$

where f indicates the dilution factor, i.e. the percentage of events that are produced by the hydrogen nuclei in the ammonia target.
As shown by the previous formula, the knowledge of the polarization and dilution factor is a necessary requirement for the full extraction of the double spin asymmetry. For this reason a particular care was dedicated to the evaluation of these quantities and the procedure and results are discussed in section 5.6 and 5.7.

5.5 Beam Charge Asymmetry

The control of the systematic error is a fundamental issue in asymmetry measurements. In particular it is important to identify and eliminate or correct any source of false asymmetry. In the present case one source of false asymmetry was found in relation to a systematic difference in the electron rate for the two opposite electron helicities.
One contribution to this false asymmetry is related to the presence of broken sequences of helicity states. The helicity pattern of the electron beam is in fact formed by pairs of electron buckets with opposite helicity whose order is chosen in a pseudo-random way (see figure 5.3). The helicity flip rate is 1Hz. During the acquisition process, the sequence can be interrupted by the DAQ, due to dead time problems, leaving unpaired helicity states. This phenomenon introduces of course an asymmetry in the number of electron with the two helicities. Nevertheless this effect can be removed simply requiring to have an uninterrupted sequence of helicity states. This is perform by applying a pre-filtering process to the data, in which the sequence of helicity states recorded in the data stream is compared with the information received directly from the CEBAF injector to identify the missing states and therefore the breaks in the helicity sequence.
After the rejection of the unpaired helicity states a charge asymmetry is anyhow still

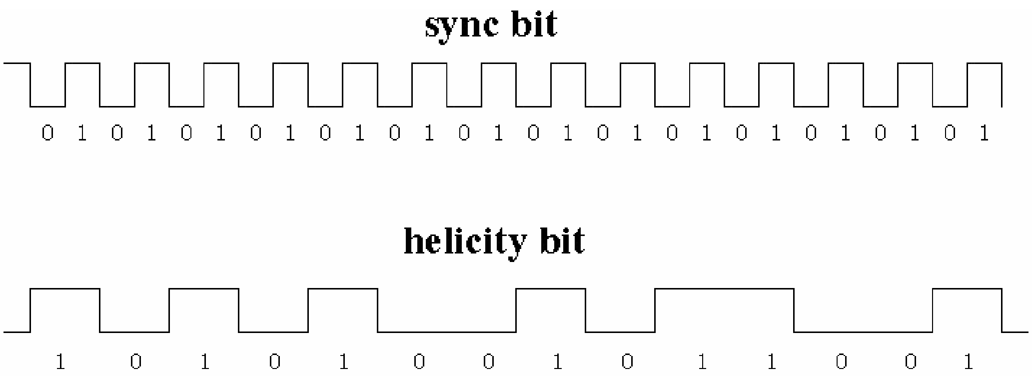

Figure 5.3: *Schematic of the helicity structure of the beam. The helicity is flipped at a frequency of 1 Hz with a pseudo-random sequence. A one-bit signal from the accelerator injector provides the helicity information. A 'sync' signal with double frequency is generated simultaneously and identifies the time of the helicity flip. This in fact occurs on the falling edge of the 'sync' signal.*

observable. This effect is detectable by looking for example at the inclusive asymmetry in carbon data: the carbon target is obviously an unpolarized target and therefore any difference in the inclusive spectrum for opposite electron helicity can only be due to a false asymmetry. As shown by figure 5.4 the observed asymmetry in the inclusive spectrum is of the order of $\sim -0.3\%$.
A similar effect can be seen looking at the inclusive asymmetry in the NH_3 data in the quasi-elastic region: in this W range the observed events can only come from the nuclei contained in this target (nitrogen+target windows+helium), i.e. an almost completely unpolarized mixture. Therefore this region should give a negligible asymmetry while a non-zero difference between the W spectra for the two helicities has been observed. The observed asymmetry is again compatible with a value of $\sim -0.3\%$ even if the statistical uncertainty is much larger that in the former case.
This evidence is an indication of a charge asymmetry in the beam current.
The solution to this problem is obviously to measure the accumulated charge for each helicity separately and correct for this false asymmetry. This measure is provided by the Faraday Cup that, for this purpose, is read synchronously with the helicity flip. The accumulated charge value corresponding to each helicity states is stored into a scaler memory and every 10 s the information for the previous 10 helicity states is sent to the data stream. The scaler information need then to be correlated with the helicity recorded on an event-by-event basis. For this purpose I developed a code to match each electron bucket with its appropriate Faraday Cup charge and to pair up the helicity states in complete pairs sequences. In the present analysis only events belonging to this corrected sequences were used.
A systematic study of the charge asymmetry was done for each energy and torus setting used in the '98 run. Carbon runs were used for this study since in that case the inclusive asymmetry can be used to check the result obtained for the charge asymmetry. Figure 5.4 shows in fact the observed asymmetry in inclusive scattering before (top plot) and after the charge-asymmetry correction. Each point corresponds to a sample of 1 M triggers and the different sections of the two plot are relative to different beam currents. The conclusion of this test is that the evaluation of the charge asymmetry by the Faraday

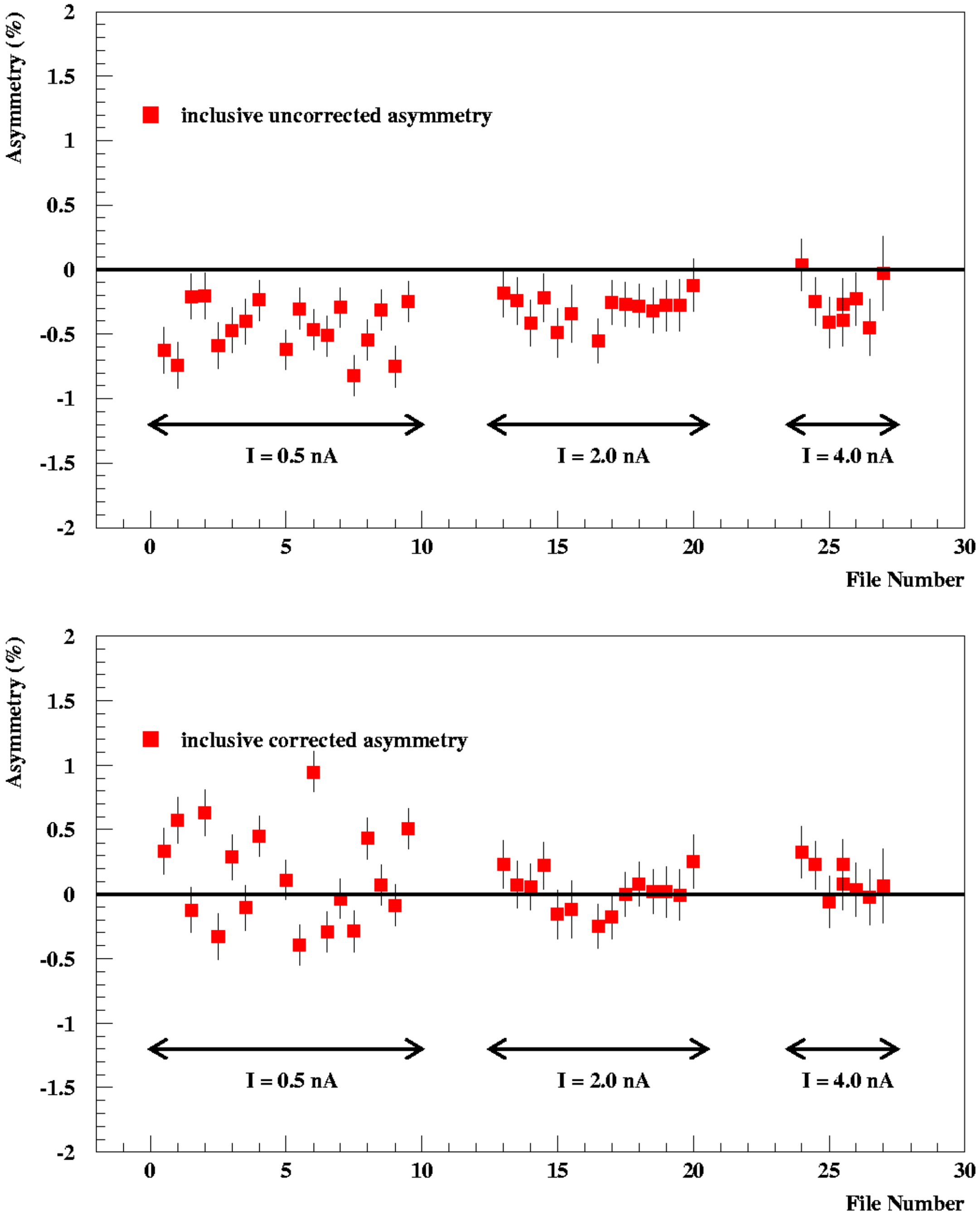

Figure 5.4: *Inclusive asymmetry on carbon target before (top plot) and after (bottom plot) the beam charge asymmetry correction for different data files. The correction clearly bring the inclusive asymmetry to the expected zero value. As mentioned before only for the lowest current data (I=0.5 nA) the correction does not converge yet.*

Cup readout produces the desired effect of canceling the false asymmetry observed in the data for all the settings except for the very low current.

5.5.1 Accuracy of the Beam Charge-Asymmetry Measure

The charge asymmetry for a data run is estimated as the integral of the Faraday Cup charge for the two electron helicities. The integral over several electron buckets contributes in reducing the final uncertainty. The single Faraday Cup measurement has an intrinsic error of ± 1 count. This implies that the measurement of the accumulated charge for one helicity state with a beam current of 2nA is equal to (20 ± 1), i.e. a measurement affected by a 5% intrinsic error. This uncertainty is clearly to high to allow a measurement of false asymmetry for each helicity pair. Nevertheless the integral of the accumulated charge over several helicity states has a smaller error thanks to the mechanism that determines the readout for each electron bucket. In fact while the Faraday Cup converts the charge to pulses or counts, the single-state charge measurement is obtained counting the number of pulses received during the 1 s time with fixed helicity. The number of counts for i-th state is given by

$$N_i = int[10(R_{i-1} + D_i)] \tag{5.7}$$

where D_i is the true charge in nC accumulated for that state and R_{i-1} is the charge remainder from the previous state. This remainder is a consequence of the integer conversion operated by the Faraday Cup and is defined as

$$R_{i-1} = D_{i-1} - \frac{N_{i-1}}{10} \tag{5.8}$$

The integrated charges for the two helicity states are then given by

$$\begin{aligned} D_{h+} &= \sum_{h_i>0} int[10(R_{i-1} + D_i)] \\ D_{h-} &= \sum_{h_i<0} int[10(R_{i-1} + D_i)] \end{aligned} \tag{5.9}$$

and the relative errors are

$$\begin{aligned} \Delta D_{h+} &= \sum_{h_i>0} \left\{ D_i - \frac{int[10(R_{i-1} + D_i)]}{10} \right\} \\ \Delta D_{h-} &= \sum_{h_i<0} \left\{ D_i - \frac{int[10(R_{i-1} + D_i)]}{10} \right\} \end{aligned} \tag{5.10}$$

where R_{i-1} is recursively defined as $R_{i-1} = int\left[\sum_{j=1}^{i-1} 10D_j\right]$. The above formulas indicate clearly that each single charge measure is in reality correlated to the previously accumulated charge, and this correlation is responsible of a reduction of the overall uncertainty in the charge integrals defined in eq. 5.9
The exact evaluation of the charge asymmetry uncertainty can be obtained computing the sum of the series in eq. 5.10. These are complicated series and to overcome this problem and give an estimate of this uncertainty two separate methods were used.

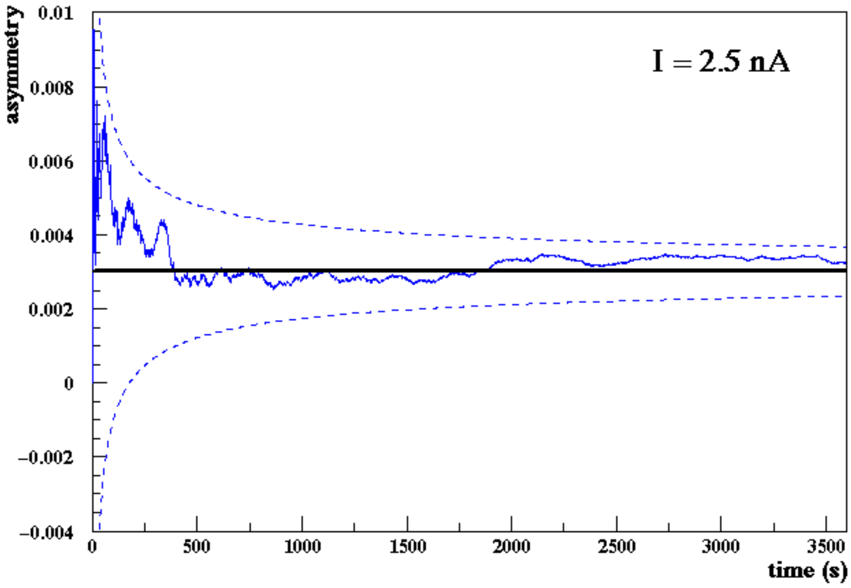

Figure 5.5: *Simulation of the beam charge asymmetry measurement operated by the Faraday Cup. The measured value, as explained in the text, tends to converge to the true value indicated by the thick solid line. The two dashed lines represent the limits on the measurement uncertainty estimated with the statistical approach.*

The first method uses a simple statistical approach in the assumption that each pair of helicity states is completely uncorrelated from the others. This is an extreme case that may describe the real condition if the current fluctuations are so high to destroy the correlation of the single Faraday Cup measurement. Anyhow this method is useful since it establishes an upper limit to the error on the dose integral. The correlations in fact tend to reduce this error. In this assumption the error on the charge difference for a single helicity pair with charges D_+ and D_- would be

$$\Delta = \frac{N_+ - N_-}{10} - (D_+ - D_-) = \pm[(R_0 - R_+) - (R_+ - R_-)] = \pm[R_0 - 2R_+ - R_-] \quad (5.11)$$

where R_0 is the remainder charge of the states before that chosen pair and R_+ and R_- are the remainder of the positive-helicity and negative-helicity states. The $\pm$ sign depends on the order of the helicity states in the pairs.

The assumption of completely uncorrelated pairs implies that the remainder R_0 will be randomly distributed between 0 and 1/10 nC. As a consequence it is possible to demonstrate that the error Δ for the single pairs has average 0 and maximum standard deviation of $\sqrt{2}/10$ nC (the exact standard deviation depends, in these assumptions, on the value of the beam current for the two helicities). Consequently, the error on the charge difference integrated over n pairs is $\sqrt{2n}/10$ and the corresponding error on the charge asymmmetry is

$$\sigma(A_d) \approx \frac{\sqrt{2n}}{10(D_+ + D_-)} = \frac{\sqrt{2}}{20\sqrt{nI}} \quad (5.12)$$

where I is the beam current.

This method is valid only when the numbers of pairs is high enough to use a statistical

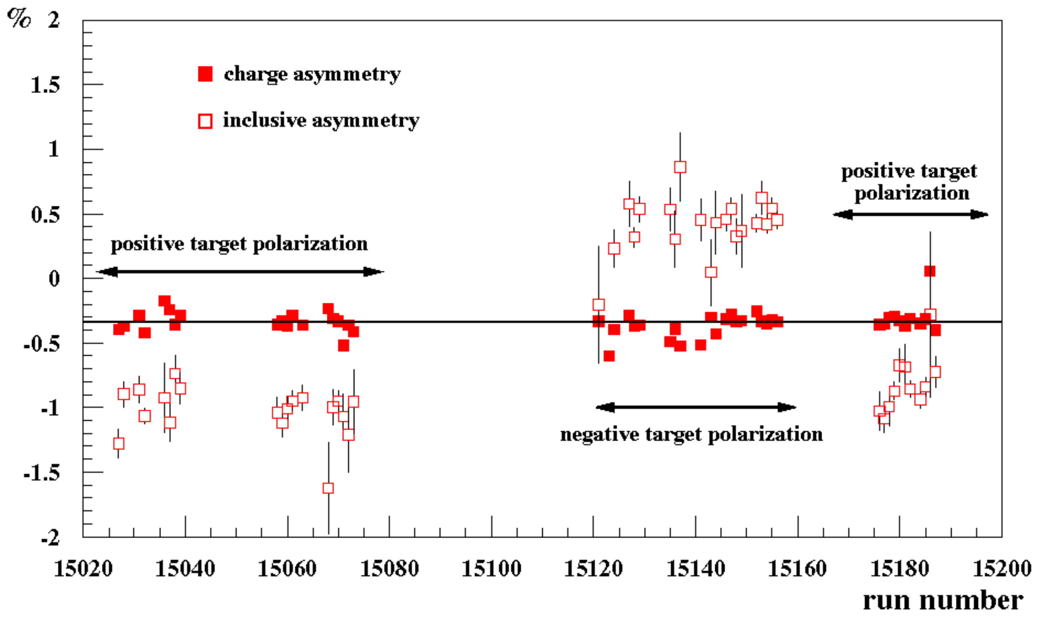

Figure 5.6: *Beam charge asymmetry versus run number for the 2.5 GeV data. The filled squares represent the charge asymmetry while the empty squares are the uncorrected electron inclusive asymmetry integrated in Q^2 and W. As shown by the plot, the charge asymmetry is stable with an average value of $\sim -0.34\%$. The corrected asymmetry is given by the difference between the uncorrected one and the charge asymmetry: its behavior is therefore consistent with flip of the target polarity occurred at run 15098 and 15176.*

approach.
The other method consist in the numerical computation of the sum of the series in eq. 5.9. This has been done for several different current and assuming different values for the charge asymmetry. An example of the result is given in figure 5.5. This approach represents the other extreme possibility since in this case the beam current for the two helicity is assumed to be constant and therefore the helicity pairs are fully correlated.
The result of this calculation shows that, for charge asymmetries close to the -0.3% observed in the data, the final error on the charge asymmetries is always less than the error derived in the full statistical approach.
These two different approaches have been used to estimate the charge-asymmetry uncertainty to be included in the evaluation of the systematic errors discussed in chapter 6.

5.5.2 Beam Charge Asymmetry for the 2.5 GeV Data

The charge asymmetry for the 2.5 GeV data used in this analysis was calculated on a run by run basis and the results are shown in figure 5.6. In the plot the filled squares represent the charge asymmetry as measured from the Faraday Cup while the empty squares represent the inclusive uncorrected asymmetry (integrated over W and Q^2). The inclusive asymmetry is determined by the physics governing the process and can vary only in relation to the beam and target polarizations. The correct asymmetry is given in first approximation by the sum of the uncorrected and charge asymmetry. In fact assuming to calculate the asymmetry from two spectra with N_+ and N_- counts and D_+ and D_- accumulated charges, the corrected asymmetry is defined as

$$A_c = \frac{\frac{N_+}{D_+} - \frac{N_-}{D_-}}{\frac{N_+}{D_+} + \frac{N_-}{D_-}} = \frac{1 - \frac{N_-}{N_+}\frac{D_+}{D_-}}{1 + \frac{N_-}{N_+}\frac{D_+}{D_-}} = \frac{A_u - A_d}{1 + A_u A_d} \approx A_u - A_d \tag{5.13}$$

where $A_u = (N_+ - N_-)/(N_+ + N_-)$ is the uncorrected asymmetry and $A_d = (D_+ - D_-)/(D_+ + D_-)$ is the charge asymmetry. Therefore for stable running condition (stable beam and target polarization etc.) the difference $A_u - A_d$ should be constant as shown by the plot.
The average charge asymmetry was found to be $\sim -0.336\%$ as already observed in the carbon data. The error on this measurement was estimated using the two methods described in the previous section and the result was an upper limit on the systematic error of this evaluation of $\pm 0.006\%$.

Q^2 (GeV^2/c^2)	$A_{elastic}(R(Q^2) = 1)$	$A_{elastic}$(ref.[71])
0.3	0.139	0.139
0.5	0.213	0.214
1.0	0.380	0.384
1.6	0.564	0.567
2.0	0.678	0.679

Table 5.3: *Predicted elastic asymmetry for different Q^2 values. The two values are both obtained in the EG1 kinematics but with different parametrizations of the ratio of the electric and magnetic form factors of the proton.*

5.6 Evaluation of the Beam and Target Polarization from Elastic Scattering

As shown by the expression for the asymmetries derived in section 5.4, a precise knowledge of the target and beam polarization is necessary to obtain an accurate measurement of the spin asymmetries. The polarization factor may in fact be one of the dominant source of systematic error in this kind of analysis.
During the experiment the beam polarization was measured using a Moeller polarimeter with an accuracy of few %. The target polarization was instead monitored by a NMR system. As described in chapter 3, the NMR sensors are located on the outside of the target cell walls, and therefore are mainly sensitive to the polarization of the outer part of the target material. In addition the rastering area of the electron beam was found to be limited to a small region close to the target center reducing the sensitivity of the NMR to the polarization of the 'active' material. Consequently, one of the main issue in this analysis has been the definition of an independent method to measure the beam and target polarization with the maximum accuracy.

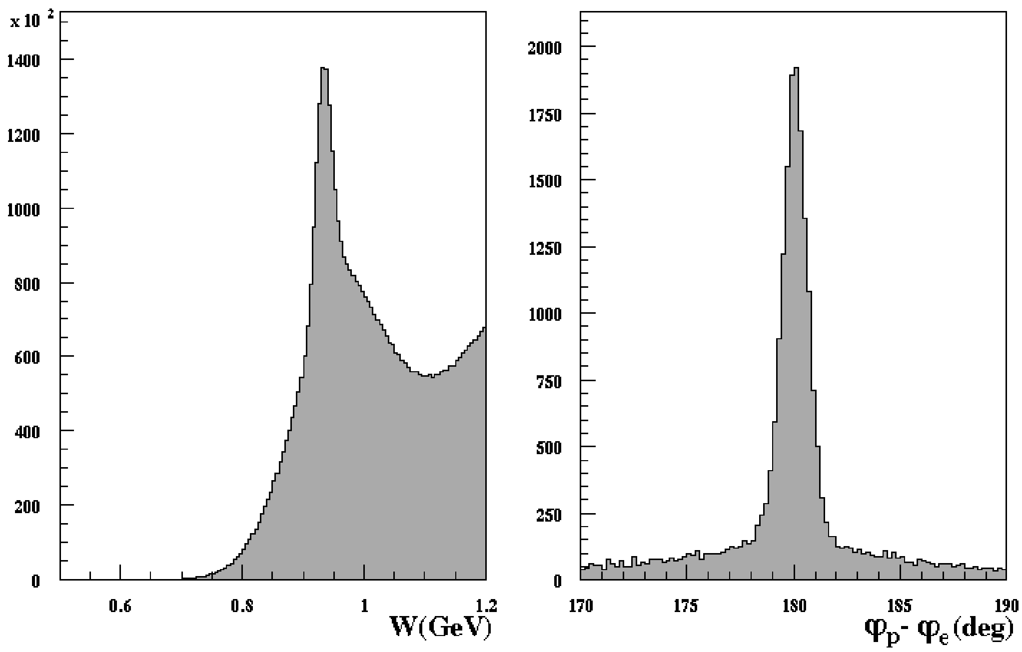

Figure 5.7: *W and ϕ distribution for elastic events. The left plot shows the W spectrum obtained detecting the scattered electron. The clear elastic peak is superimposed on the nitrogen quasielastic peak. The right plot shows the angular correlation between the electron and proton azimuthal angle. The nitrogen contribution gives the smooth background below the peak.*

The chosen method relies on the measurement of the elastic asymmetry from which it is possible to extract the product of the target and beam polarization P_eP_t. This procedure is feasible thanks to the CLAS capabilities to simultaneously measure all the reaction channels including elastic scattering.
The elastic asymmetry serves to this purpose since its general expression is predicted by theory and depend only on the ratio of the electric and magnetic form factors

$$R(Q^2) = \mu_p \frac{G_E(Q^2)}{G_M(Q^2)} \tag{5.14}$$

The elastic asymmetry can in fact be written as

$$A_{elastic} = \frac{1}{\sqrt{2}} \frac{-\cos\psi\sqrt{1-\epsilon^2} + \sin\psi\cos\varphi\sqrt{2\epsilon(1-\epsilon)}\left(\frac{Q^2}{4m^2}\right)^{-1/2} R(Q^2)}{1+\epsilon\left(\frac{Q^2}{4m^2}\right)^{-1} R^2(Q^2)} \tag{5.15}$$

where the angles ψ and φ describe the direction of the target spin in relation to the virtual photon. In the EG1 kinematics the angle ψ corresponds to angle between the virtual photon and the beam axis while the angle φ is equal to 0. The ratio $R(Q^2)$ was measured in several experiments with different results and a noticeable deviation from unity was observed in a recent measurement in Hall A at Jefferson Lab [71]. However, in the kinematical conditions of the present experiment where the target is polarized along the electron beam, the elastic asymmetry is only weakly dependent from the ratio

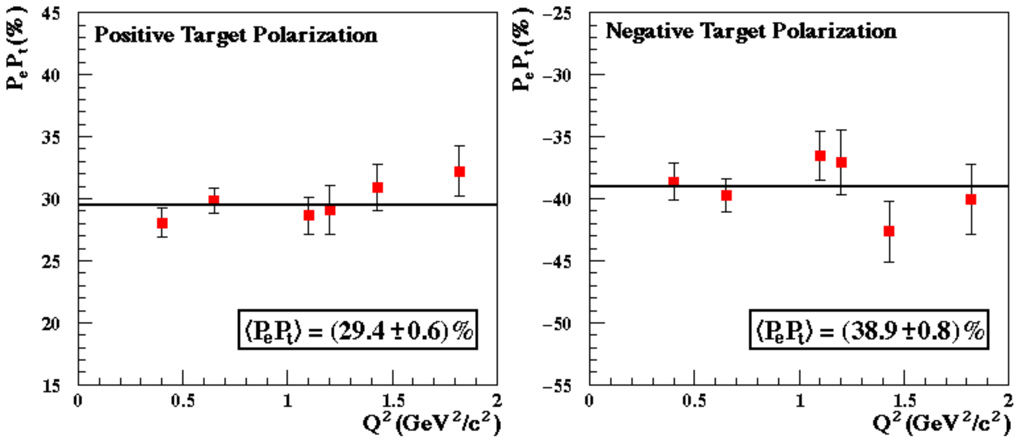

Figure 5.8: *Product of the beam and target polarization for positive target-polarization and negative target-polarization runs. In each set the product was evaluated in six different Q^2 bins using the elastic asymmetry: the first three are the results of the inclusive analysis while the last three are obtained from the exclusive one.*

$R(Q^2)$. An example is given in table 5.3, where the $A_{elastic}$ at 2.5 GeV is computed for $R(Q^2) = 1$ and for $R(Q^2)$ as obtained from an interpolation of the data in reference [71], showing an overall difference lower than 1%. The elastic asymmetry reported above is calculated for 100 % electron and proton polarization. By comparing the predicted asymmetry with the asymmetry observed in the data is therefore possible to extract the product of the beam and the target polarization. Because of the importance of this quantity for the final result of this analysis, the extraction of the elastic asymmetry from the data was performed with two different approaches. In the first case elastic events were selected detecting only the scattered electron and using the correlation between the electron momentum and angle to separate those events from inelastic scattering. In the second approach both electron and proton in the final state were detected and their angular correlation was exploited to separated elastic events.
The first method has clearly the advantage of a higher statistics in comparison to the fully exclusive approach. Nevertheless, since the target is composed by ammonia molecules, an additional difficulty is introduced by the overlap of the elastic and quasi-elastic events. In the first case the elastic peak is in fact completely superimposed over the quasi-elastic nitrogen contribution as shown in figure 5.7. In the second the strict azimuthal correlation of the elastic events contributes to obtaining a better discrimination of hydrogen and nitrogen events (see figure 5.7).
However in both cases the nitrogen background needs to be subtracted. This was performed by estimating the nitrogen contribution based on carbon data. The ^{12}C spectra, both in the inclusive and exclusive analysis, were fitted to a smoothed curve to reduce the statistical fluctuations and normalized to the nitrogen spectra. In the inclusive analysis the normalization factor was obtained comparing the quasielastic tail for the W spectra between 0.6 and 0.85 GeV^2/c^2. In this region in fact no hydrogen contribution is present since the elastic peak width is approximately 15 MeV and the nuclear-correlation effects are still small. A similar procedure was applied also for the exclusive analysis. In this

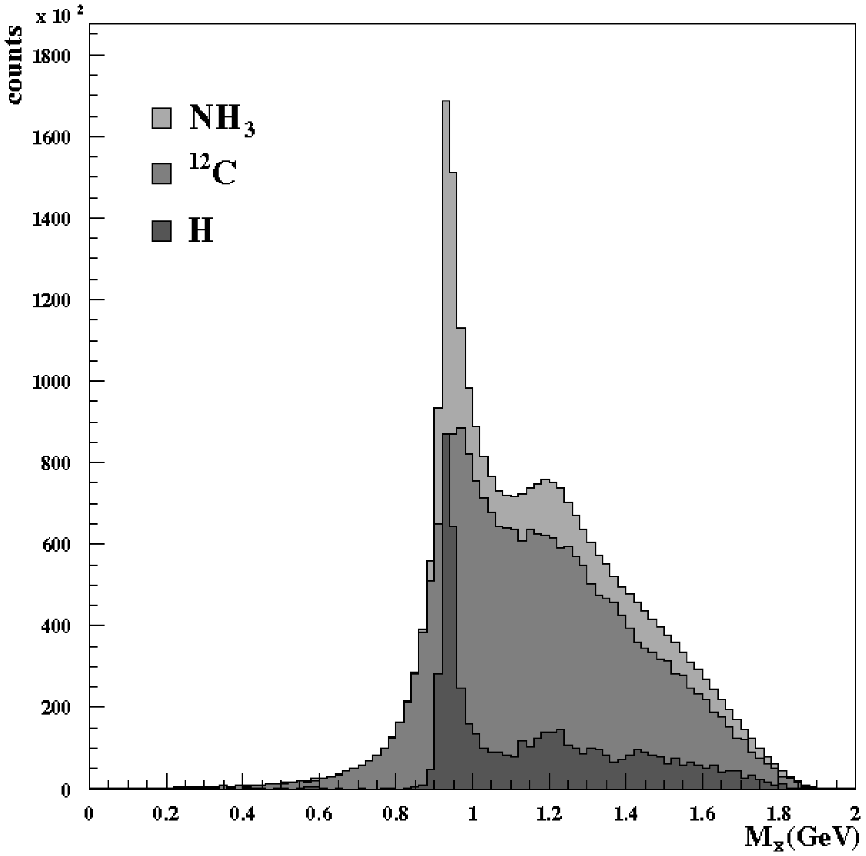

Figure 5.9: *$e\pi^+$ missing mass spectra for NH_3 (light grey) and ^{12}C (medium grey) targets. The dark histogram represents the free hydrogen contribution obtained by subtracting the ammonia and carbon spectra.*

case the normalization was obtained on the sides of the peak shown in the right plot of figure 5.7.
After the separation of the elastic events the asymmetry was calculated in both methods for different Q^2 bins and the product of the beam and target polarization was obtained as

$$P_e P_t = \frac{A_{exp}}{A_{elastic}} \tag{5.16}$$

The main reason for using two separate methods is the identification of systematic effect. The two analysis are in fact completely indepedent not only for the event selection but also for the nitrogen subtraction and the comparison of their results is therefore an important tool to evaluate the systematic error.
This procedure was applied to the 2.5 GeV data set: the polarization was evaluated for four sets of runs and the results are shown in figure 5.8. The six data point have been obtained for different Q^2 values; the first three are the result of the inclusive analysis while the last three have been obtained form the exclusive one. The final error is given as the weighted average of the single error measurement. This estimate of the polarization introduces therefore relative error of $\sim 2.5\%$ on the final asymmetry.

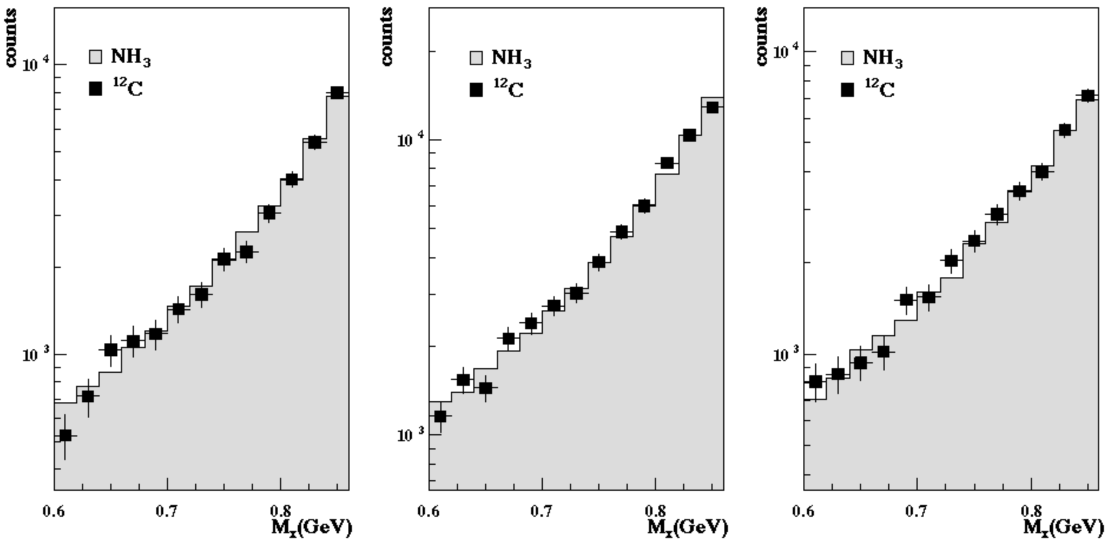

Figure 5.10: *Comparison of the NH_3 (grey histogram) and ^{12}C (points) missing mass spectra for $M_X < 0.85 GeV$ in three Q^2 bins.*

5.7 Dilution Factor

The dilution factor is defined as the ratio between the hydrogen and the full NH_3 contribution to the cross section:

$$f = \frac{3H}{NH_3} \tag{5.17}$$

The dilution factor accounts for the effect of nitrogen contribution to the measured asymmetry. The ^{15}N nucleus is almost unpolarized and therefore it does not produce any sizeable effect in the spin terms of the cross sections that depend from the target polarization. However it gives a significant contribution to the electron spin term and to the unpolarized cross section. The latter determines the denominator of the asymmetry calculation that as a consequence is 'diluted' by the nitrogen.

For the present analysis, ^{12}C data have been used to estimate the ^{15}N contribution and the dilution factor. This procedure is feasible since π^+ electroproduction is mainly sensitive to the protons inside the nucleus. Thus the ^{15}N spectrum can be evaluated from the ^{12}C spectrum by correcting for the different number of protons, i.e. 7/6.

Q^2 (GeV^2/c^2)	*Normalization Constant c*
$0.3 < Q^2 < 0.5$	(15.63 ± 0.33)
$0.5 < Q^2 < 0.9$	(15.34 ± 0.24)
$0.9 < Q^2 < 1.5$	(15.28 ± 0.32)
all Q^2	(15.38 ± 0.17)

Table 5.4: *Normalization constant extracted from the comparison of the carbon and nitrogen missing mass spectra below the neutron peak. The reported values show that at this level of accuracy no Q^2 dependence affects the behavior of the normalization constant.*

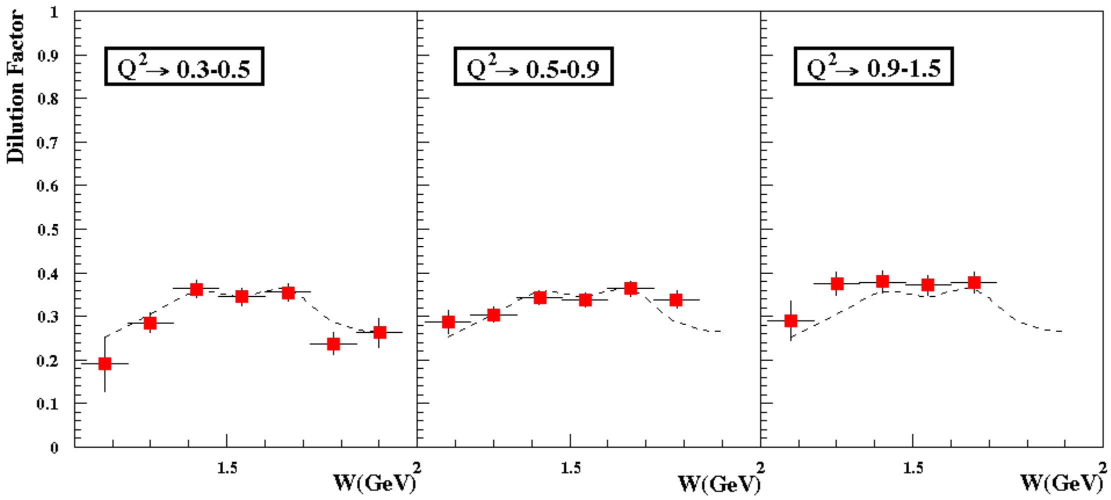

Figure 5.11: *Comparison of the dilution factor for three different Q^2 bins as a function of W. The dashed line represent the average dilution factor obtained as a sum over all Q^2. The plots shows that the dilution factor does not have any evident dependence from Q^2.*

Furthermore, since the channel selection is performed using the missing mass technique, only the quasi-free nucleon of the ^{15}N are included in the event sample. This implies that the nuclear effects, which may occur in the two nuclei, affect the selected events only in a negligible way. The exact procedure used for the dilution factor evaluation can be subdivided in two steps. First, the carbon data were normalized to the NH_3 data comparing the missing mass spectra below the neutron peak ($W < 0.85$ GeV). This region is free from the hydrogen contribution and therefore it is simply determined by the nuclear part. This normalization procedure compensates also for the poor knowledge of the NH_3 target thickness. The normalization constant c has been extracted separately for three different Q^2 intervals and the values are reported in table 5.4. These numbers show that the normalization factor does not have any evident dependence from Q^2, indicating that, at this accuracy level, the two nuclei have a very similar behavior. For this reason a single normalization constant was finally used in the analysis. This was obtained from the Q^2-integrated missing mass spectra.
The final dilution factor can be obtained selecting the $\pi^+ n$ channel with the missing mass spectrum cuts introduced in section and evaluating the ratio

$$f = \frac{3H}{NH_3} = \frac{NH_3 - c^{12}C}{NH_3} \tag{5.18}$$

as a function of W. The result, plotted in figure 5.11, shows again that the Q^2 dependence is negligible and that therefore it's possible to use in all the Q^2 bins the same dilution factor. The W dependence of the dilution factor is determined by two factor. First of all since the channel selection is performed using a fixed missing mass cut, the resolution can introduce a W dependence. In addition fro high invariant-mass values, multipion production becomes dominant. In this range the multipion production on nitrogen can 'leak' below the neutron missing mass peak due to the Fermi motion. This is shown in figure 5.12 in which the comparison between NH_3, ^{12}C and proton missing mass spectra

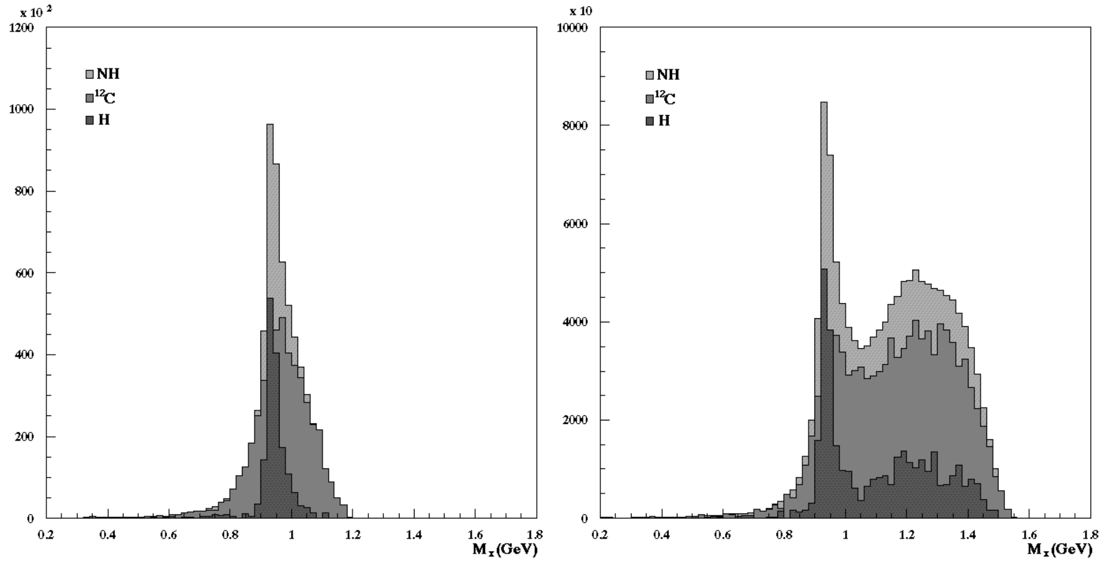

Figure 5.12: *Comparison between NH_3, ^{12}C, and proton missing mass spectra for two different W bins. The left and right plots correspond respectively to $1.24 < W < 1.36$ GeV and $1.6 < W < 1.72$ GeV.*

is plotted at two different W. This phenomenon does not introduce contamination in the extracted asymmetry but simply modifies the dilution factor.

5.8 Acceptance Correction

The advantage of studying spin asymmetries is that an asymmetry is in principle independent from the detector acceptance and efficiency. However in the present analysis, because of the limited statistics, the spin asymmetries have been studied in the form of integrated quantities in which the numerator and denominator are integrated over one the kinematical variables of the reaction. The azimuthal angle ϕ^* was chosen for the integration since the ϕ^* behavior of the cross-section is completely predicted based on kinematics. Using this approach it becomes necessary to apply an acceptance correction since this is not fully canceled in the ratio.
The evaluation of the acceptance correction can be separated into two steps, the first related to the geometrical acceptance and the second to the efficiency of the detector.
The geometrical acceptance issue can be easily solved in the present case because fiducial cut have been used in the analysis: these cuts define in fact a precise geometrical region whose area determines the acceptance. In the following the procedure used to evaluate this acceptance will be described in detail.
The efficiency of the detector is usually evaluated using Monte Carlo simulations in which the exact detector layout and geometry are considered. For the present analysis this can be avoided. The first reason is that the asymmetries are studied as a function of the electron variables Q^2 and W. In this way the asymmetries are completely independent from the electron-detection efficiency. Furthermore an asymmetry is sensitive only to the variation of the efficiency and not to its average value. Since the events are selected

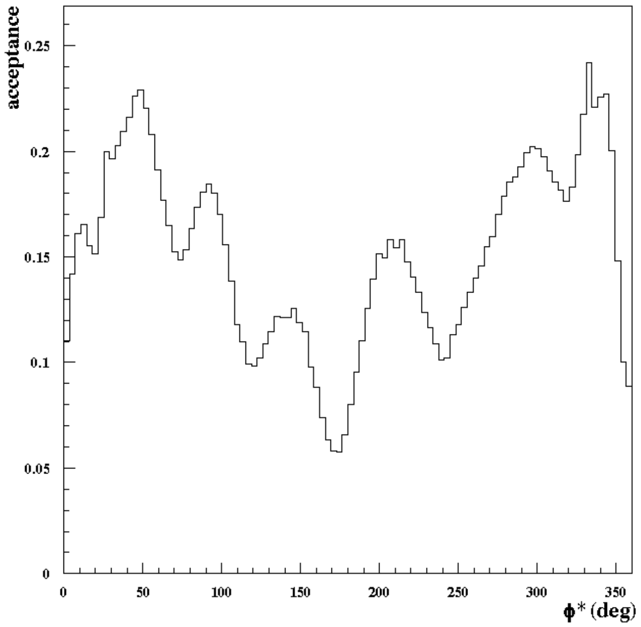

Figure 5.13: *Calculated acceptance for the π^+n channel as a function of ϕ^*. The calculation has been performed for $Q^2 = 0.55\ GeV^2/c^2$ and $W = 1.55 GeV$.*

inside fiducial region chosen expressly to avoid areas with strongly varying response, the final effects are expected to be very small.

However a study of efficiency related effects has been performed and will be discussed in section 6.3. As mentioned above the acceptance within the fiducial regions can be easily calculated. Single pion electroproduction (see section 1.2) can be described in the center of mass frame using four kinematical variables as Q^2, W, θ^*, and ϕ^*. In the lab frame those variables can be converted into the electron momentum and polar angle, p_e and θ_e, the pion polar angle θ_π and the difference between the pion and electron azimuthal angles, $\phi_\pi - \phi_e$, while the pion momentum p_π can be expressed as a function of the other variables.

The electron azimuthal angle is on the contrary a free variable as in all electron-scattering experiments and does not provide any dynamic information. This is true also in the polarized case if the target polarization component in the $\{\hat{x}, \hat{y}, \hat{z}\}$do not depend explicitly from the electron-azimuthal angle, as in the present configuration.

For a fixed kinematics, the geometrical acceptance is in fact given by the ratio over 2π of the angular range in which ϕ_e can be varied while the scattered electron and pion remain inside the fiducial regions. The number of events with fixed kinematics (Q^2,W,θ^*,ϕ^*) detected within the fiducial cuts can be written as

$$\begin{aligned} n(Q^2, W, \theta^*, \phi^*) &\sim \int \sigma(E_0, Q^2, W, \theta^*, \phi^*) a(p_e, \theta_e, \phi_e, p_\pi, \theta_\pi, \phi_\pi) d\phi_e = \\ &= \int \sigma(E_0, p_e, \theta_e, \theta_\pi, \phi_\pi - \phi_e) a(p_e, \theta_e, \phi_e, p_\pi, \theta_\pi, \phi_\pi) d\phi_e = \quad (5.19) \\ &= \int \sigma(E_0, p_e, \theta_e, \theta_\pi, \phi') a(p_e, \theta_e, \phi_e, p_\pi, \theta_\pi, \phi' + \phi_e) d\phi_e = \end{aligned}$$

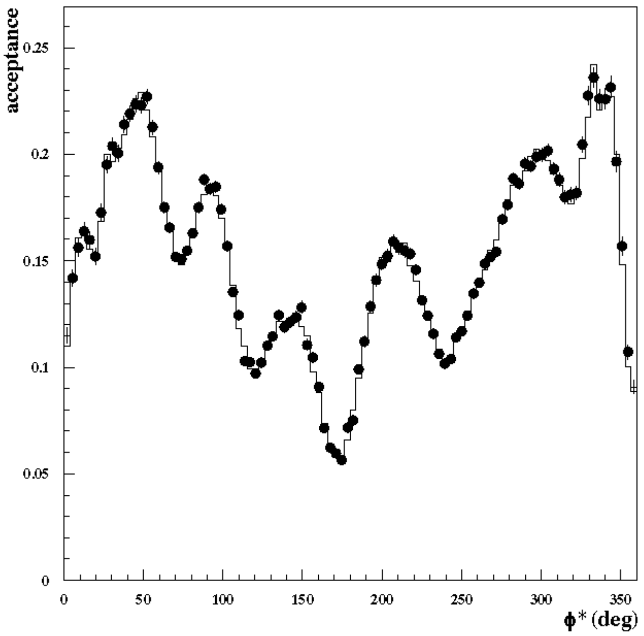

Figure 5.14: *Comparison between the results of the acceptance calculation (full line) and the estimate obtained using a Monte Carlo (red points).*

$$= \quad \sigma(E_0, Q^2, W, \theta^*, \phi^*) \int a(p_e, \theta_e, \phi_e, p_\pi, \theta_\pi, \phi' + \phi_e) d\phi_e$$

where $a(p_e, \theta_e, \phi_e, p_\pi, \theta_{pi}, \phi' + \phi_e)$ is a step function that is equal 1 of the event is inside the fiducial region and zero outside. This function can be expressed as the product of the single particle acceptance functions that describe the fiducial regions introduced in chapter 4. The integral is therefore simply the convolution between the two functions that represent the fiducial cut for the electron and pion. Figure 5.13 shows an example of the acceptance calculated with this approach for a particular Q^2, W, θ^* value and as a function of ϕ^*. The results of the calculation have been also verified by comparing with the result of a Monte Carlo as shown in figure 5.14. This plot also demonstrates the advantage given by the analytical calculation. The Monte Carlo in fact gives always a finite error and a longer computing time. In addition the acceptance can be strongly varying as shown by the plots in figure 5.13 and a good reproduction of this dependence can be achieved in the case of the Monte Carlo only simulating a very large amount of events with a fine binning.
Using the analytical calculation the acceptance correction is applied event by event avoiding therefore the model dependency introduce by a finite binning.

5.9 Radiative Correction

In electroproduction processes, radiative phenomena affect the cross-section measurement. The radiative effects apply to the incident and scattered electrons and to the vertices connecting the virtual photon to the electron and hadron currents. The first order diagrams of this process are in fact shown in figure 5.15. The direct consequence of these processes is a discrepancy between the particles momenta at the interaction vertex and the external momenta of the beam and final state particles. For example in the process shown in figure 5.15.a, a real photon is radiated from the incident electron before it exchanges a virtual photon with the proton, reducing the effective energy of the incident electron on the proton. On the contrary, in the process shown in figure 5.15.c, the radiation of a real photon occur after the exchange of a virtual photon with the target, which means that the energy of scattered electron at the primary vertex is higher than the one observed experimentally. In both cases the radiative effect results in the assignment of the wrong values of the kinematical variables used to describe the reaction (Q^2, W, θ^*, ϕ^*).

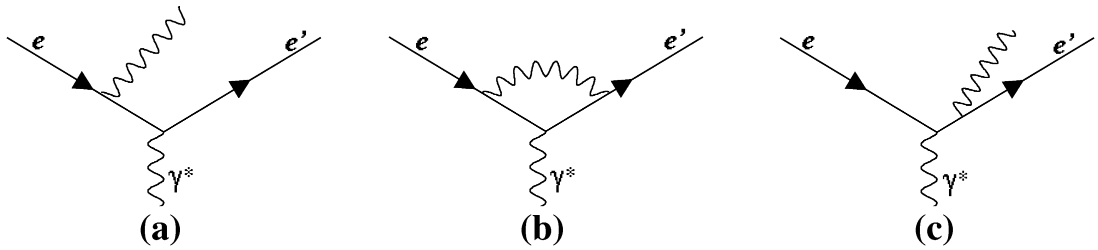

Figure 5.15: *First order diagrams that contribute to the radiative processes.*

In inclusive scattering, the primary consequence is that, since the elastic cross section rises very rapidly with decreasing beam energy, the probability for radiation of an high energy photon followed by elastic scattering can be very large. In exclusive reaction, like pion production, the elastic contribution is obviously excluded since the final state includes an additional particle. However the decay angular distributions are dependent on the invariant hadronic mass, which can have a different value at the interaction vertex than the one obtained from the initial and final electron kinematics due to the radiative effect. For the same reason, the missing mass distribution is distorted by the radiative phenomenon. The missing mass that is reconstructed from events in which the incident or scattered electron emit a real photon are displaced in respect to the correct value, forming a tail as shown in figure 5.16.

In addition to all the effects mentioned above, the magnitude of the cross section is changed by the radiative process in which a virtual photon is exchanged between the incident and scattered electron. This diagram is characterized the same final state of the unradiated process and, consequently, they cannot be separated. Their amplitudes are therefore summed coherently in the calculation of the cross section that is in fact affect by the interference of the two. To account for radiative effect, a correction for the $ep \to e'\pi^+n$ channel has been calculated using a generalization of the Mo and Tsai procedure to exclusive electroproduction [73].

Mo and Tsai [72] provide the equations for calculating the radiative cross sections for elastic and inclusive inelastic electron-proton scattering assuming the Born cross section is known. The Born cross section is substituted by model for pion electroproduction that in the present case is MAID, the Unitary Isobar Model developed in Mainz [74]. A fundamental point in this procedure is that model should be adjusted until the model plus radiative corrections matches the experimental cross section. As will be discussed

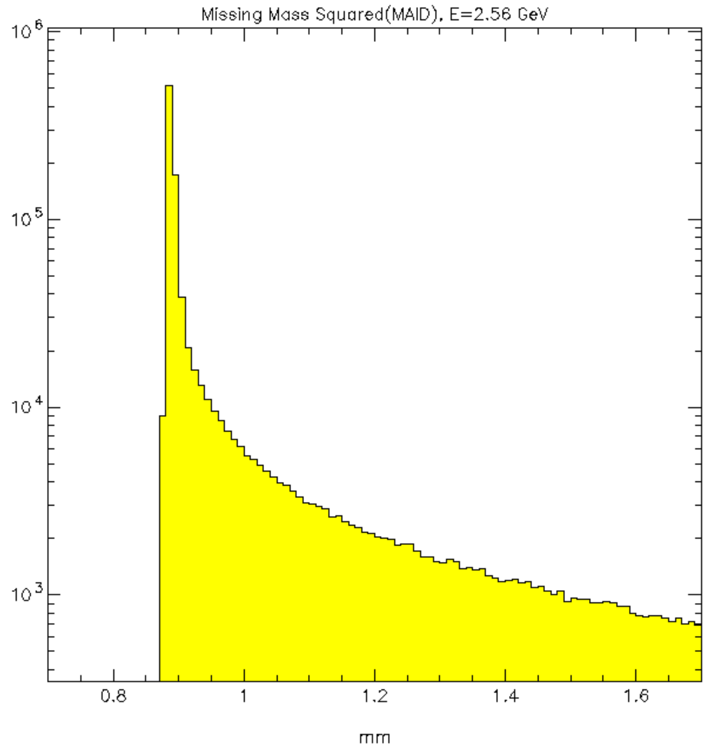

Figure 5.16: *Missing mass for the $p(e,e'\pi^+)n$ channel with the effects of radiative processes. The histogram represents the missing mass squared obtained with the Monte Carlo calculation.*

in section 6.4, MAID shows a very good agreement with the CLAS data and is therefore a good candidate for calculating the radiative correction. The radiated cross section is then evaluated using a Monte Carlo technique to calculate the integrals contained in the Mo and Tsai formulas. The radiative correction is calculated as the ratio between the radiated and unradiated cross section. To account for radiation in the target before and after the primary scattering event, the straggling calculations given in Mo and Tsai are included, randomly calculating the energy loss case by case for the electrons traveling through the target. In the calculation for the radiated cross section, it is necessary to choose a small energy, Δ, that defines the two photon energy ranges in which the Mo and Tsai integral is subdivided. For photon energy less than Δ, the radiative phenomenon is simply assumed to affect the born cross section by an overall factors that include the exchange of a virtual photon between the incident and scattered electron and the emission of soft photon. This factor is given by the Mo and Tsai correction factor. On the contrary, for photon energy greater than Δ, the Mo and Tsai integration formula is used. The parameter Δ is simply chosen to be less than the resolution of the CLAS detector (Δ= 5 MeV). The total cross section should be insensitive to the choice of the parameter Δ provided it is small and in fact a very little dependence (less than 1%) was found for choices of Δ between 3 and 10 MeV.

In the calculation of the radiated cross section, the direction of the electron is assumed to be unchanged by the radiation process. This is justified on the grounds that the radiative cross section is very strongly peaked for the photon to be emitted in the direction

of the electron that is responsible of the radiation. For the same reason and to make the integration more efficient the Monte Carlo search is concentrated in the region of these peaks. In addition, to improve the search in the phase space, the variables were changed to the set for which the cross section is more uniform.
As shown in figure 5.17, the radiative correction to the unpolarized cross section is typically of the order of 10-20% with a sign that depends on the W region. This dependence is determined by the combined effects of soft- and hard-photon emission. The emission of soft photon, i.e. with energy less than Δ, results in a lower cross section and the corresponding correction is therefore greater than 1. This occurs in the P_{33} region where, as shown in figure 5.17, the radiated cross section is approximately 20 % lower than the Born cross section. On the contrary at higher W the corrections becomes less than 1. This is a consequence of the emission of hard photons (photon energy higher than Δ) in events in which the true invariant mass corresponds to the mass of the P_{33} resonance. In fact, as for elastic scattering, at low energy the P_{33} resonance is the dominant contribution to the process and therefore the probability for the emission of a hard photon with the consequent excitation of this resonance is very high. The same phenomenon occurs also for the other resonances, the D_{13} and the F_{15}, whose contributions appear at higher W.
Using the same procedure it is straightforward to calculate the radiative correction for an asymmetry. In this case the effects described above have two direct consequences. First of all, since the observable is defined as the ratio of two cross sections, the magnitude of the radiative effect is reduced and part of the correction cancels out. the second effect is related to the radiation of hard photons. As mentioned above, for these events the misassignment of the particle momenta results in a wrong invariant mass that is higher than the true value. These events carry the asymmetry that would correspond to the correct invariant mass, producing in the end a distortion in the measured asymmetry. For this reason the radiation of hard photon is the dominant contribution to the radiative correction for the spin asymmetry. However it is very important to notice that most of the hard photon contribution can be rejected by applying a cut on the reconstructed missing mass distribution. The events in which the incident or scattered electrons emit a real photon with energy higher than Δ form in fact the radiative tail in the missing mass spectrum. This part is removed in the analysis procedure by selecting the reaction with the missing mass technique and therefore does not affect the final data sample. In this case the radiative correction is calculated applying the same missing mass cut on the simulated Monte Carlo events. As a results the W dependence of the radiative correction is strongly reduced as shown in figure 5.17 and the correction on the spin asymmetry is only of the order of few % . Of this order is in fact the final correction estimated for the double spin asymmetry.

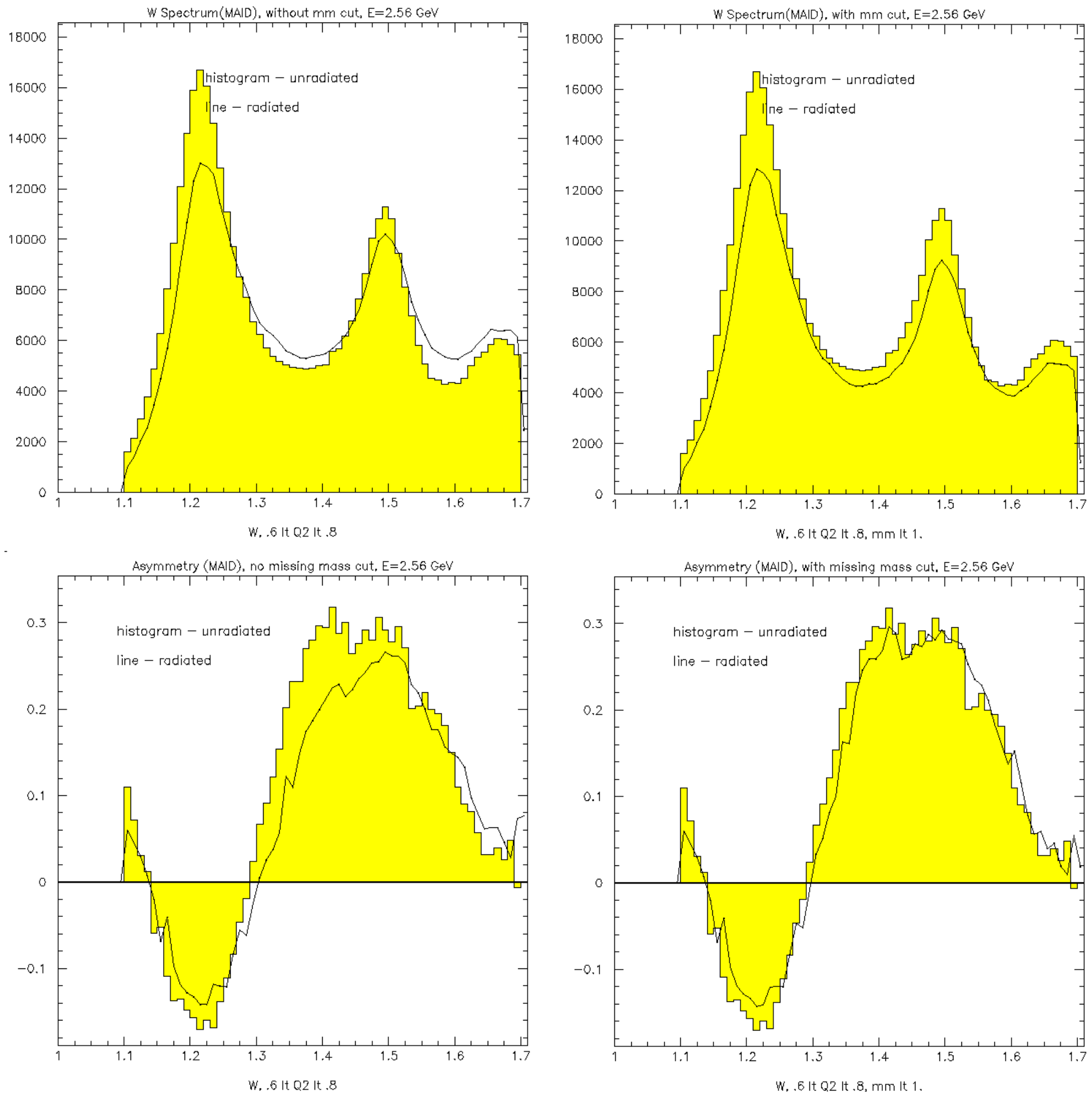

Figure 5.17: *Results of the radiative correction evaluation. The top plots show the estimated radiative effect on the W spectrum in the case no missing mass cut is applied (left) and in the case the missing mass is required to be less than 1 GeV (right). The bottom plots show the corresponding effects on the double spin asymmetry.*

Chapter 6

Results and Discussion

6.1 Introduction

The final purpose of this analysis is the extraction of the double spin asymmetry in the $ep \to e\pi^+ n$ channel. This is the first measurement ever performed for this observable and the results are presented in this chapter.
The physical meaning of the double spin asymmetry (see section 1.4.1) can be better understood considering its relation with the helicity asymmetry A_1 defined in the first chapter. Due to the EG1 kinematics, the main contribution to the double spin asymmetry are in fact the polarized response functions $R^l_{TT'}$ in the numerator, and the unpolarized transverse response function R^0_T in the denominator. In this experiment, the target polarization is in fact oriented along the direction of incident electron. Consequently, the longitudinal polarization P_l becomes the dominant component, while the transverse components P_n and P_t correspond only to a small fraction of the total polarization. The functions $R^l_{TT'}$ and R^0_T are determined respectively by $A^2_{3/2} - A^2_{1/2}$ and $A^2_{3/2} + A^2_{1/2}$, resulting therefore in a direct relation between the double spin asymmetry that is measured and the helicity asymmetry. The asymmetry was obtained using the procedure discussed in the previous chapter. This method relies on using data set with different combination of the target and beam polarization to separate the spin-dependent terms of the cross-section. This represents one of the main issues in this analysis and therefore a particular care was dedicated to test the results and to evaluate the systematic error affecting this procedure.
In this chapter I will describe the results obtained with this analysis. I will discuss in details the systematic studies that were performed for each different step of the asymmetry extraction and finally I will present the final results. The double spin asymmetry will be compared with a physics model and the behavior of this observable will be discussed.

6.2 Results

Following the procedure introduced in the previous chapter, I evaluated the double spin asymmetry for the 2.5 GeV data. The asymmetry was obtained based on the expression defined in eq. 5.6. This can be evaluated either as a function of all the four variables of the reaction or integrating over one or more of them.

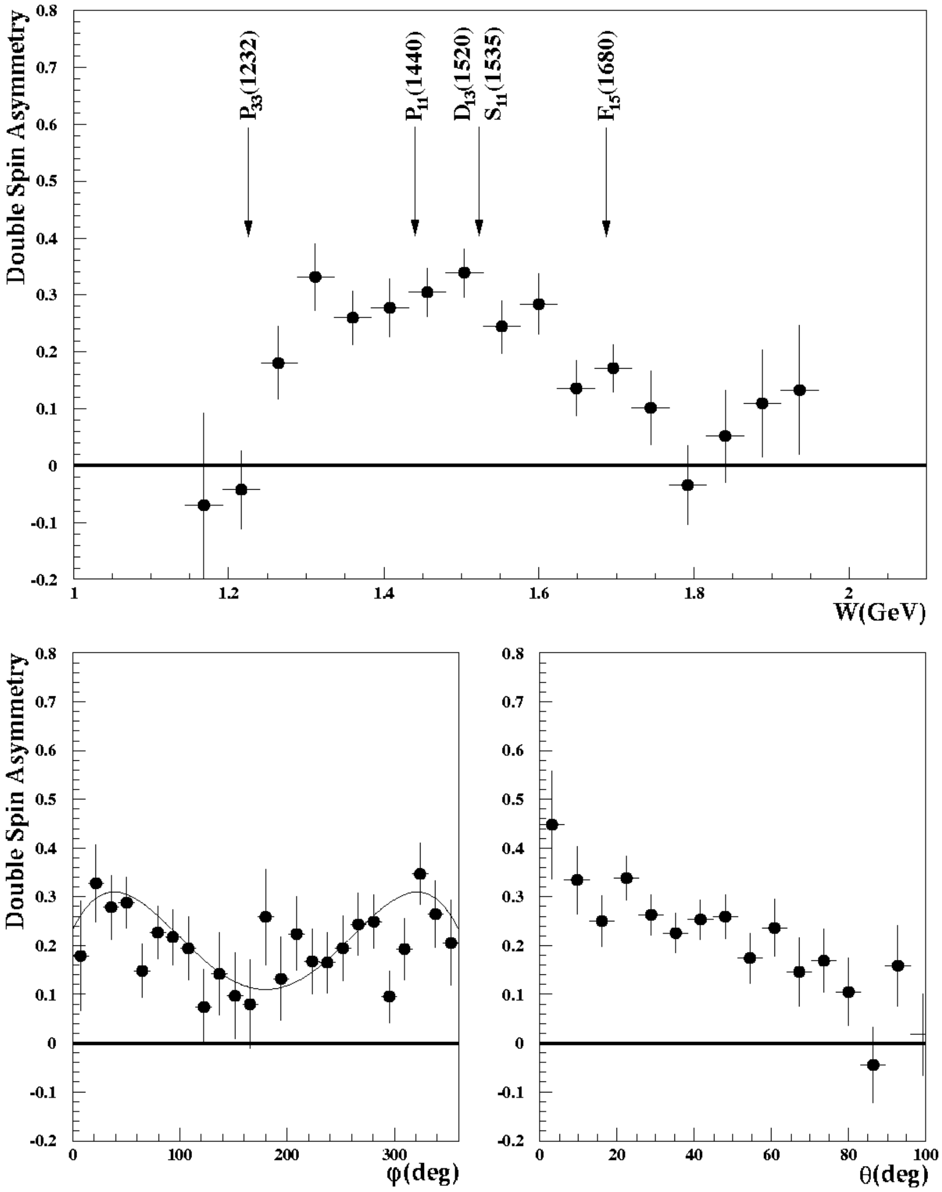

Figure 6.1: *Double spin asymmetry as a function of the hadronic invariant mass W, and the pion azimuthal angle ϕ^* and polar angle θ^*. In each plot the asymmetry is integrated over the other variables.*

As an example the three plots in figure 6.1 show the asymmetry as a function of W, θ^* and ϕ^* respectively, but integrated over the other variables. These results already indicate the general feature of these observables. The double spin asymmetry is in fact slightly negative in the Δ region while is positive in the second and third resonance region. In addition the angular dependence shows that the asymmetry tends to be larger in the forward direction. This is a consequence of the angular momentum conservation that limits the collinear production to the helicity-1/2 amplitude. These two features are a clear indication of the connection between the double spin asymmetry and the helicity asymmetry that is expected to have these characteristics. Finally the azimuthal dependence of the observables shown in the third plot is in agreement with the behavior predicted by equation 1.17. This is in fact expected to be a combination of different terms whose ϕ dependence is describe by even functions of the center mass angle ϕ^*.

Further information can of course be obtained studying the angular-dependence of the asymmetry as a function of the four-momentum transfer Q^2 and the invariant mass the W. However because of the limited statistics available for this reaction, the asymmetry has been evaluated as integral of the azimuthal angle ϕ^*. This limits obviously the possibility of extracting the single response functions but nevertheless allows the use of an interesting method to separate the different spin terms. In calculating the integrated asymmetries it is in fact necessary to take into account the angular dependence of the integrand function. As mentioned above, the double spin term σ_{et} is expected to have a ϕ^* dependence of the form

$$a + b\cos\phi^* + c\cos^2\phi^* + d\sin^2\phi^*.$$

On the contrary, the electron spin term of the cross section σ_e is predicted to have a $\sin\phi^*$ dependence from the center of mass azimuthal angle.
The first useful consequence is that while the integral over ϕ^* of the double spin asymmetry is expected to be different from zero, the integral of the electron spin term is predicted to vanish. This particular feature represents an important check of the consistency of the results. The second consequence is that the predicted angular dependences of the two mentioned spin terms are complementary and this can be exploited to improve and verify the separation of the two observables. In fact, following the same argumentation used above, if in the integral is introduced a $\sin\phi^*$ weight, then the integral of the double spin term will become zero, while the electron spin term will give a non-zero value. This expected features are verified by the CLAS data as shown in figure 6.2.
These particular properties result in an alternative method to separate the spin dependent terms. In fact comparing data set with opposite electron helicity (see section 5.4) it is possible to extract the quantity

$$\bar{N}_{\uparrow\uparrow} - \bar{N}_{\downarrow\uparrow} = P_e\sigma_e - P_e P_t \sigma_{et} \tag{6.1}$$

This can be integrated ove ϕ^* as explained above and two integrals will give

$$\begin{aligned} \int (\bar{N}_{\uparrow\uparrow} - \bar{N}_{\downarrow\uparrow}) d\phi^* &\to -P_e P_t \sigma_{et} \\ \int (\bar{N}_{\uparrow\uparrow} - \bar{N}_{\downarrow\uparrow}) sin\phi^* d\phi^* &\to P_e \sigma_e \end{aligned} \tag{6.2}$$

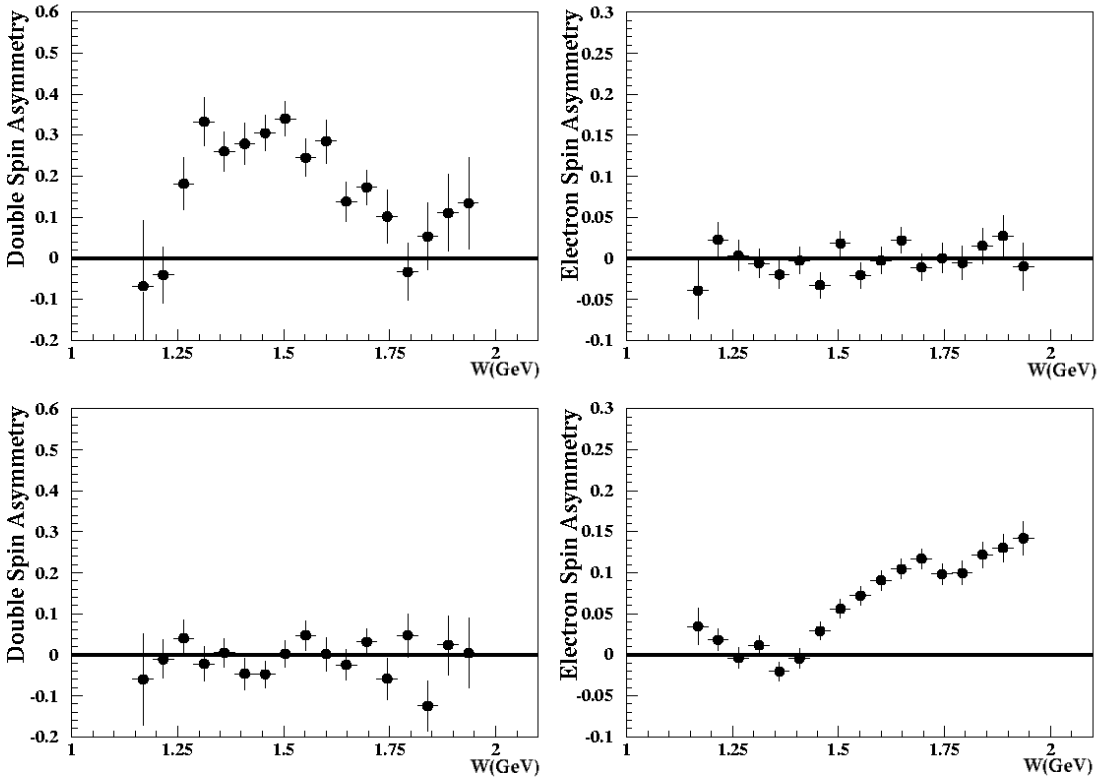

Figure 6.2: *Double spin asymmetry and electron spin asymmetry as a function of the hadronic invariant mass W. The asymmetry is integrated over the azimthal angle of the pion. As mentioned in the text, the double spin asymmetry is non-zero when integrated over ϕ^* (top left) but vanishes if the a $\sin\phi^*$ weight is added in the integral (bottom left). Viceversa the integral of the electron spin asymmetry is non-zero with the additional weight (top right) but vanishes without (bottom right).*

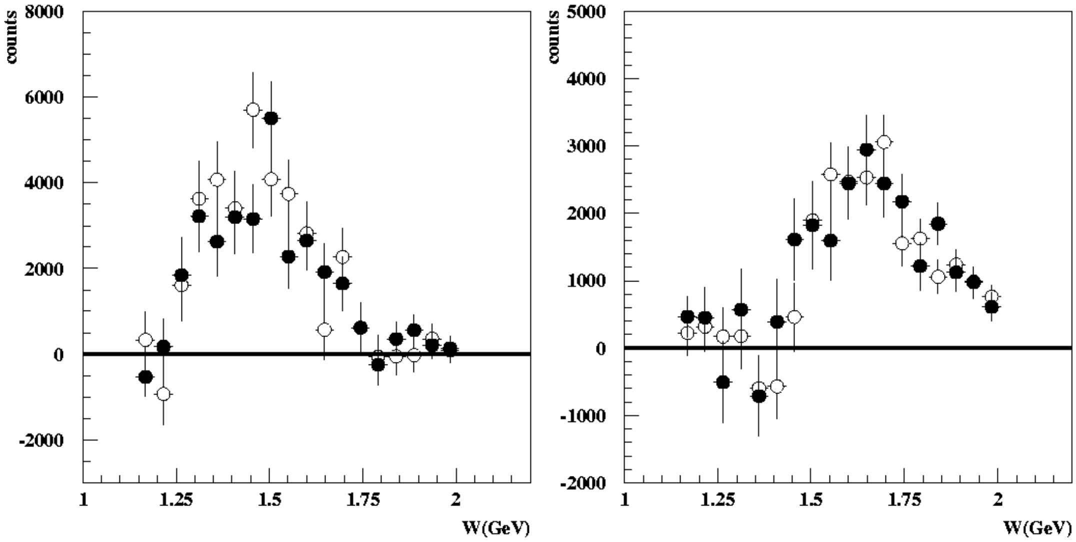

Figure 6.3: *Comparison of the double spin (left) and electron spin (right) yields extracted using the four possible combination of electron and proton helicities (full circles) and the ϕ^*-integral (open circles).*

The results obtained with this method have been compared with the asymmetry extracted by combining measurements with both opposite electron helicity and target helicity. Figure 6.3 shows in fact this comparison indicating that the two techniques give consistent results both for the double spin term (left plot) and the electron spin term (right plot).

6.2.1 Q^2 Dependence

The double spin asymmetry has been studied in details as a function of the four-momentum transfer Q^2. The results are shown in figure 6.4 . The three plots in this figure represent the double spin asymmetry in three different Q^2 bins and clearly indicate an increasing trend in the asymmetry for increasing Q^2. This behavior can be partly explained in term of the virtual photon polarization ϵ. The double spin term is in fact defined as (see section 1.4.1):

$$\begin{aligned}\sigma_{et} &= -\sqrt{2\epsilon_L(1-\epsilon)}[\sin\theta_\gamma(R^x_{LT'}\cos^2\phi^* + R^y_{LT'}\sin^2\phi^*) + R^z_{LT'}\cos\theta_\gamma\cos\phi^*] + \\ &- \sqrt{1-\epsilon^2}[R^x_{TT'}\sin\theta_\gamma\cos\phi^* + R^z_{TT'}\cos\theta_\gamma].\end{aligned}$$

where the term $\sqrt{1-\epsilon^2}$ is the degree of circular polarization of the virtual photon. This factor tends to increase with Q^2 resulting in larger experimental asymmetries.
However even after correcting for this factor, the double spin asymmetry still shows a increasing trend as indicated by the bottom plot in figure 6.4. This is consistent with the theoretical expectations. As mentioned before, the double spin asymmetry is in fact related to the helicity asymmetry A_1. This is predicted to increase with Q^2 both in the second and third resonance region. This rise is mainly due to the transition of the $D_{13}(1520)$ and $F_{15}(1680)$ from pure helicity 3/2 excitations at the photon point to helicity 1/2 for higher Q^2. In addition the $S_{11}(1535)$ resonance is expected to give a large contribution to the π^+ channel for higher Q^2. Since this resonance can contribute only to the helicity 1/2 amplitude, this results in a larger helicity asymmetry.

6.2.2 Angular Dependence

The angular dependence of the double spin asymmetry has been studied for θ^* between $0°$ and $75°$, i.e. the region with larger acceptance, and the results are shown in figure 6.5 for different bins in Q^2 and W.
As already observed, the asymmetry tends to rise in the forward direction. This is a direct consequence of the angular-momentum conservation. In fact in the collinear configuration, i.e. at $\theta^* = 0°$, only s-waves give a non-zero contribution. This implies that in this kinematics only the helicity-1/2 amplitude can contribute.
In the $P_{33}(1232)$ region, the asymmetry varies from positive values in the forward region to a slightly negative value for $\cos\theta^* < 0.75$. The process is in fact determined by the overlap of the resonant and non-resonant contribution that in the π^+ channel represent a significant part the cross-section. In this W region, i.e. close to the pion threshold, the non-resonant background is dominated by the emission of pion is s-waves and therefore gives a positive contribution to the double spin asymmetry.

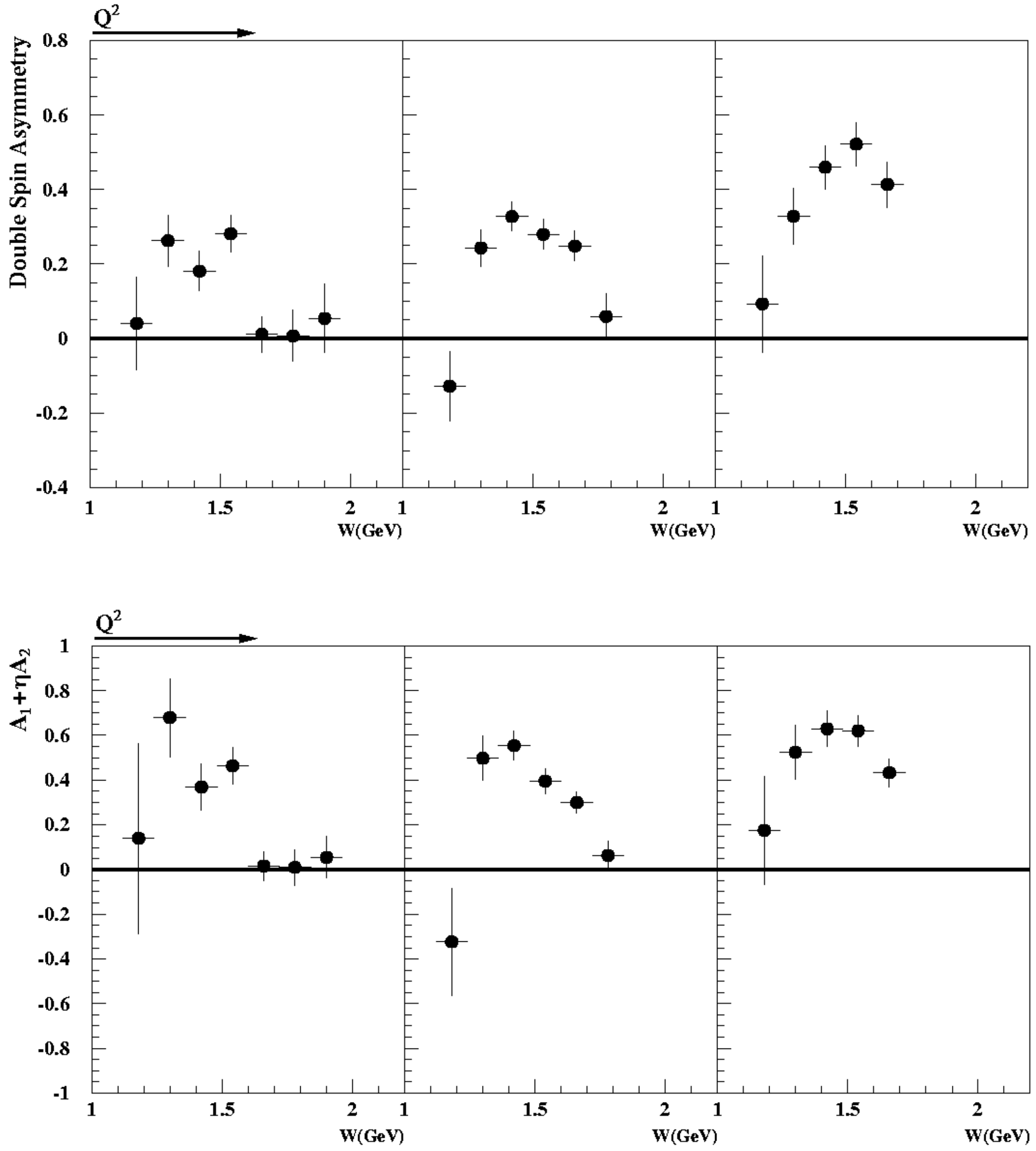

Figure 6.4: *Q^2 dependence of the double spin asymmetry. The top plots represent the asymmetry as defined in section 1.2 while the bottom plots represent the same after the correction for the virtual-photon depolarization. The plots shows the W dependence in three Q^2 intervals: 0.3 - 0.5, 0.5 - 0.9, 0.9 - 1.5 GeV$^2/c^2$.*

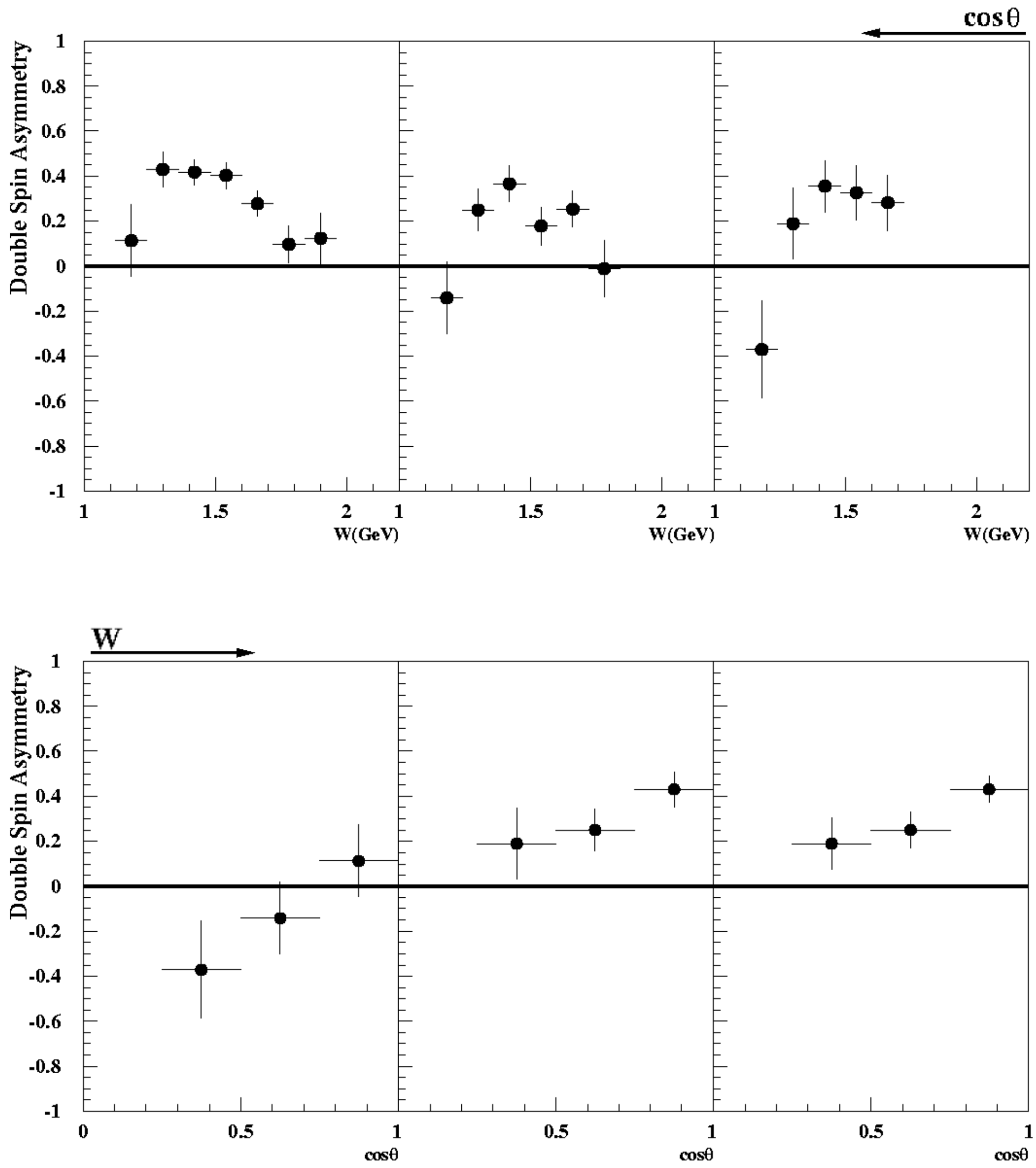

Figure 6.5: *Angular dependence of the double spin asymmetry. All the plots are for Q^2 is between 0.5 and 0.9 GeV^2/c^2. The top plots shows the asymmetry as a function of W for different $\cos\theta^*$ intervals (0.75-1.0, 0.5-0.75, 0.25-0.5 from left to right). The bottom plots shows the $\cos\theta^*$ dependence for different W intervals (1.12-1.24, 1.24-1.36, 1.36-1.48 GeV).*

The resonant term produces instead a positive asymmetry in the forward region where the helicity-1/2 amplitudes dominates and a negative asymmetry at larger angles due to the helicity-3/2 amplitude. This is in fact described by the first-order Legendre polynomial $1 - \cos\theta^*$. The resonant and non-resonant terms are therefore summed coherently in the forward region where they are both positive, while the have opposite signs at larger angles. This can explain the small asymmetry that is measured in this W interval.

6.3 Systematic Error Evaluation

This section is dedicated to the discussion of systematic effects that may affect this measurement. This is one of the most important issues for this analysis since the measured asymmetry are usually small and can be distorted by several effects.
Possible source of systematic error can derive from the cuts used to select the reaction and to the other parameters, as beam-charge asymmetry, polarization and dilution factor, which are required for the extraction the double spin asymmetry. Each of these sources have been studied separately and the following subsections will be dedicated to the discussion of each of them.
The results of this study are summarized in table 6.2.

6.3.1 Run Selection

As discussed in section 5.3, the 2.5 GeV data were selected according to precise quality checks. These are fundamental in an asymmetry measurement in which variations in the detector response or in any other parameter can produce false asymmetry.
The tests that were performed show that, for the 'good' runs, the number of events normalized to the accumulated charge is stable within $\pm 1.5\%$. In addition the comparison of the W distribution for various runs indicates the presence of localized differences of the order of 2% in the shape of the spectrum.
The evaluation of the impact of these variations is not straightforward. It's important to remind that the present analysis is in fact focused on the evaluation of the double spin asymmetry. This observable is obtained comparing spectra computed for different electron helicity and the electron helicity is flipped at a frequency of 1 Hz. Consequently this asymmetry is not expected to be sensitive to changes that occur on a long time scale (hours or days) as the one observed.
In conclusion to give a quantitative estimate of the systematic effect related to the run selection, I have compared the difference of fixed-helicity W spectra obtained from different sets of runs. An example is shown in figure 6.6. The two graphs show the double spin (left) and electron spin (right) terms extracted from the 2.5 GeV data. These are integrated in ϕ^* with no weight and with $\sin\phi^*$ weight respectively. The full and empty circles were obtained from two sets of runs with similar statistics but recorded with approximately one week of time in between.
The conclusion is that the two sets of runs are compatible within the statistical error and that no effect related to run to run differences is therefore detectable.

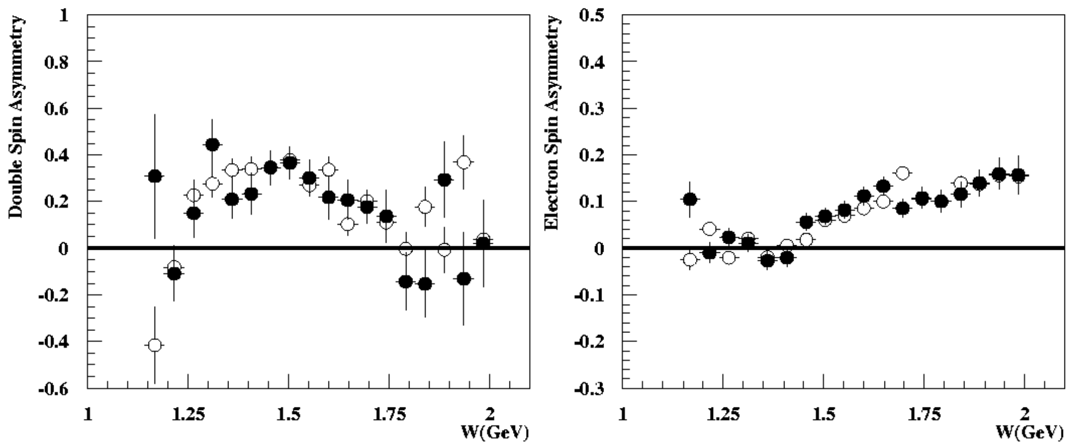

Figure 6.6: *Comparison of the double spin asymmetry and electron spin asymmetry extracted from two sets of data with similar statistics. The comparison shows that the two results are compatible within the statistical error.*

6.3.2 Channel Selection

Another possible source of systematic is the channel selection. Each of the cuts described in chapter 4 can in principle introduce a systematic bias.
I have studied in particular problems related to the electron identification and to the missing mass cuts.
As mentioned in section 4.6.1, the electron identification is a very important issue that need to be tested accurately. The main problem is the contamination from other charged particles. The approach I have adopted has been to tighten the cuts used in the analysis and to verify the correspondent effect. In particular we have made the electron identification more restrictive by requiring the detection of a Cerenkov signal corresponding to a number of photo-electrons higher than 2.5. This cut excludes the peak that is shown in figure 4.8 and that may be due to bad light collection or contamination.
The results have been compared with what obtained without the additional cut. Such comparison clearly indicate that the cut on the number of photoelectron does not introduce any significant effect and as a consequence that there is no evidence of pion contamination even in the very high W region where misidentified pion yield would appear.
A similar approach was used to study the missing mass cut effects. In this case I have simply tighten the cut from 0.85 GeV $< M_X <$1.05GeV to 0.90 GeV $< M_X <$ 0.98 GeV. Figure 6.7 shows the comparison of the tight cut result (open circle) with the large cuts (filled circles). In this case we have compared simply the final double spin and electron spin asymmetry. The change in missing mass cut induce in fact a modification of the dilution factor and for this reason the raw asymmetry are expected to be different while the final ones should be comparable.
In conclusion the tests that have been performed demonstrates that no significant effect is associated with the cuts used for the particle identification and for the selection of the exclusive reaction. The small shifts in the data points there were observed in this

procedure have been anyhow included in the evaluation of the systematic error.

6.3.3 Beam Charge Asymmetry

A detailed description of the study on the beam charge asymmetry was given in section 5.5. For the 2.5 GeV data the beam charge asymmetry was estimated to be

$$A_d = -(0.336 \pm 0.006)\%.$$

The uncertainty on this factor is transferred to the raw asymmetry since as explained before the charge asymmetry correction has the effect of a shift on the measured asymmetry. Considering the typical size of the raw asymmetry that was observed, $\sim 1-5\%$, this error gives a relative uncertainty of $\sim 0.15 - 0.75\%$.
This contribution is included in the final evaluation of the systematic error (see table 6.2).

6.3.4 Normalization Factors

In section 5.4 I explained how the procedure to extract the final asymmetries involves the introduction of normalization constants like the factor d and α_{et}. These constant have been evaluated from the data and in the present case the values that were obtained are

$$\begin{aligned} d &= (0.6339 \pm 0.0002) \rightarrow 0.03\% \\ \alpha_{et} &= (1.305 \pm 0.007) \rightarrow 0.05\% \end{aligned}$$

Both these contributions to the systematic error are therefore practically negligible.

6.3.5 Polarization

A detailed explanation of the evaluation of the product of the beam and target polarization was given in section 5.6.
The polarization was evaluated following two different methods to select elastic events and the results were found to be compatible within the statistical error. This was an important check to estimate the systematic uncertainty of the measurement. Since in fact the two methods agrees this has to be negligible in respect to the statistical error. This leads to a relative uncertainty of $2.5 - 3\%$.
The uncertainty on the polarization is directly transferred as a systematic error on the final asymmetry. This is in fact obtained by dividing the raw asymmetry for the beam and target polarization. Since the polarization values for the sets of runs with opposite target polarization have been normalized to the same value introducing the factor α_{et}, the analysis relies on a single polarization measurement. In this case the data set were normalized to the polarization observed for the negative target polarization, i.e. $(-39. \pm 1.)\%$. This corresponds to a relative systematic error of 2.5%.
This study is obviously related to the hydrogen polarization. However during the polarization process the nitrogen nucleus contained in the ammonia molecule gains a small degree of polarization that has to be taken into account when correcting the target polarization. The nitrogen polarization, even if it was not measured during the experiment,

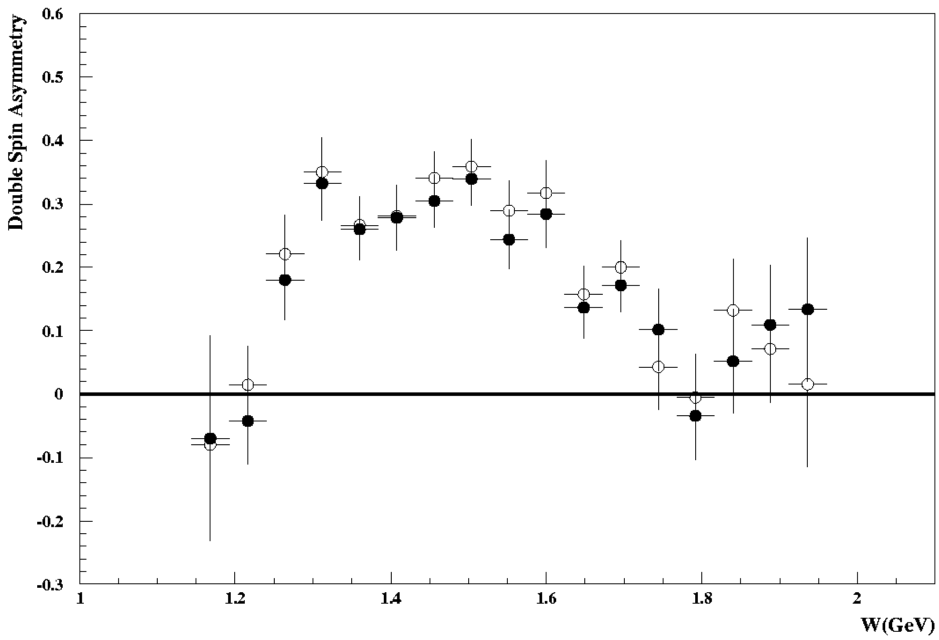

Figure 6.7: *Comparison of the double spin asymmetry obtained using different missing mass cuts. The full circles correspond to a missing mass cut between 0.85 and 1.05 GeV, while the open circles correspond to a cut between 0.9 and 0.98 GeV. The two results agree fairly well within the statistical error with a* $\chi^2 = 0.43$ *and with a centroid for the z-distribution of* (0.21 ± 0.14).

can be estimate since the ^{15}N and the H nuclei have been found to follows the Equal Spin Temperature (EST) prediction [63, 68]. This regime is established when two polarizable systems are connected by spin-spin interaction. In that case, their behavior can be described in term of a common 'spin temperature', T_S. In that case, it was demonstrated that the equilibrium between the two systems is reached when their polarization satisfy the relations

$$P(^{15}N) = \tanh \frac{\mu_{^{15}N} B}{K T_S}, \qquad P(H) = \tanh \frac{\mu_p B}{K T_S}. \tag{6.3}$$

This expression allows the estimate of the nitrogen polarization from a known proton polarization. In the present case, the typical proton polarization was measured to be approximately $\sim 60\%$. Since the ^{15}N magnetic moments is $\sim -0.28\mu_B$, this leads to a ^{15}N polarization of $\sim -6.0\%$. This value can then be used to estimate the polarization of the unpaired proton in the ^{15}N nucleus. This is in fact a odd-even nucleus in which the nuclear magnetic moment is completely hold by the seventh proton. This is in p-shell and its spin couples to the orbital angular momentum to give a total angular momentum equal to 1/2. Using the Clebsh-Gordon coefficients it is possible to express the proton polarization in terms of the nitrogen polarization, that in fact is given by

$$P(p) = -\frac{1}{3} P(^{15}N) \tag{6.4}$$

The polarization of the unpaired proton is therefore expected to be of the order of $\sim 2.0\%$ and parallel to the spin direction of the hydrogen nuclei.

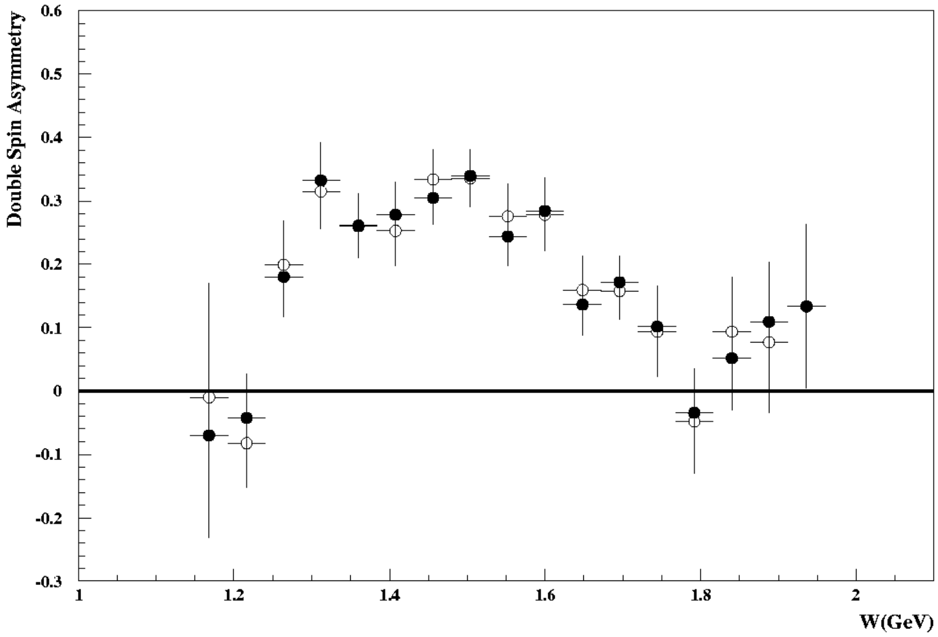

Figure 6.8: *Comparison of the double spin asymmetry obtained using all the six sectors of the detector (full circles) and excluding sector 5 (open circles). The two results agree fairly well within the statistical error with a* $\chi^2 = 0.14$ *and with a centroid for the z-distribution of* (0.03 ± 0.09).

The contribution of this additional nucleon can be included when calculating the numerator of the asymmetry where this will be added to the free nucleons as

$$3P(H) \rightarrow= (3P(H) + P(p)).$$

The final effect is an increase of the effective proton polarization of $2.0\%/3 \sim 0.6\%$. In addition the missing mass selection we used in the analysis cuts out part of the nitrogen contribution that is spread because of the Fermi motion. Therefore we can estimate an addition reduction of a factor 3 that brings the final correction to be $\sim 0.2\%$. The correction is applied modifying the polarization factor from 39.% to 39.2%.

6.3.6 Acceptance Correction

In section 5.8 I have explained the technique used to evaluate the acceptance correction for our reaction and I have discussed in detail the reason why the efficiency of the detector is not expected to affect the asymmetry results. Nevertheless is important to give a quantitative demonstration of this fact. In this section I will describe the approach used for this purpose.
The basic idea was to modify the fiducial cuts that define the regions of the detector in which events are accepted and to study the correspondent effect. This has been done in different ways to have a more complete test.
The first test was to recalculate the asymmetry after excluding an entire sector. The sector that was rejected is sector 5. This approach is useful for the study on the acceptance issue since the loss of a sector does not change the kinematical coverage but changes the

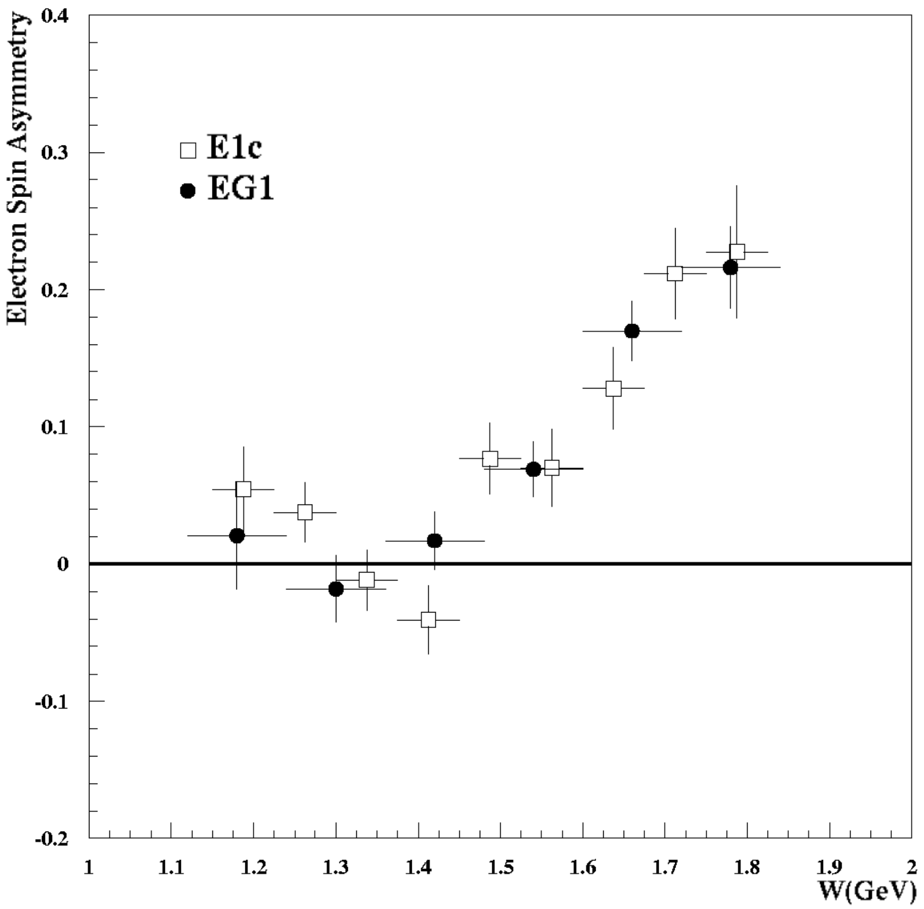

Figure 6.9: *Comparison of the electron spin asymmetry obtained from the EG1 (full circles) and E1C (open squares) data for Q^2 between 0.9 and 1.5 GeV^2/c^2, and $\cos\theta^*$ between 0.75 and 1. The two experiments differ for the target that in EG1 is the polarized NH_3 target and in E1C is a liquid-hydrogen target.*

efficiency. In particular sector 5 was chosen since in the quality checks it showed the lowest electron rate. The results that were obtained are shown in figure 6.8 in comparison with the results obtained with the six sectors. The two graphs show the comparison for the double and electron spin asymmetries in the two cases and demonstrates that the two sets of results are perfectly compatible within the statistical error.
As second test, I have changed the electron fiducial cuts applying a tighter version. Again this modification changes the detector region accepted in the analysis and as a consequence the efficiency for the reaction. The results show that, also in this case, no efficiency effects are detectable.

As final check I have compared our result for the electron spin asymmetry with the result obtained from CLAS data recorded with polarized beam on an unpolarized liquid-hydrogen target, in the E1C run. For this purpose I have analyzed a selected sample of $\sim$ 25 M electrons from that data set with beam energy 2.567 GeV and torus current $+2250A$. Since this run period used a pure liquid hydrogen target, it represents

Test	χ^2	z-distribution
Run Selection	1.18	(-0.16 ± 0.28)
Electron Cuts	0.56	(-0.18 ± 0.15)
Missing Mass Cut	0.43	(0.21 ± 0.14)
Acceptance: 5/6 sectors	0.14	(0.03 ± 0.09)
Acceptance: loose/tight cuts	0.38	(-0.11 ± 0.13)
Acceptance: EG1/E1C data	0.75	(0.12 ± 0.86)
Pion decay	0.01	(0.07 ± 0.01)

Table 6.1: *Summary of the results obtained in the systematic studies. The table includes the χ^2 values and the z-distribution parameters for the each of the test performed.*

the ideal condition for electron spin measurement. For this reason the comparison is very important to confirm the reliability of our results in respect to several fundamental issues. First of all, in this data there is no need for a separation of the electron and double spin asymmetry because the target is unpolarized. In addition the comparison is a direct way to study efficiency problems. In E1C the running condition are in fact very different from EG1, both for the detector setup and for the reconstruction procedure. In the E1C run the absence of the polarized target implies that no solenoidal field affects the particle trajectories, and in particular that the azimuthal angle is unchanged. In addition as mentioned in chapter 3, the EG1 target was moved upstream to the center of the CLAS detector of ~60 cm. These main modifications introduce an intrinsic difference between the efficiency and the acceptance in the two runs. Due to the different setup, the same event would in fact produce hits in different position of the detector. As a consequence the comparison of events with the same kinematical configuration in the two runs becomes a comparison between the response of different parts of the detector. In spite of all these modifications, the comparison plotted in figure 6.9 for a particular Q^2 and $\cos\theta^*$ bin where the kinematical coverage in the two runs is similar shows an extremely good agreement.
This demonstrates, first of all, that the detector efficiency does not affect the final results and that the procedure used to separate the spin asymmetries is successful. In addition it indicates that no evident nuclear effect that may be distinguishable by comparison of the two targets occur.

6.3.7 Pion Decay

The dominant decay mode for charged pion is the weak decay $\pi^\pm \to \mu^\pm \nu_\mu$. The branching ratio for this decay mode is $(99.98770 \pm 0.00004)\%$ and the life time has been measured to be $(2.6030 \pm 0.0024) \cdot 10^{-8}$ s [1].
Charged pions produced by the photon-nucleon interaction can therefore decay before being detected. The typical pion momentum varies from a lower limit of 200 MeV up to 2 GeV. As a consequence the shortest lifetime in the laboratory frame is approximately 80 ns corresponding to a path before the decay of approximately 3.5 m. Since the typical path length of a charged particle before producing a hit in the time of flight is $\sim$ 4-5 m,

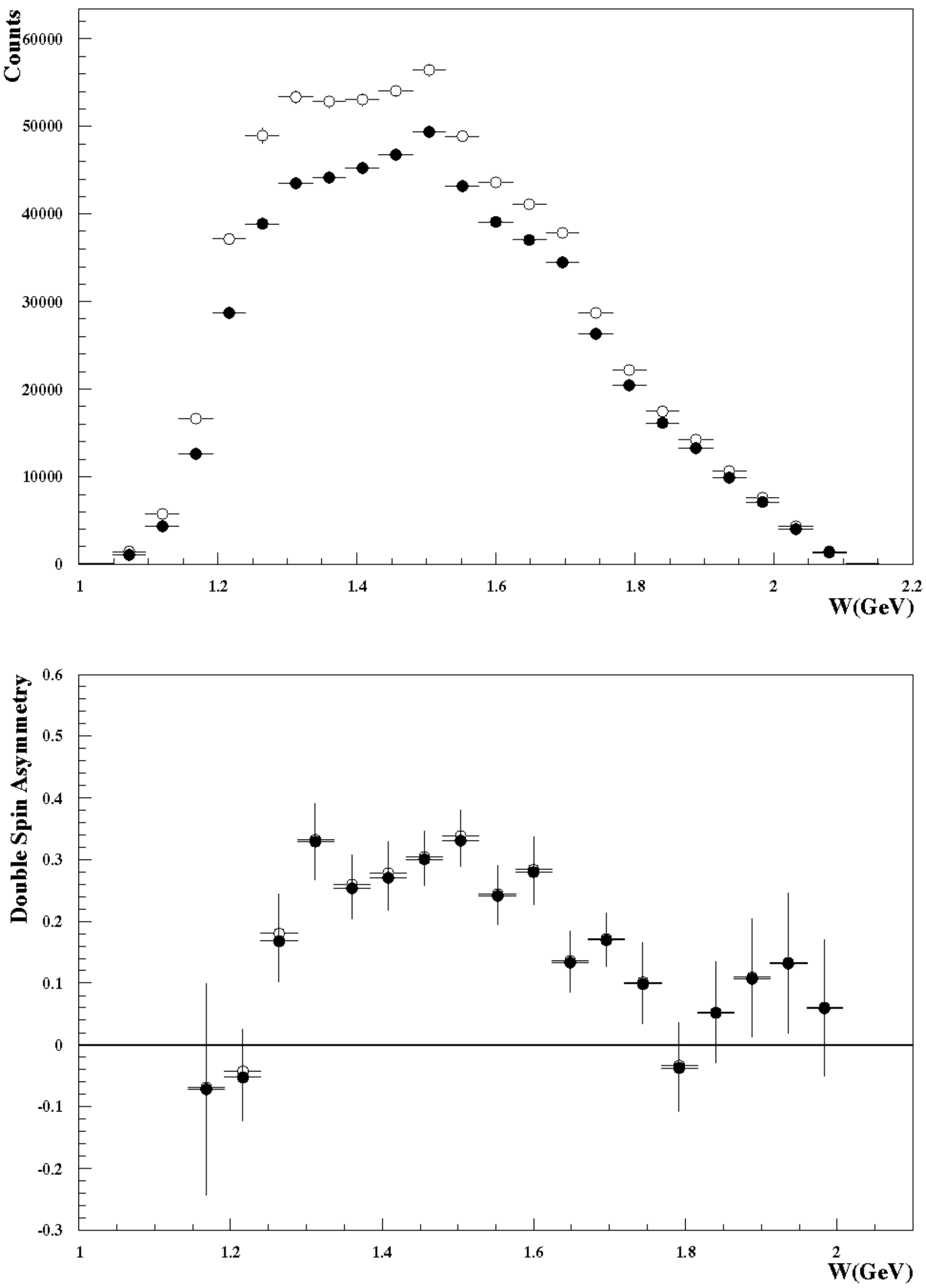

Figure 6.10: *Results of the study on the effect of pion decay. A correction to account for the pion decay has been calculated assuming that the mesons that decay before exiting from the detector are not reconstructed. The effect of the correction is clearly visible on the W spectrum shown in the top plot where the open circles represent the spectrum after the correction in comparison with the raw spectrum (full circles). The effect on the asymmetry is however almost negligible as shown in the bottom plot. The two results agree fairly well and the small shift that can be observed in the data points has been included in the evaluation of the systematic error.*

pion can decay before exiting from the CLAS detector. When this occurs close to the track vertex, the reconstruction process is likely to fail and the particle is lost. However since one of the decay product, i.e. the muon, is a charged particle whose mass is close to the pion mass, the muon track can be reconstructed and be identified as a pion. In this case the particle is not lost but its momentum can be misassigned. This events can be anyhow partially rejected by applying narrow cuts on the missing mass and vertex distributions, as was done in this analysis. In this case the main effect is therefore a loss of events that need to be corrected.
Since the present analysis aims at the extraction of an asymmetry, this loss does not have in principle influence on the results. However since the probability of missing a charged pion depends on the kinematics and the measured asymmetries are integrated over the azimuthal angle ϕ^*, the pion decay may have a relatively small impact on the results in relation to the variation of the decay probability in the range of integration of the asymmetry.
To establish an upper limit on the impact of pion decay, the double spin asymmetry was evaluated in the assumption that all the pion that decay before reaching the time of flight are undetected. This probability was evaluated as

$$P_{loss} = 1 - \frac{1}{\tau_{lab}} \int_0^{t_{TOF}} e^{-t/\tau_{lab}} dt \tag{6.5}$$

where τ_{lab} is the pion life time in the lab frame and $t_{TOF} = t_{TOF}(p_\pi, \theta_\pi)$ is the time of flight for that particular kinematics. The data have then been corrected according to this loss probability event by event and the double spin asymmetry has been evaluated. This is shown in figure 6.10 in comparison with the uncorrected asymmetry. The comparison indicates that the two analyses agree perfectly within the statistical error bars and that the overall difference introduced by this correction is less than 1.5%.

The previous sections were dedicated to the discussion of the different sources of systematic error in the asymmetry measurement. In addition to the effects that were mentioned, another source of systematic uncertainty is represented by the dilution factor. The error in the evaluation of this quantity affect directly the final asymmetry since this is obtained by dividing the so-called 'raw asymmetry' measured on the NH_3 target by the dilution factor. This contribution to the systematic error is in reality dominant in respect to the others that were discussed previously. The uncertainty on the dilution factor varies between 3 and 8% for different W values. This is represented by the error bars on the dilution factor evaluation shown in figure 5.11. The error bars are due to the statistical uncertainty on the carbon spectrum used for the evaluation of the nitrogen contribution. However since the effect is transferred to any calculated asymmetry, it can be considered a source of systematic. Therefore this contribution has been combined with the other sources as shown in table 6.2.

Source	**Error**
Run selection	$< 3\%$
PID and channel Selection	$< 4\%$
Beam Charge Asymmetry	$0.15 - 0.75\%$
Normalization Factors: d	0.06%
Polarization	2.5%
Acceptance Correction and Efficiency	2%
Pion decay	1.5%
Dilution factor	$3 - 8\%$
TOTAL	$6 - 10\%$

Table 6.2: *Summary of the systematic errors on the asymmetry measurement*

6.4 Final Results and Physical Interpretation

The results discussed in section 6.2 are the first available measurements for the double spin asymmetry in the $ep \to e\pi^+ n$ channel in the resonance region. Therefore no comparison with previous measurements is possible. However the comparison with phenomenological and theoretical models able to predict the behavior of spin observables is feasible and at this stage desirable to obtain a physical interpretation of the results.
As noticed in chapter 1, the double spin asymmetry is very sensitive to the resonance structure and to the mechanism that is responsible for the transition from the nucleon to the excited state. For this reason the asymmetry represents a unique mean for the study of the baryonic resonances. However for the same reason very accurate and complete models are necessary to obtain the correct physical interpretation of the results.
Over the past 30 years a series of models on pion photo and electroproduction have been developed for hadronic invariant mass from the pion threshold up the first resonance region. However only few models cover the large W range of the CLAS data and have the characteristics necessary for a direct comparison with the results presented in this thesis.
Here a comparison between the CLAS results and the prediction of the MAID2000 model is proposed [74].
MAID2000 is the improved version of the Unitary Isobar Model developed in Mainz on pion photo and electroproduction. This model covers the W range from the pion threshold up to approximately 2 GeV and includes all the main resonances: $P_{33}(1232)$, $P_{11}(1440)$, $D_{13}(1520)$, $S_{11}(1535)$, $F_{15}(1680)$, and $D_{33}(1700)$.
The non-resonant contribution in the model are described using the standard Born terms with a mixed pseudovector-pseudoscalar πNN coupling and vector meson (ρ and ω) exchange. The mixed πNN coupling is chosen since it guarantees a good reproduction of the data both a low photon energy where the pseudovector coupling fulfills PCAC and is consistent with the low energy theorems and chiral perturbation theory, and at high energies where the renormalizable pseudoscalar coupling leads to a better description of the existing data. The Q^2 dependence for the Born terms is introduced explicitly with the nucleon and pion form factors that are expressed in the standard dipole form. Both the Born and vector meson exchange terms have been fitted to the existing data, in particular the coupling constants for the vector meson exchange were fixed to reproduce the behavior of the electromagnetic multipoles $M_{1+}^{(1/2)}$ and $E_{1+}^{(1/2)}$.
The resonance contributions in s-channel are parameterized by the standard Breit-Wigner form for the relevant multipoles. The unitarity condition was maintained by multiplying the resonant terms with the appropriate phase. The Q^2 dependence of the electromagnetic multipoles $M_{1+}^{(3/2)}$, $E_{1+}^{(3/2)}$ and $S_{1+}^{(3/2)}$ that contribute to the excitation of the $P_{33}(1232)$ is expressed in the model in the form

$$\frac{|\mathbf{k}|}{k_W} e^{-\gamma Q^2} F_D(Q^2)$$

where F_D is the usual dipole form factor and γ was determined from the existing data. On the contrary the multipole $M_{1-}^{(1/2)}$ that is related to the excitation of the Roper resonance $P_1 1(1440)$ is parameterized as

$$\frac{|\mathbf{k}|}{k_W} e^{-\frac{Q^2}{6\alpha^2}}$$

where α is the harmonic oscillator parameter of the quark model calculation. However as a consequence of the unitarization procedure, the Roper contribution is additionally suppressed with increasing Q^2, in agreement with the behavior shown in the existing data. The Q^2 dependence of the higher mass resonances was instead derived from the quark model calculation attributing the D_{13}, S_{11}, and D_{33} to the $[70, 1^-]$ multiplet and the F_{15} to the $[50, 2^+]$ multiplet. The model parameters were fitted, with good agreement, to the world data including all the unpolarized photo and electroproduction data and the few measurement of polarization observables at present available.
The comparison of the CLAS results with this isobar model has been performed calculating the model predictions for the double spin asymmetry in the exact kinematics of the experimental data. The model parameterization for the electromagnetic multipoles with angular momentum up to L=5 was used as basis for the calculation. The multipoles were calculated in steps of 0.05 GeV^2/c^2 in Q^2 and of 10 MeV in W. Linear interpolation between the points of this grid was used to obtain the multipoles value in the full phase space. These were used to calculate the 18 response functions (see section 1.2). The calculation was divided in three steps: first the CGLN amplitudes were evaluated using the electromagnetic multipoles; these amplitudes were then used to derive the helicity amplitudes from which finally the response functions were obtained. A summary of the formulas used in this calculation is given in appendix A. With this approach it is possible to evaluate the electroproduction cross section, including the polarized terms defined in section 1.2 in any allowed kinematics.
The spin-independent and spin-dependent parts of the cross section were integrated in the same kinematical bins used for the data analysis. The integral was performed numerically with steps of 0.05 GeV^2/c^2 in Q^2, 5 MeV in W, 0.025 in $\cos\theta^*$, and 2° in ϕ^*. To account for the non-complete coverage of the detector, the integral was limited to the region of the phase space accessible with the present experiment. This final correction was performed to have the most accurate reproduction of the experimental conditions, even if in the kinematical region were the comparison is proposed the angular coverage is of the order of 90%.
The comparison between the double spin asymmetry extracted from the CLAS data and the MAID predictions is shown in figure 6.11. The plots shows the W dependence of the double spin asymmetry for three different Q^2 and $\cos\theta^*$ intervals in comparison with the result of the calculation represented by the solid line. The comparison clearly indicates a good qualitative agreement in the behavior of the double spin asymmetry both for the W and Q^2 dependence. The MAID predictions obviously shows the expected negative or just slightly positive asymmetry in the P_{33} region as already noticed commenting the data, with good quantitative agreement with the CLAS data. In the second resonance region the asymmetry become strongly positive but a systematic shift between the data points and the model predictions is present. A larger discrepancy is evident at higher W where the data points shows a still positive asymmetry while the predictions indicates negative values. However this discrepancy is non completely surprising since in this invariant mass region it is reasonable to expect a significant contribution of high mass excited states that are not included in the model. In the W region from 1.7 GeV to 2.0 GeV significant contribution are in fact expected from several resonances as the $P_{13}(1720)$, $F_{35}(1905)$, $P_{31}(1910)$, and $F_{37}(1950)$. The main features of the angular dependence of the double spin asymmetry are also reproduced by the MAID predictions. In the P_{33} region the model confirmed what already observed in the data in relation

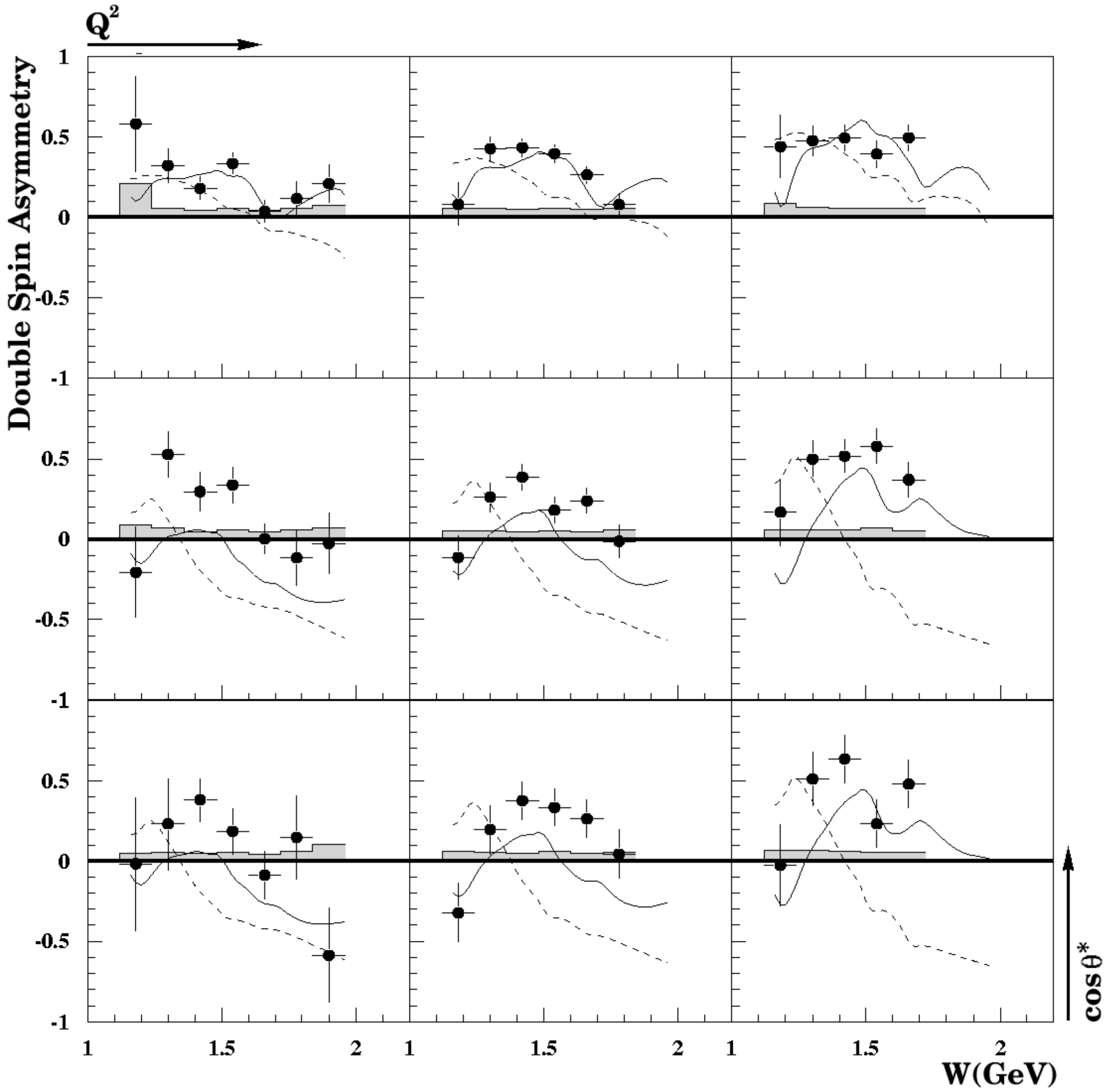

Figure 6.11: *Double spin asymmetry as a function of the invariant mass W for different Q^2 and $\cos\theta^*$ intervals. Each column corresponds to a different Q^2 bin: 0.3 - 0.5 GeV^2/c^2, 0.5 - 0.9 GeV^2/c^2, 0.9 - 1.5 GeV^2/c^2. The rows represent different $\cos\theta^*$ bins: 0.25-0.5, 0.5-0.75, 0.75-1. The error bars are statistical only, while the shadowed region represents the size of the systematic error. The solid line is the prediction of the MAID model for the double spin asymmetry including all dominant resonances and the background. The dashed line is the MAID prediction for the background only.*

to the positive value of the asymmetry in the very forward region. In this kinematics in fact both the resonance and background contribution are predicted to be positive. The separated contribution of the Born and vector meson exchange terms shown by the dashed line gives in fact a large and positive asymmetry in this W region.

In conclusion, the comparison clearly shows many similarities between the data and the MAID predictions, in particular at low W where a rather good knowledge of the resonant and non-resonant contribution is already available, while larger discrepancies appear at higher W. This is anyhow a success since the model is mainly based on unpolarized data, and the prediction of the spin asymmetry is therefore obtained indirectly from the existing measurements. A more precise understanding of the mechanisms that create these discrepancies may be obtained with thorough studies on the details of the resonant and non-resonant contributions to the double spin asymmetry. However the comparison that was proposed has already proven that the CLAS results provide a fairly good basis to perform such studies.

Conclusions

An experiment to measure spin observables in single-pion electroproduction has been performed in Hall B at Jefferson Lab using the detector CLAS (CEBAF Large Acceptance Spectrometer). The electron beam, polarized via the GaAs cathode technique, was scattered over a solid NH_3 target polarized by Dynamic Nuclear Polarization. The polarized target was designed and built for this application by a collaboration including Jefferson Lab, the University of Virginia and the INFN.
A first run of the experiment was completed in the fall of 1998 and the analysis of the data recorded at beam energy of 2.5 GeV has been presented in this thesis. These data cover the W range of the baryonic resonances at moderate and low Q^2 (0.3 GeV^2/c^2 $< Q^2 <$1.5 GeV^2/c^2) and allows for the first time the extraction of the double spin asymmetries in the $ep \to e\pi^+ n$ channel. The complete determination of this asymmetry requires in fact the measurement of the full angular distribution of the outgoing pion, which is achievable in this experiment thanks to the large acceptance of the CLAS detector.
The reaction was selected by detecting the electron and the pion in the final states and using the missing mass technique to isolate the neutron. The double spin asymmetry has been extracted as a function of the four-momentum transfer Q^2, of the hadronic invariant mass W, and of the polar angle θ^* of the outgoing pion in the center of mass frame. The ϕ^* dependence of the asymmetry, which is completely predicted by kinematics, was exploited to separate the double spin contribution from the single spin terms of the full electroproduction cross section. This procedure allows the extraction of the physics asymmetry and, in addition, has been proven to be a very powerful method to test the consistency of the results. The dilution factor correction to the asymmetry that accounts for the contribution of the ^{15}N nucleus of the ammonia molecule was estimated using carbon data while the beam and target polarization were evaluated based on the asymmetry observed in elastic scattering. A detailed study of systematic effect was performed, demonstrating the total systematic uncertainty in this measurement is rather small.
This experiment has provided the first measurement of the double spin asymmetry for the $ep \to e\pi^+ n$ channel in the resonance region. The physical interpretation of the results of this analysis has been proposed in terms of the helicity amplitude $A_{1/2}$ and $A_{3/2}$ that characterized the $\gamma_v N$ vertex. In the kinematics of this experiment, the double spin asymmetry is in fact strictly related with the helicity asymmetry $A_1 = (A_{1/2} - A_{3/2})/(A_{1/2} + A_{3/2})$.

The measured asymmetries indicates a strong dependence both from the invariant mass W and the momentum transfer Q^2, as expected from the resonance contribution. The asymmetry appears in fact to be negative or only slightly positive in the $P_{33}(1232)$ region, while it becomes positive in the second and third resonance region. The first feature is related to the overlap of the resonance excitation, expected to give $A_1 = -1/2$, with the Born mechanism that, close to the pion threshold, is predicted to give a positive asymmetry. At higher W, the observed asymmetry is compatible with the predicted helicity structure of the $D_{13}(1520)$ and $F_{15}(1680)$ that should in fact give a positive contribution in this Q^2 range. The double spin asymmetry shows in fact an increasing trend in Q^2 with maximum observed values of approximately 50% for the $Q^2 \sim 1.2$ GeV^2/c^2. This characteristic, enhanced by the kinematical dependence of the virtual photon polarization, confirms the predicted Q^2-dependence of the helicity amplitudes. The observed behavior is in fact consistent with an increase in the contribution of the helicity 1/2 amplitude expected both for the D_{13} and the F_{15} states, and with the rise of $S_{11}(1535)$ contribution that, for high Q^2, dominates the second resonance region. These observations have been confirmed by the comparison with the prediction of the Mainz Unitary Isobar Model, MAID that has allowed the calculation of the double spin asymmetry on the basis of the parameterization of the world electroproduction and photoproduction data.

These results demonstrate that the extracted double spin asymmetry in the $\pi^+ n$ channel can be measured with good accuracy using the CLAS data. A thorough study of details of the resonance and non-resonance contributions would be necessary to have a complete understanding of the measured asymmetry. Nevertheless the comparison of the CLAS results with a physics model has shown an overall agreement, demonstrating already that new physics information can be obtained from these observables. This measurement and the high-energy data, provided by the new experimental run, will therefore give an important contribution to improve the present knowledge on the baryonic-resonance structure.

Appendix A

Response functions, Helicity amplitudes and Multipoles

The response functions in electroproduction can be expressed in terms of the helicity amplitudes H_{1-6} via the following relation:

$$\begin{aligned}
R_T^0 &= \frac{1}{2}\left(|H_1|^2 + |H_2|^2 + |H_3|^2 + |H_4|^2\right), \\
R_T^y &= -\mathcal{I}m\left\{H_1^* H_2 + H_3^* H_4\right\}, \\
R_L^0 &= |H_5|^2 + |H_6|^2, \\
R_L^y &= -2\mathcal{I}m\left\{H_5^* H_6\right\}, \\
R_{LT}^0 &= \frac{1}{\sqrt{2}} Re\left\{H_5^* H_1 - H_5^* H_4 + H_6^* H_2 + H_6^* H_3\right\}, \\
R_{LT}^x &= \frac{1}{\sqrt{2}} \mathcal{I}m\left\{-H_5^* H_2 + H_5^* H_3 - H_6^* H_1 - H_6^* H_4\right\}, \\
R_{LT}^y &= \frac{1}{\sqrt{2}} \mathcal{I}m\left\{-H_5^* H_2 - H_5^* H_3 + H_6^* H_1 - H_6^* H_4\right\}, \\
R_{LT}^z &= \frac{1}{\sqrt{2}} \mathcal{I}m\left\{-H_5^* H_1 - H_5^* H_4 + H_6^* H_2 - H_6^* H_3\right\}, \\
R_{TT}^0 &= Re\left\{-H_1^* H_4 + H_2^* H_3\right\}, \\
R_{TT}^x &= \mathcal{I}m\left\{H_1^* H_3 - H_2^* H_4\right\}, \\
R_{TT}^y &= \mathcal{I}m\left\{H_1^* H_3 + H_2^* H_4\right\}, \\
R_{TT}^z &= -\mathcal{I}m\left\{H_1^* H_4 + H_2^* H_3\right\}, \\
R_{LT'}^0 &= \frac{1}{\sqrt{2}} \mathcal{I}m\left\{-H_5^* H_1 + H_5^* H_4 - H_6^* H_2 - H_6^* H_3\right\}, \\
R_{LT'}^x &= \frac{1}{\sqrt{2}} Re\left\{H_5^* H_2 - H_5^* H_3 + H_6^* H_1 + H_6^* H_4\right\}, \\
R_{LT'}^y &= \frac{1}{\sqrt{2}} Re\left\{-H_5^* H_2 - H_5^* H_3 + H_6^* H_1 - H_6^* H_4\right\}, \\
R_{LT'}^z &= \frac{1}{\sqrt{2}} Re\left\{H_5^* H_1 + H_5^* H_4 - H_6^* H_2 + H_6^* H_3\right\}, \\
R_{TT'}^x &= Re\left\{H_1^* H_2 + H_3^* H_4\right\}, \\
R_{TT'}^z &= \frac{1}{2}\left(|H_1|^2 - |H_2|^2 + |H_3|^2 - |H_4|^2\right).
\end{aligned}$$

The helicity amplitudes can be expressed in terms of the CGLN amplitudes as reported below:

$$\begin{aligned}
H_1 &= -\frac{1}{\sqrt{2}} \sin\theta^* \left(F_3 + F_4 \cos\theta^*\right), \\
H_2 &= -\frac{1}{\sqrt{2}} \left(2F_1 - 2F_2 \cos\theta^* + F_4 \sin^2\theta^*\right),
\end{aligned}$$

$$
\begin{aligned}
H_3 &= -\frac{1}{\sqrt{2}} F_4 \sin^2\theta^*, \\
H_4 &= \frac{1}{\sqrt{2}} \sin\theta^* \left(2F_2 + F_3 + F_4 \cos\theta^*\right), \\
H_5 &= F_5 + F_6 \cos\theta^*, \\
H_6 &= F_6 \sin\theta^*.
\end{aligned}
$$

The CGLN can be written as a multipole series in terms of derivatives of the Legendre polynomials P_l:

$$
\begin{aligned}
F_1 &= \sum_{l\geq 0} \left\{ (M_{l+} + E_{l+})\, P'_{l+1} + \left[(l+1)M_{l+} + l M_{l-} P'_{l-1}\right] \right\}, \\
F_2 &= \sum_{l\geq 1} \left[(l+1)M_{l+} + l M_{l-} P'_l\right], \\
F_3 &= \sum_{l\geq 1} \left[(E_{l+} - M_{l+})\, P''_{l+1} + (E_{l-} + M_{l-} P''_{l-1}\right], \\
F_4 &= \sum_{l\geq 2} \left(M_{l+} - E_{l+} - M_{l-} + E_{l-} P''_l\right), \\
F_5 &= \sum_{l\geq 0} \left[(l+1)L_{l+} P'_{l+1} - l L_{l-} P'_{l-1}\right], \\
F_6 &= \sum_{l\geq 1} \left[l L_{l-} - (l+1) L_{l+}\right] P'_l.
\end{aligned}
$$

Appendix B

$e\pi^+$ Missing Mass W and Q^2 distribution

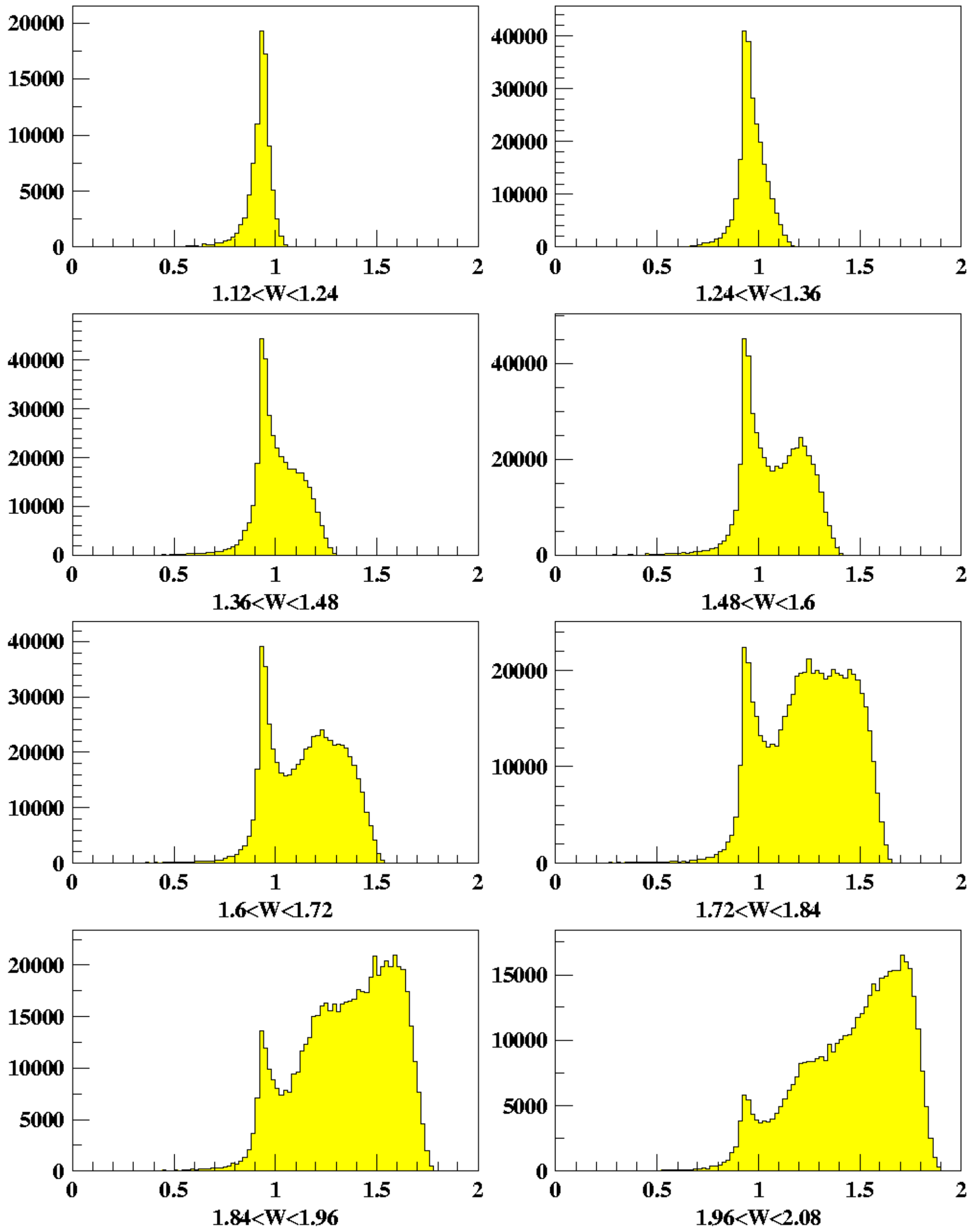

Figure B.1: $e\pi^+$ *Missing Mass for* $0.3 < Q^2 < 0.5$.

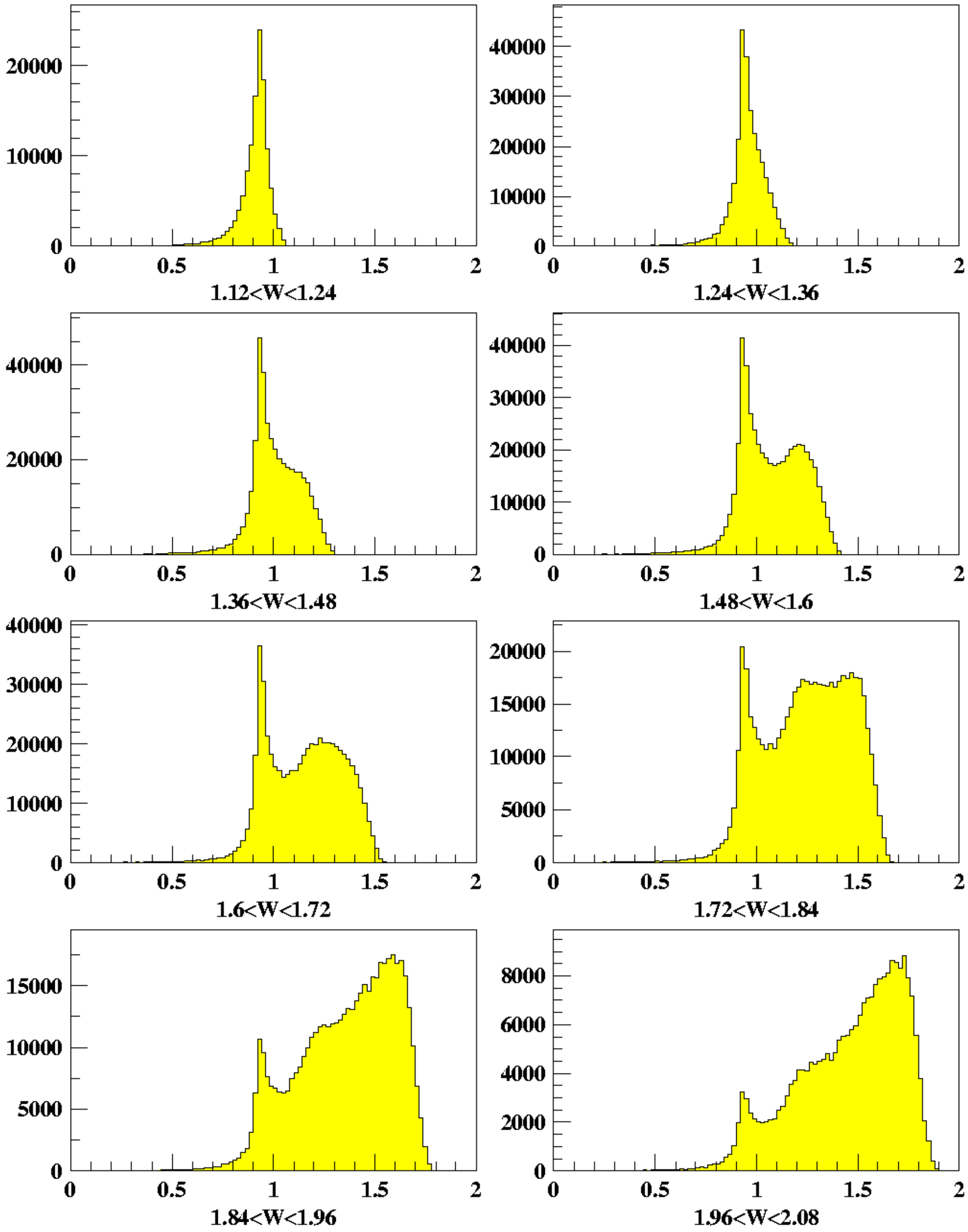

Figure B.2: *$e\pi^+$ Missing Mass for 0.5 $< Q^2 <$ 0.9.*

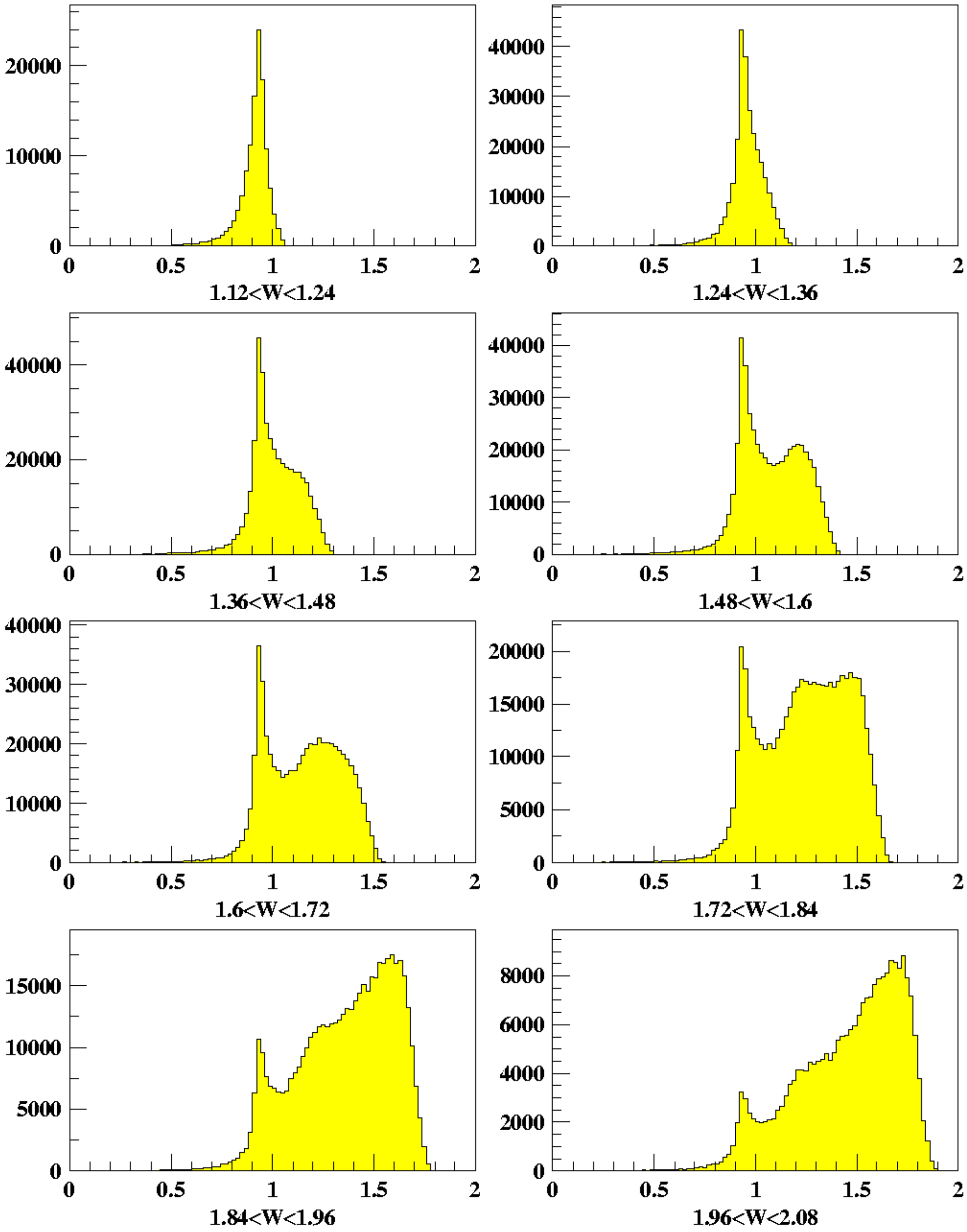

Figure B.3: *$e\pi^+$ Missing Mass for 0.9 $< Q^2 <$ 1.5.*

Bibliography

[1] Particle Data Group, *Review of Particle Properties*, *Phys. Rev.*, **54**, (1996).

[2] M.J.Alguard *et al.*, *Phys. Rev. Lett.*, **37**, 1261 (1976) and *Phys. Rev. Lett.*, **41**, 70 (1978).

[3] G.Baum *et al.*, *Phys. Rev. Lett.*, **51**, 1135 (1983).

[4] L.Tiator *et al.*, *Z.Phys.*, **A352**, 327 (1995).

[5] R.L.Walker, *Phys. Rev.*, **182**, 1729 (1969).

[6] A.S.Raskin and T.W.Donnelly, *Annals of Phys.* **191**, 78 (1989).

[7] V.Dimitrasinovic *et al. Research Program at CEBAF(III)*, (1988).

[8] A.Bartl and W.Majerotto, *Nucl.Phys.B*, **62**, 267 (1973).

[9] F.Foster and G.Hughes, *Rep. Prog. Phys.*, **46**, 1445 (1983).

[10] J.Ahrens *et al.*, *Phys. Rev. Lett.*, **84**, 5950 (2000).

[11] GRAAL Collaboration, *Phys. Rev. Lett.*, **81**, 1797 (1998).

[12] G.Blanpied *et al.*, Submitted to Phys. Rev. C.

[13] S.M.Dolfini *et al.*, *Phy. Rev.*, **C60**, 4622 (1999)

[14] C.Becchi and G.Morpurgo, *Phys. Lett.*, **17**, 352 (1969).

[15] R.Beck *et al. Phys. Rev. Lett.*, **78**, 606 (1997).

[16] K. Batzner et al., *Nucl. Phys.*, **B75**, 1 (1974).

[17] W.Albrecth *et al.*, *Nucl. Phys.*, **B27**, 615 (1971).

[18] S.Galster *et al.*, *Phys. Rev.*, **D5**, 519 (1972).

[19] C.Mistretta *et al.*, *Phys. Rev.*, **184**, 1487 (1968).

[20] J.C.Adler *et al.*, *Nucl. Phys.*,**B46**, 573 (1972).

[21] C.Gerhardt *et al.*, *DESY Rep. F21-079/02*, unpublished.

[22] R.Siddle *et al.*, *Nucl. Phys.*, **B35**, 93 (1971).

[23] R.D.Helllings *et al.*, *Nucl. Phys.*, **B32**, 179 (1971).

[24] E.Evangelides *et al.*, *Nucl. Phys.*, **B71**, 381 (1974).

[25] V.V.Frolov *et al.*, *Phys. Rev. Lett.*, **82**, 45 (1999).

[26] Particle Data Group, *Review of Particle Properties*, *Phys. Lett.*, **111B**, (1982).

[27] L.A.Copley *et al.*, *Nucl. Phys.*, **B13**, 303 (1969).

[28] J.Drees *et al.*, *Z. Phys.*, **C7**, 183 (1981).

[29] S.Capstick, *Proceedings of the NSTAR2000 Workshop, Jefferson Lab, February 16-19, 2000.*

[30] Z.Li *et al.*, *Phys. Rev*, **D46**, 70 (1992).

[31] C.Gerhardt, *Z. Phys.*, **C34**, 311 (1980).

[32] S.D.Ecklund and R.L.Walker, *Phys. Rev*, **159**, 1195 (1967).

[33] S.Capstick, *Phys. Rev.*, bf D46, 2864 (1992).

[34] S.Ono, *Nucl. Phys.*, **B107**, 522(1976).

[35] L.A.Copley *et al.*, *Phys. lett.*, **29B**, 117 (1969).

[36] F.E.Close *et al.*, *Phys. Lett.*, **38B**, 541 (1972), and *Phys. rev.*, **D6**, 2533 (1972).

[37] Particle Data Group, J.J.Hernandez *et al.*, *Phys. Lett.*, **B239**, 1 (1990).

[38] H.Breuker *et al.*, *Z. Phys.*, **C13**, 11391982); **c17**, 121 (1983).

[39] W.Brasse *et al.*, *Nucl. Phys.*, **B110**, 410 (1976).

[40] R.Haidan, *DESY Rep. F21-079/03*, unpublished.

[41] *CEBAF proposal*, PR-91-023.

[42] *CEBAF proposal*, PR-93-009.

[43] *CEBAF proposal*, PR-93-036.

[44] *CEBAF proposal*, PR-94-003.

[45] *CEBAF proposal*, PR-91-015.

[46] *CEBAF proposal*, PR-89-042.

[47] K.Abe *et al.*, *Phys. Rev. Lett.*, **74**, 346 (1995); *Phys. Rev. Lett.*, **75**, 25 (1995); *Phys. Lett.*, **B364**, 61 (1995); *Phys. Rev. Lett.*, **76**, 587 (1996); *Phys. Rev. Lett.*, **79**, 26 (1997); *Phys. Lett.*, **B**), 377 (1997) and *Phys. Lett.*, **B405**, 180 (1997).

[48] B.Adeva *et al. Phys. Lett.*, **B302**, 533 (1993) and D. Adams et a;., *Phys. Lett.*, **B396**, 338 1997.

[49] A.Airapetian, *et al.*, submitted to Phys. Lett.B.

[50] S.Gerasimov, *Soviet J. Nucl. Phys.*, **2**, 930 (1966).

[51] S.D.Drell and A.C.Hearn, *Phys. Rev. Lett.*, **16**, 908 (1966).

[52] J.Ellis and R.L.Jaffe, *Phys. Rev*, **D9**, 1444 (1974).

[53] *CEBAF Conceptual Design Report for Experimental Equipment*, (1990).

[54] M.D.Mestayer *et al.*, *Nucl.Instr. and Meth.***A449**, 81 (2000).

[55] D.S.Carman *et al.*, *Nucl.Instr. and Meth.***A419**, 315 (1998).

[56] G.Adams *et al.*, Submitted to Nuclear Instruments and Methods:7/28/200.

[57] M.Amarian *et al.*, Submitted to Nuclear Instruments and Methods:9/27/200.

[58] M.Anghinolfi *et al.*, *Nucl.Instr. and Meth.***A447**, 424 (1998).

[59] E.S.Smith *et al.*, *Nucl.Instr. and Meth.***A432**, 265 (1999).

[60] M.Borghini, *Proton Spin Orientation*, CERN Yellow report 1968,CERN-**68-32**.

[61] A.Abragam, *The principle of nuclear amgnetism*, Oxford Clarendon Pres (1961).

[62] W.Meyer, *Proc. Conf. On High Enegy Spin Physics-Brookhaven 1982, (ed. G.M.Bunce)*, AIP Conf. Proc. **95**, 506 (1983).

[63] D.G.Crabb *et al.*, *Nucl.Instr. and Meth.***356**, 9 (1995).

[64] A.A.Belayev at al., *Proc. Conf. On High Enegy Spin Physics-Minneapolis 1988, (ed. G.M.Bunce)*, AIP Conf. Proc. **187**, 1336 (1989).

[65] A.Thomas *et al.*, *Nucl. Instr. and Meth.*, **A356**, 5(1995).

[66] M.L.Seely *et al.*, *Proc. Conf. On High Enegy Spin Physics-Brookhaven 1982, (ed. G.M.Bunce)*, AIP Conf. Proc. **95**, 526 (1983).

[67] S.T.Goertz *et al.*, *Nucl. Instr. and Meth.*, **A356**, 20(1995).

[68] M.Goldman, *Spin temperature and nuclear magnetic resonance in solids*, Oxford Clarendon Press (1970).

[69] G.R.Court *et al.*, *Nucl. Instr. and Meth*, **A324**, 433 (1993).

[70] V.Blobel *et al.*, *The BOS system for the CLAS detector: Dynamic Memory Management*, (1995).

[71] M.Jones *et al.*, *Phys. Rev. Lett.*, **84**, 1393(2000).

[72] L.W.Mo and Y.S.Tsai, *Rev. Mod. Phys.*, **41**, 205(1969).

[73] R.Minehart, *private communication.*

[74] D. Drechsel *et al.*, *Nucl. Phys*, **A645**, 145 (1999).